Three-Dimensional Hybrid Simulation Of Dayside Magnetic Reconnection

by

Binying Tan

A dissertation submitted to the Graduate Faculty of
Auburn University
in partial fulfillment of the
requirements for the Degree of
Doctor of Philosophy

Auburn, Alabama
May 9, 2011

Keywords: magnetic reconnection, magnetospheric physics, hybrid simulation

Approved by

Yu Lin, Chair, Professor of Physics
Satoshi Hinata , Professor of Physics
Stephen Knowlton, Professor of Physics
J. D. Perez, Professor of Physics

Abstract

With a 3-D global hybrid simulation model, we investigate magnetopause reconnection and the energy spectra of cusp precipitating ions under different IMF conditions.

First, the magnetic configuration and evolution of Flux Transfer Events (FTE) and the associated ion density and ion velocity distribution at various locations on the magnetopause are investigated under a purely southward IMF. The results reveal: (1) Multiple X lines are formed during the magnetopause reconnection, which lead to both FTEs and quasi-steady type reconnection under a steady solar wind condition. The resulting bipolar signature of local normal magnetic field of FTEs is consistent with satellite observations. (2) A plasma temperature rise is seen at the center of an FTE, compared to that of the upstream plasma in the magnetosheath. The temperature enhancement is mainly in the direction parallel to the magnetic field due to the mixing of ion beams. (3) Flux ropes that lead to FTEs form between X lines of finite lengths and evolve relatively independently. The ion density is enhanced within FTE flux ropes due to the trapped particles, leading to a filamentary global density. (4) Different from the previous understanding based on the asymmetric density across the magnetopause, a quadrupole magnetic field signature associated with the Hall effects is found to be present around FTEs. (5) A combination of patchy reconnection and multiple X-line reconnection leads to the formation of reconnected field lines from the magnetosphere to IMF, as well as the closed field lines from the magnetosphere to the magnetosphere in the magnetopause boundary layer.

Secondly, both the spatial and temporal energy spectra of cusp precipitating ions are computed by tracing trajectories of the transmitted magnetosheath ions under a southward IMF. The spatial spectrum shows a dispersive feature consistent with satellite observations, with higher energy particles at lower latitudes and lower energy particles at higher latitudes.

The simulation reveals (1) how and where particles are transmitted from the solar wind into the magnetosphere via direct magnetic reconnection on the dayside; (2) how the features of the spectra are related to ongoing magnetic FTEs; (3) how the motion of the cusp, particularly the latitudinal variation of the open/closed field line boundary, is correlated with the dayside reconnection and reflected in the spectra, energy flux due to precipitating ions as a function of time.

Third, the energy spectra of cusp precipitating ions and magnetopause reconnection under an IMF of a finite B_y component are investigated. It is found that component reconnection is the reconnection process at the dayside magnetopause. Dispersive feature is also shown in spatial spectra for precipitating ions in the cusp, compared to that under a purely southward IMF. When IMF clock angle is larger than 180°, the heaviest precipitation shifts to the dawn side.

Acknowledgments

I want to thank my supervisor Dr. Lin whose advice and encouragement guided me in the process of research and writing of this thesis. At the Physics Department, I owe a debt of gratitude to all the professors and staff. Thanks in particular to Dr. J. D. Perez and Dr. Xueyi Wang for invaluable discussions, and to Dr. Ming-kuo Lee, Dr. Stephen Knowlton, Dr. Satoshi Hinata for taking the time to review my thesis.

I would also like to thank my family and all my dear friends for their precious support through this.

Table of Contents

List of Figures

List of Abbreviations

1-D	One Dimensional
2-D	Two Dimensional
3-D	Three Dimensional
ASCII	American Standard Code for Information Interchange
AU	Astronomical Unit
CME	Coronal Mass Ejection
FTE	Flux Transfer Event
HDF	Hierarchical Data Format
LLBL	Low Latitude Boundary Layer
MHD	Magnetohydrodynamic
PIC	Particle-in-cell

Chapter 1

An Introduction to Magnetopause Reconnection

The purpose of this chapter is to provide background knowledge to prepare readers for the following chapters by trying to make the thesis a self-contained piece.

Magnetopause reconnection is referred to magnetic reconnection that occurs near the outermost boundary of the Earth's magnetic field in this thesis. In the next few sections, we first give a brief overview of magnetic reconnection and some basics of solar wind as the external plasma source for reconnection, then we will review current progress on dayside magnetopause reconnection, e. g., flux transfer events (FTEs). The last section of this chapter compares different simulation models used in space plasma physics.

1.1 A Brief Overview of Magnetic Reconnection

Magnetic reconnection, namely, is the process that two magnetic field lines bend towards each other and fuse to create new field lines. The concept of motion of magnetic field lines is closely connected with the magnetohydrodynamic (MHD) description of plasmas as follows [*Priest and Forbes*, 2000a].

As we all know, Faraday's law gives

$$\frac{\partial \mathbf{B}}{\partial t} = -\nabla \times \mathbf{E}, \tag{1.1}$$

where $\mathbf{B}$ is the magnetic field, $\mathbf{E}$ is the electric field and t is time. With the displacement current omitted, Ampére's law gives

$$\nabla \times \mathbf{B} = \mu_{\mathbf{0}} \mathbf{J}, \tag{1.2}$$

where $\mathbf{B}$ is the magnetic field, $\mathbf{J}$ is the current density. The Ohm's law in the resistive MHD can be written as,

$$\mathbf{E} + \mathbf{V} \times \mathbf{B} = \eta_{\mathbf{e}} \mathbf{J}, \tag{1.3}$$

where η_e represents the scalar electrical resistivity. Combine Equation 1.1, 1.2 and 1.3, the magnetic induction equation is obtained as

$$\frac{\partial \mathbf{B}}{\partial t} = \nabla \times (\mathbf{V} \times \mathbf{B}) + \eta \nabla^{\mathbf{2}} \mathbf{B}, \tag{1.4}$$

where $\eta = \frac{\eta_e}{\mu_0}$ is the magnetic diffusivity. The first term on the right hand side of Equation 1.4 is the contribution to $\frac{\partial \mathbf{B}}{\partial t}$ from field convection, and the second term is the contribution from field diffusion.

The ratio of the two terms, the magnetic Reynolds number, is defined as

$$R_m = \frac{L_0 V_0}{\eta}, \tag{1.5}$$

where L_0, and V_0 are typical length and velocity scales, respectively. If $R_m \gg 1$, the convection dominates over the diffusion and Equation 1.4 becomes

$$\frac{\partial \mathbf{B}}{\partial t} = \nabla \times (\mathbf{V} \times \mathbf{B}), \tag{1.6}$$

which leads to the 'frozen-in' theorem of the ideal MHD as describe below.

In Figure 1.1, a closed loop of plasma elements $l(t)$ at time t moves to $l(t + dt)$ at time $t + dt$, where $t + dt$ and t are two successive instants. During this process, the change of the magnetic flux enclosed by the closed loop of plasma at t can be written as

$$\frac{d}{dt} \int \mathbf{B} \cdot \mathbf{dS} = \int \frac{\partial \mathbf{B}}{\partial \mathbf{t}} \cdot \mathbf{dS} + \oint \mathbf{B} \cdot (\mathbf{V} \times \mathbf{dl}), \tag{1.7}$$

where $\mathbf{S}$ is the vector area enclosed by the loop. The first term on the right hand side of Equation 1.9 is due to the time variation of the magnetic field, and the second term is due to the motion of the plasma loop. Since the vector identity gives

$$\mathbf{B} \cdot (\mathbf{V} \times \mathbf{dl}) = (\mathbf{B} \times \mathbf{V}) \cdot \mathbf{dl}, \tag{1.8}$$

Equation 1.7 can be written as

$$\frac{d}{dt} \int \mathbf{B} \cdot \mathbf{dS} = \int \frac{\partial \mathbf{B}}{\partial \mathbf{t}} \cdot \mathbf{dS} + \oint (\mathbf{B} \times \mathbf{V}) \cdot \mathbf{dl}. \tag{1.9}$$

Recall Equation 1.6, we have

$$\frac{d}{dt} \int \mathbf{B} \cdot \mathbf{dS} = \int \nabla \times (\mathbf{V} \times \mathbf{B}) \cdot \mathbf{dS} - \oint (\mathbf{V} \times \mathbf{B}) \cdot \mathbf{dl}. \tag{1.10}$$

Applying Stokes' theorem, we find that the right side of Equation 1.10 is identically equal to zero. In another word, the magnetic field and the plasma elements are 'frozen-together' so that the plasma elements move with magnetic field lines and the plasma within a magnetic flux tube always stays inside the same flux tube. If the 'frozen-in' condition always holds, magnetic reconnection never happens, which is defined below.

Let us consider another limit. When $R_m \ll 1$, the diffusion dominates over the convection, and Equation 1.4 becomes

$$\frac{\partial \mathbf{B}}{\partial t} = \eta \nabla^2 \mathbf{B}, \tag{1.11}$$

which is actually a diffusion equation that implies the magnetic field variation diffuses away the same as the heat diffuses when a temperature gradient exists.

However, we see a more complicated behavior of magnetic field than a simple diffusion process when the 'frozen-in' condition no longer holds, where field lines are no longer frozen-in the plasma elements.

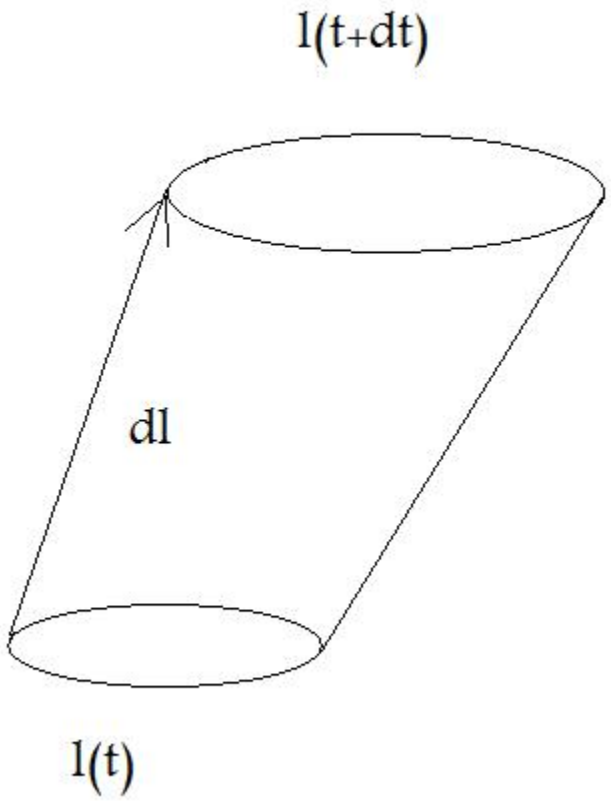

Figure 1.1: Frozen-in theorem of ideal MHD: a closed loop of plasma elements $l(t)$ at time t moves to $l(t + dt)$ at time $t + dt$

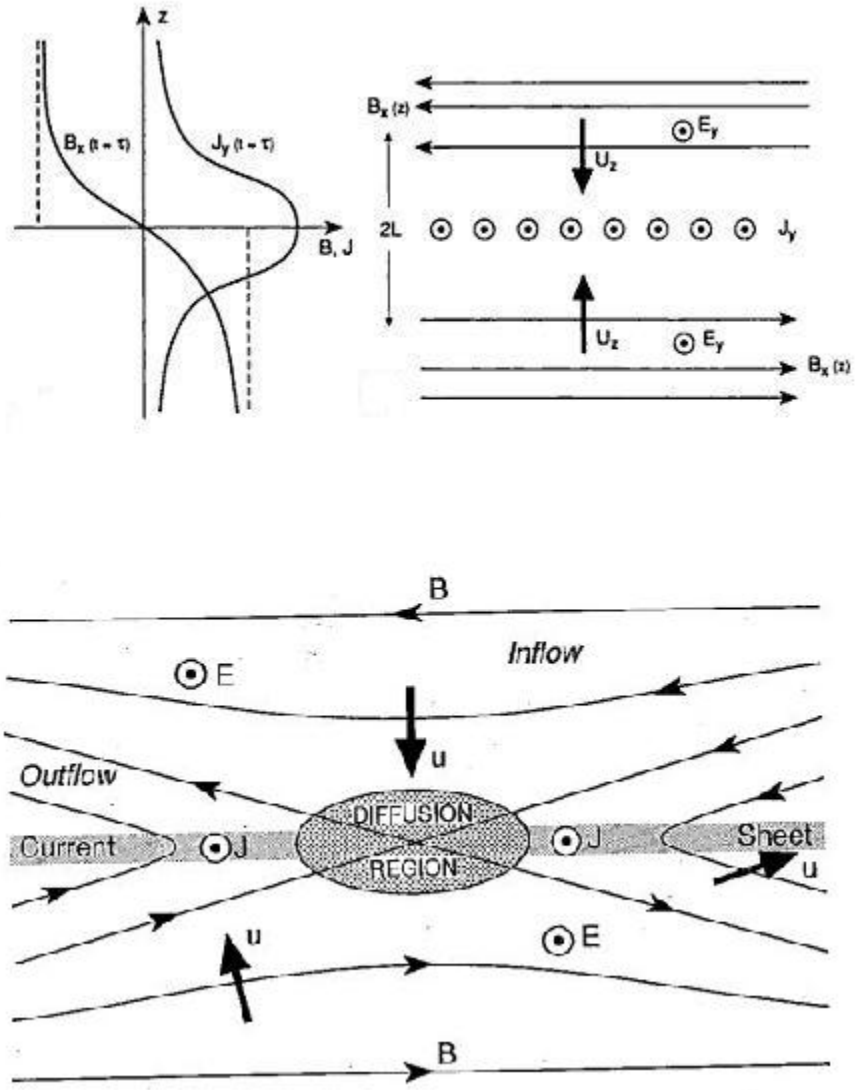

Figure 1.2: Illustration of magnetic reconnection in the $x - z$ plane. Magnetic field strength and current density variation along the z axis, corresponding to the current sheet shown in the upper right plot (upper left); Initial conditions of magnetic reconnection, which consists of a current sheet in the y direction, the inflow of magnetic flux as well as the plasma towards the $z = 0$ plane (upper right); Illustration of magnetic reconnection occurrence near an X line (lower panel). Adapted from *Hughes* [1995]

Figure 1.2 illustrates the concept of magnetic reconnection in the Cartesian coordinate system, where the magnetic field possess anti-parallel components across the current sheet. As shown in the upper right plot, the plane of the current sheet lies in the y direction at $z = 0$ while the inflow of magnetic flux as well as plasma towards the $z = 0$ plane. The upper left plot gives the variation of the corresponding magnetic field strength and current density along the z axis.

The lower panel of Figure 1.2 illustrates the occurrence of magnetic reconnection. The plasma and magnetic field convect in from the top and bottom uniform plasma region and towards the $z = 0$ plane. At the center of the current sheet, there is a diffusion region, where $R_m < 1$ and plasma elements are not tied to field lines. Note that R_m is proportional to L_0 so that the thinner the current sheet is, the smaller R_m is. Because electrons have much smaller mass than ions do, the diffusion region of electrons during reconnection is of smaller size than the diffusion region of ions. At the center of the diffusion region, the intersection of the X-type separatrices is the X point in the xy plane. The X point is the projection of a singular line (X line) in the 3-D space onto the xy place, near which reconnection occurs and the magnetic field has an X-type configuration. A more rigorous definition will be given in Chapter 4.

So qualitatively, the reconnection process is such that magnetic field lines from different magnetic domains are spliced to one another, changing their patterns of connectivity with respect to the sources. The inflow plasma slide across the field lines in the diffusion region, leading to the formation of an outflow region where the plasma flows out towards the left and right. In the MHD description, magnetic reconnection occurs on timescales intermediate between the slow resistive diffusion of the magnetic field and the fast Alfvénic timescale. During magnetic reconnection, stored magnetic energy is released in the form of thermal energy and kinetic energy of plasm particles.

Magnetic reconnection is a fundamental process in in both space and laboratory plasmas. In solar physics, it is believed that magnetic reconnection explains the ejection of coronal

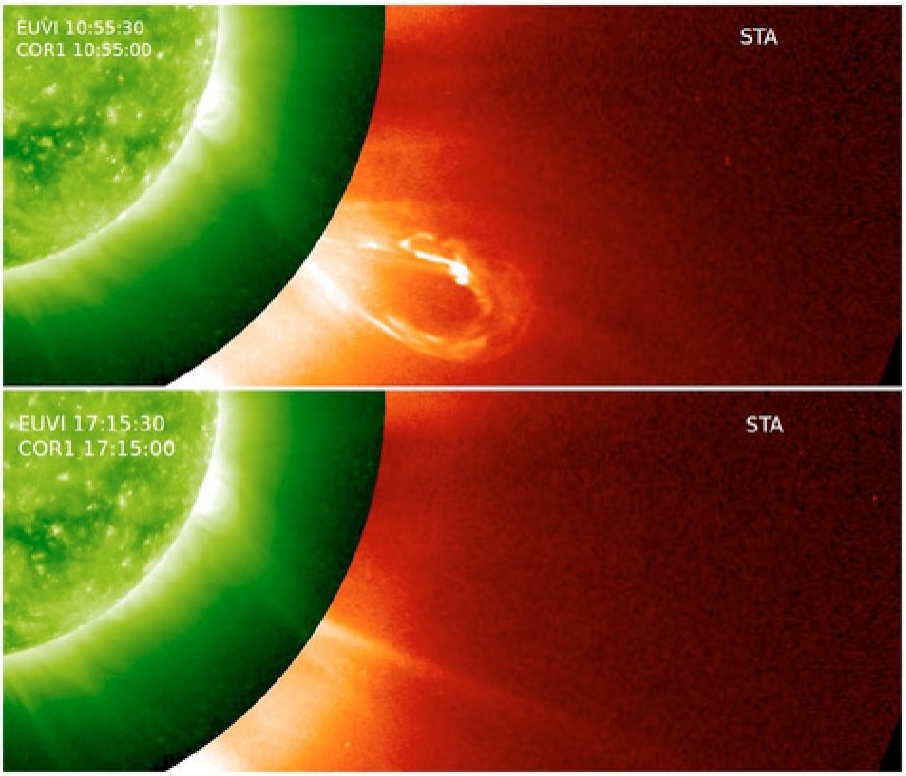

Figure 1.3: An event of emerging coronal matter ejection. Adapted from *Patsourakos and Vourlidas* [2011]

matter from the Sun [*Antiochos et al.*, 1999]. Figure 1.3 shows an event of emerging coronal matter ejection. In magnetospheric physics, reconnection is believed to be closely connected with the aurora intensification under some circumstances, Flux Transfer Events (FTEs) in the current sheet at the dayside magnetopause [*Russell and Elphic*, 1978; *Lee and Fu*, 1985; *Russell et al.*, 1995; *Scholer et al.*, 2003; *Raeder*, 2006; *Dorelli and Bhattacharjee*, 2009] and in the magnetotail plasma sheet. For laboratory plasmas, reconnection is important to the science of controlled nuclear fusion because it may cause the failure of magnetic confinement.

1.1.1 Basics of the Solar Wind

The first source of plasma, solar wind, is a fully ionized plasma that carries the interplanetary magnetic field (IMF) and streams continuously outward from the Sun into the solar system. In this section, some basics of the solar wind are introduced.

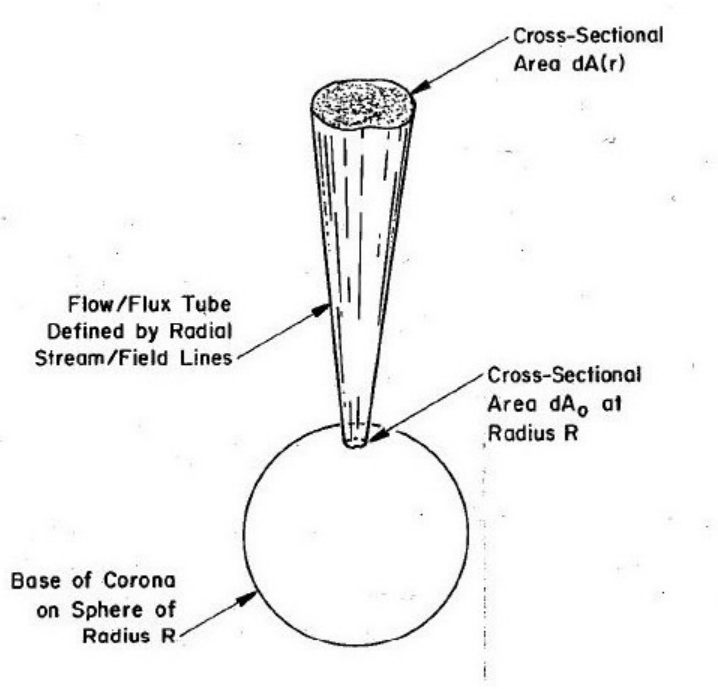

Figure 1.4: Geometry of a flow (or flux) tube defined by radial streamlines, adapted from *Hundhausen* [1995]

The Sun can be seen as a magnetohydrodynamic dynamo, which generates magnetic field and plasmas flow outwardly from the base of the corona sphere. If we do not consider the rotation of the Sun first, the classical picture of an outwardly moving solar wind should be the one shown in Figure 1.4. According to the frozen-in field line condition, the magnetic structure is consistent with the plasma flow. In another word, if a plasma flux tube exists, the corresponding identical magnetic flux tube exists too.

The simple picture in Figure 1.4 becomes more complicated as the Sun rotates with an average period of 25.4 days. The upper left plot of Figure 1.5 illustrates the magnetic field configuration around the sun if there is no rotation, while the upper right plot of Figure 1.5 illustrates the magnetic field configuration around the sun, considering the rotation of the Sun. The lower panel of Figure 1.5 shows the Earth's orbit in the spiral magnetic field lines from the Sun. Also shown in the lower panel of Figure 1.5, the magnetic field $\mathbf{B}$ is

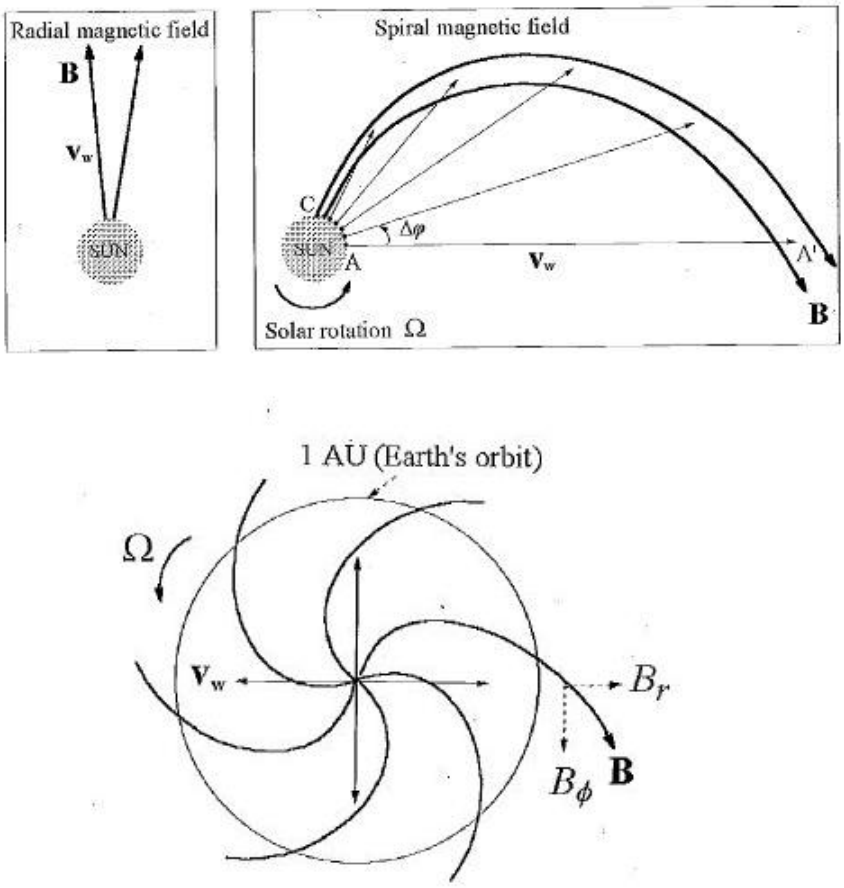

Figure 1.5: (Upper left) Magnetic field lines drawn by the radially expanding solar wind, assuming the Sun is not rotating; (Upper right) The spiral field lines illustrate the impact of the rotation of the Sun on the magnetic field geometry. $\mathbf{V_w}$ is the radial velocity of the fluid. (Bottom) the Earth's orbit in the spiral magnetic field lines from the Sun. This figure is adapted from [*Meyer-Vernet*, 2007]

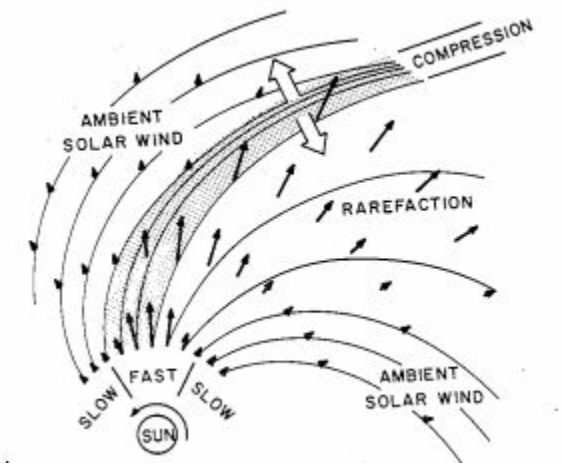

Figure 1.6: Illustration of the interaction of fast and slow solar wind as the substructure of solar wind, adapted from *Pizzo* [1985]

approximately radial at small distances while at large distances, the azimuthal component of **B** becomes dominant.

Across the equatorial plane, **B** changes direction dramatically and gives rise to a current sheet. Note that in reality the solar dipole field is not aligned to the rotation axis, which causes the deformation of the current sheet so that the current sheet has a similar shape to a twirled ballerina skirt as shown in Figure 1.7.

As a result, the Earth moves above and below the warped current sheet alternatively at a distance to the Sun of 1 astronomical unit (AU). Note that 1 AU is approximately the mean Earth-Sun distance. In another words, the IMF at the Earth could possibly be in any directions, including both 'northward' and 'southward'.

The speed of the solar wind usually measures as low as $300 - 400km \cdot s^{-1}$ at sector boundaries while the fast solar wind measures as high as $700km \cdot s^{-1}$. The interaction of fast and slow solar wind is shown in Figure 1.6, which is one of the major perturbations in the solar wind. Other important perturbations in the solar wind include shocks, which form when the solar wind is compressed at speeds greater than the phase speed of the related waves, and coronal mass ejections (CME) .

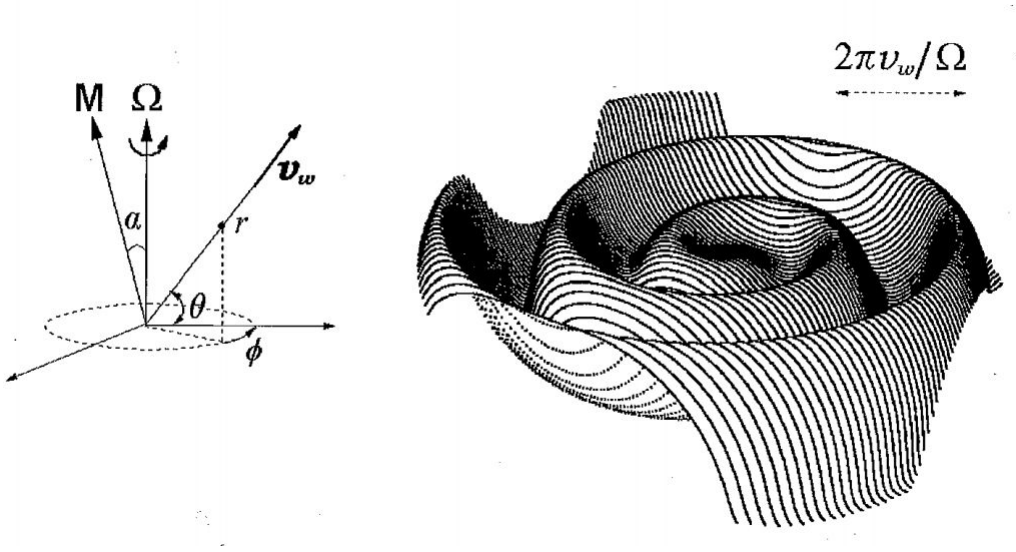

Figure 1.7: Deformation of the current sheet (the shadowed surface) by a tilt angle α of the Sun's magnetic axis ($\mathbf{M}$) with respect to the rotation axis ($\mathbf{\Omega}$) with a constant solar wind radial velocity, adapted from *Meyer-Vernet* [2007]

Hydrodgen is not the only element in the solar wind. Helium is the second most abundant element. The ratio n_a/n_p is about $0.04 - 0.05$, where n_a is the number of helium ions per unit volume and n_p is number density of protons [*Meyer-Vernet*, 2007].

1.2 Magnetospheric Configuration and Reconnection at the Magnetopause

The first concept of the Earth's magnetosphere was deduced by Sydney Chapman and his student Vincenzo Ferraro in the early 1930s [*Akasofu*, 1974]. The first concepts of open magnetosphere and magnetic reconnection were proposed by *Dungey* [1961], which explained why the convection pattern of plasma in the high latitude is dependent on the direction of the IMF.

Figure 1.8 shows the magnetospheric configuration in the noon-midnght meridian plane under a southward IMF, implying the convection of plasma within the magnetosphere driven by the magnetic reconnection. The Earth's intrinsic field is approximately a magnetic dipole in the first order. As solar wind flows against the dipole field, the bow shock and magnetopause shown in dashed lines are the two boundaries. Note that the bow shock is the curved,

stationary shock wave where the super sonic solar wind past the Earth. The magnetopause is the boundary between the solar wind and the geomagnetic field. Inside the magnetopause, the region is called magnetosphere, while the region between the magetopause and the bow shock is the magnetosheath. The magnetosheath is the shocked solar wind.

In Figure 1.8, the red cross near the subsolar region of the magnetopause current sheet indicates the location of the field neutral point at the dayside magnetopause under a southward IMF, where favors magnetic reconnection. Some field lines are numbered to show the succession of field line configuration. Under the southward IMF, a new field line (2) forms after reconnection between field line (1) and (1') at the dayside magnetopause. The newly reconnected field lines convect tailward. As the reconnection proceeds, more originally "closed" geomagnetic field lines become "open". There is another reconnection site where field line (6) and (6') reconnects in the tail. Magnetic reconnection at the dayside primarily leads to magnetic energy storage rather than the covert of magnetic energy into kinetic and thermal energy as it does at the night side [*Cowley*, 1980].

The inset shows the foot print of the numbered field lines in the norther high-latitude ionosphere. The solid line with arrows in the inset indicate high-latitude plasma flows correspondingly antisunward in the polar cap and returns to the dayside at lower latitude.

Now, magnetic reconnection at the magnetopause is believed to be a fundamental process that leads to the transfer of the solar wind mass, momentum, and energy into the Earth's magnetosphere [*Cowley*, 1996]. Satellite observations have identified both transient and quasi-steady reconnection at various locations on the magnetopause under various IMF conditions [*Russell and Elphic*, 1978; *Paschmann et al.*, 1982; *Sonnerup et al.*, 1981; *Fuselier et al.*, 1991; *Lockwood and Smith*, 1992; *Scholer*, 1989a; *Phan et al.*, 2005].

A flux transfer event (FTE) is a characteristic set of perturbations in the magnetic field observed by spacecraft in the vicinity of the terrestrial magnetopause , which was first observed by the International Sun-Earth Explorer-1 and -2 satellites in 1978 [*Russell and Elphic*, 1978]. Because of their regular appearance and easy identification, FTEs attract

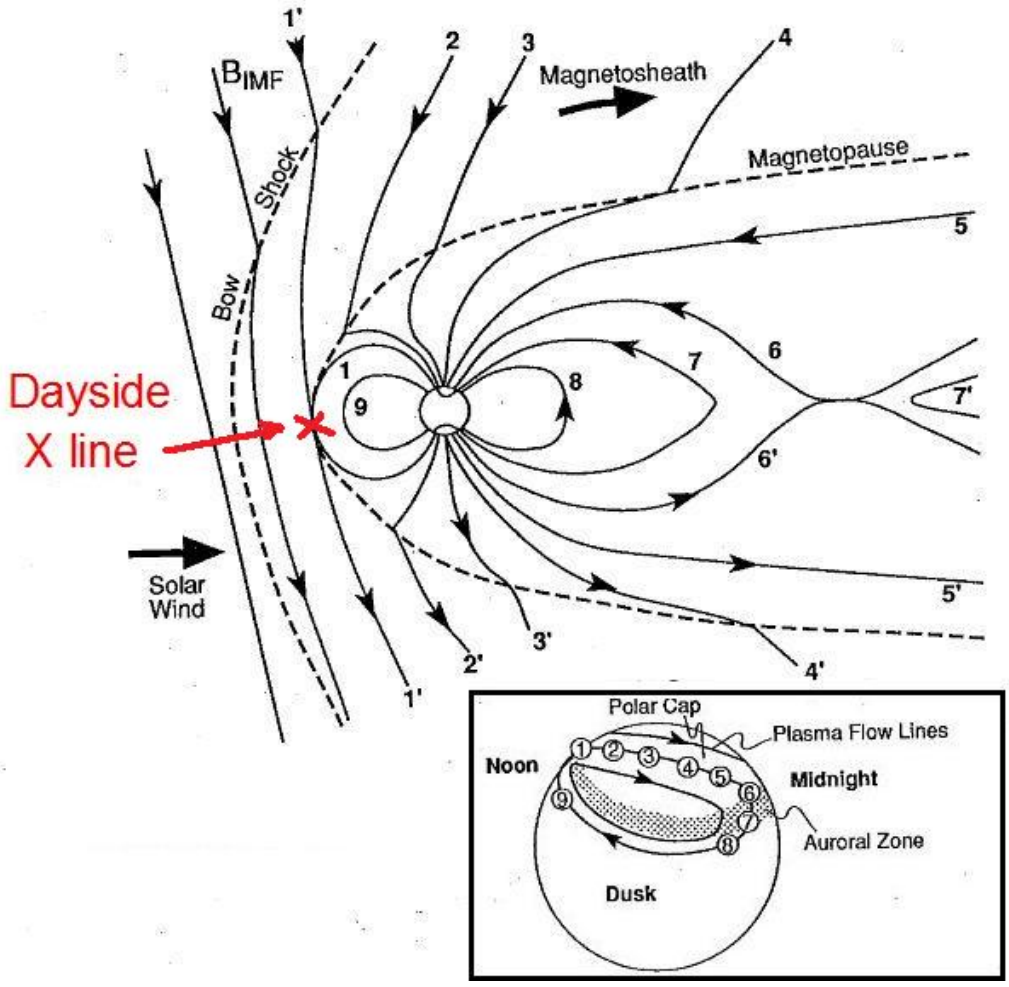

Figure 1.8: Magnetospheric configuration in the noon-midnght meridian plane under a southward IMF, showing the convection of plasma within the magnetosphere driven by the magnetic reconnection. The field lines are numbered to show the succession of field line configuration. The inset (lower right) shows the position of the footprint of the numbered field lines in the northern high latitude ionosphere. Adapted from *Hughes* [1995].

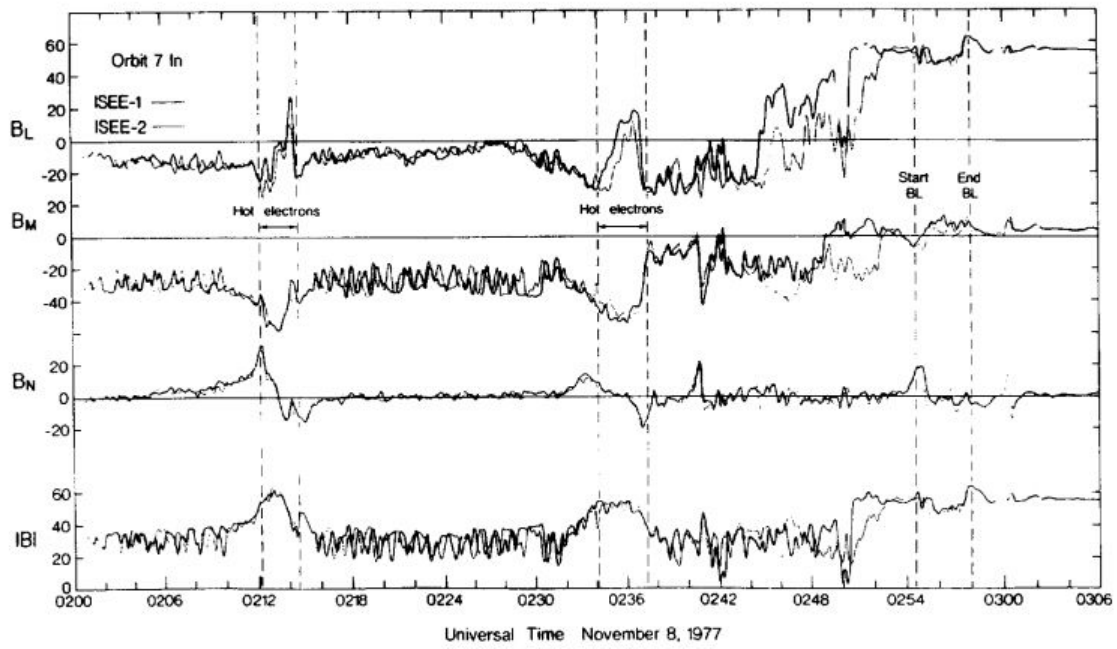

Figure 1.9: Magnetic field during a clear example of an FTE, where the magnetic field is expressed in boundary normal coordinates with B_n outward along the boundary normal, B_l along the projection of the field in the magnetosphere and B_m completing a right-handed set. Adapted from *Russell et al.* [1995]

a lot of attention. Figure 1.9 shows the magnetic field during a clear example of an FTE [*Russell et al.*, 1995], where the magnetic field is expressed in boundary normal coordinates with B_n outward along the boundary normal, B_l along the projection of the field in the magnetosphere and B_m completing a right-handed set. The signatures of an FTE include a bipolar variation in the magnetic field component normal to the magnetopause B_n and simultaneous deflection in the tangential components [*Uberoi*, 2003].

An FTE is limited in space and the quasi-period of the reoccurrence is around 8 minutes [*Rijnbeek et al.*, 1984] . So far, an FTE is thought to be a typical transient magnetic reconnection occurrence because of its strong control by the direction of the IMF [*Russell*, 1995]. Once the IMF turns southward, the occurrence rate of FTEs increases sharply.

Figure 1.10 shows a simple schematic model proposed by *Russell and Elphic* [1978], which explains the main magnetic signatures of FTEs. FTEs were thought to be flux tubes

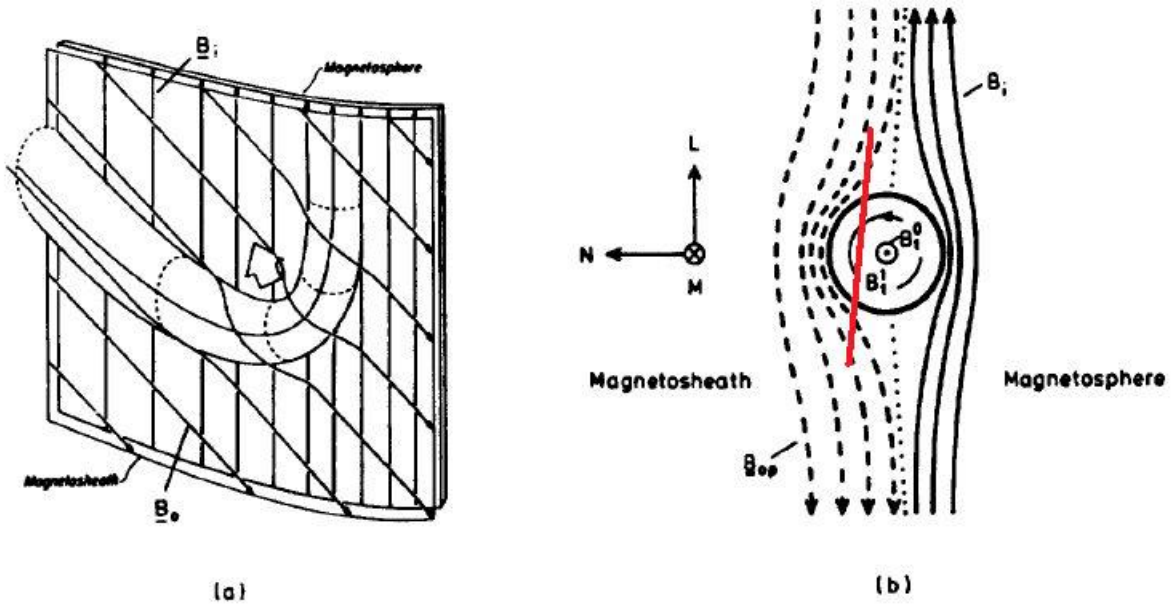

Figure 1.10: Schematic diagram of the structure of an FTE, proposed by *Russell and Elphic* [1978]. On the left a bundle of flux tubes is shown having become connected between the magnetosheath (foreground) and magnetosphere (background), and on the right the bulge in the magnetosheath and magnetospheric fields is illustrated. A virtual satellite passing as marked with the red line leads to the bipolar signature of B_n. Adapted from *Russell and Elphic* [1978]

that connect geomagnetic field and the IMF. If the satellite flies through the flux tube with a path in red lines in Figure 1.10, the variation of the normal component of the magnetic field in the local normal coordinates has a bipolar signature. Later, *Lee et al.* [1993] argued that FTEs could be generated in the process of multiple X-line reconnection(MXR). As shown in Figure 1.11, the flux rope that generates the signatures of FTEs is formed between X lines denoted with heavy bars, which have finite length and in parallel with the current sheet. There are six possible patterns of field lines configuration of the magnetic flux rope.

And even today, people have not stopped asking questions about FTEs since then. Is there any possibility that an FTE is not caused by reconnection? Can we divide FTEs into different categories? What is the internal structure of FTEs? What trigger FTEs? What is the relationship between FTEs and the separatrices of magnetic reconnection? How do FTEs evolve? Do reconnection rate vary during the life cycle of an FTE?

Overall, FTEs are transient reconnection occurrences. Another category of reconnection events have a much longer time scale, which are considered to be steady, or quasi-steady. Except for the time scale, they also have a magnetic field configuration as they are usually associated with a single X line.

P. A. Sweet and E. N. Partker in 1950s [*Priest and Forbes*, 2000a] were the first to develop a simple MHD model of steady-state reconnection in a current sheet formed at a null point, which is often referred to as a model for slow reconnection. Petschek [*Petschek*, 1964] later developed an alternative model with a current sheet whose length is many order of magnitude smaller than the Sweet-Parker model. Petschek's reconnection model can predict a faster reconnection rate than that predicted by the Sweet-Parker model, also for steady-state reconnection with a single X line.

As shown in the upper plot of Figure 1.12, Petschek's [*Petschek*, 1964] reconnection models a symmetric case with equal plasma density, equal magnetic strength, and antiparallel magnetic fields on the two sides of the current sheet. Plasma particles are accelerated through

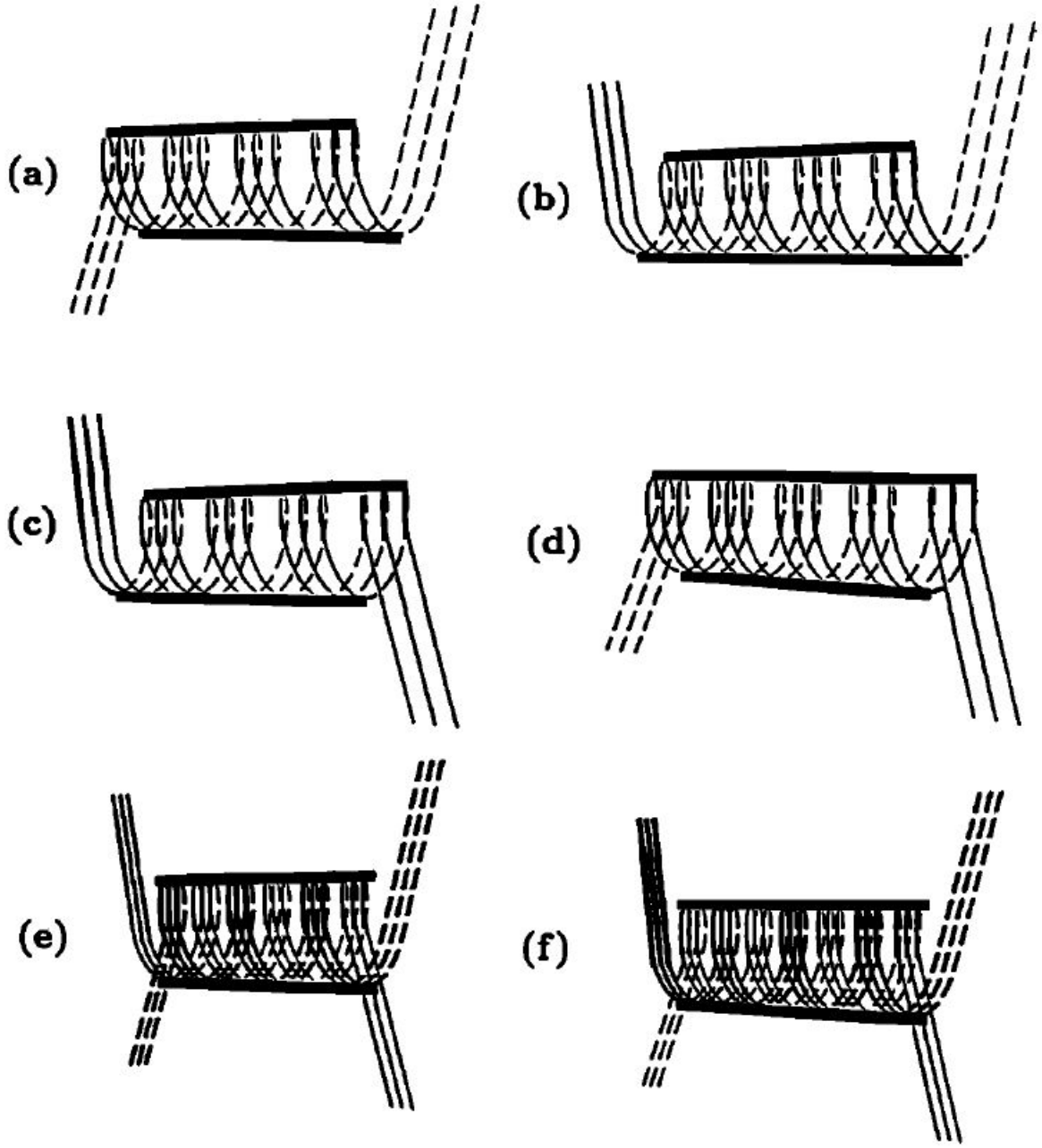

Figure 1.11: Six possible patterns of field lines configuration of the magnetic flux rope that can generate signatures of FTEs. The heavy bars denote the reconnection X lines. The solid and dashed lines are used to distinguish field lines on different side of the current sheet. Adapted from *Lee et al.* [1993]

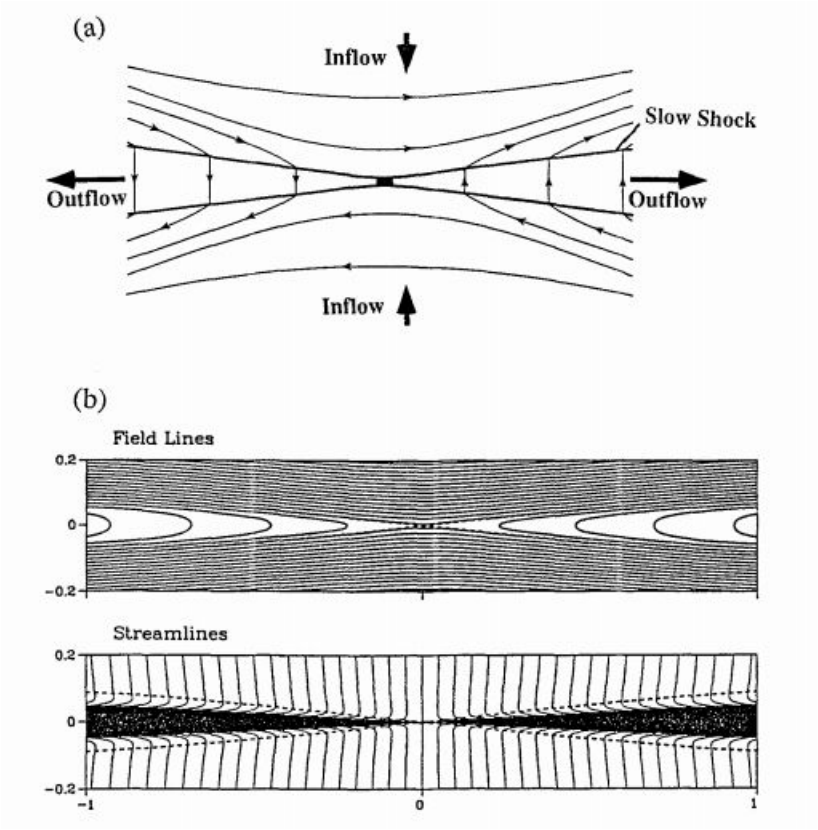

Figure 1.12: (a) Petschek's symmetric reconnection model which consists of the inflow region, the outflow region, and the small central diffusion region as shown in the dark area. (b) Magnetic field lines and stream lines of plasma flow in a MHD simulation [*Yan et al.*, 1992]. Adapted from *Lin and Lee* [1994]

the two slow shocks in the current layers. Note that the slow shocks are located downstream of the sparatrices as indicated in the lower panel of Figure 1.12.

The steady reconnection at the dayside magnetopause is an asymmetric case as first modeled by *Levy et al.* [1964]. In this model, the magnetic field strength on one side is larger than that on the other side, and the plasma density is set to be zero on the side of a higher field. The result is shown in Figure 1.13, where the two slow shocks are replaced by a rotational discontinuity and a slow expansion wave. The magnetic field changes direction cross the rotational discontinuity (an MHD discontinuity) , and high speed plasma flow along the current layer. Note that an MHD discontinuity is a thin transition region, across which the plasma density, magnetic field, flow velocity etc. satisfy a set of jump conditions [*Lin and Lee*, 1994].

Besides theoretical work for steady reconnection, observations [*Gosling et al.*, 1990] pointed out that quasi-steady reconnection indeed occurs at the dayside magnetopause.

Figure 1.14 shows a series of simultaneous 2-s snapshots of 2-D ion (above) and electron (below) velocity distribution functions during an outward traversal of the earthward edge of the low latitude boundary layer (LLBL) from the magnetosphere, which is identified as a quasi-steady reconnection event. As shown in the lower row, the evolution of the hotter population is consistent with their escape into the magnetosheath on newly reconnected field lines with the most field-aligned electron escaping first. Note that the vector (black arrow) shows the projection of the magnetic field onto the xy plane. More analysis on this event shows that the electron edge of the LLBL lies closer to the separatrix of the corresponding reconnection site that does the ion edge, which is consistent with the fact that the electron diffusion region of reconnection is samller than ion diffusion region. Thus, the author drew a diagram, showing the magnetopause region for quasi-stationary reconnection as in Figure 1.15

For a quasi-steady single X-line reconnection case, the velocity space distributions of ions just inside the magnetopause in the magnetosphere are expected to have a D-shaped

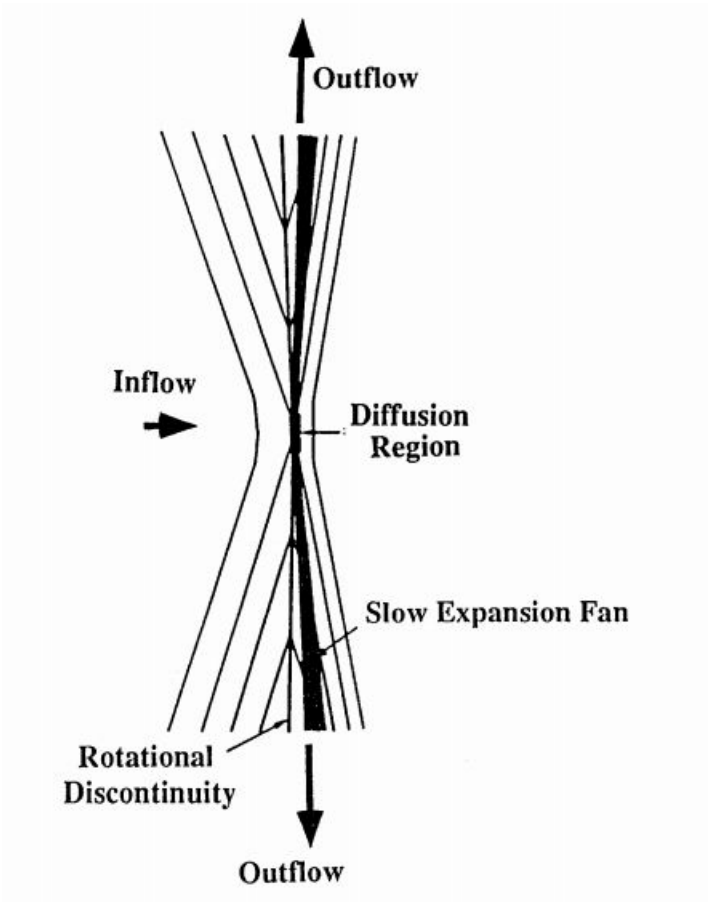

Figure 1.13: Asymmetric reconnection model by *Levy et al.* [1964]. A rotational discontinuity and a slow expansion wave are presented in the reconnection layer. Note that the plasma density decreases slowly to zero at right hand side of the current sheet. Adapted from *Lin and Lee* [1994]

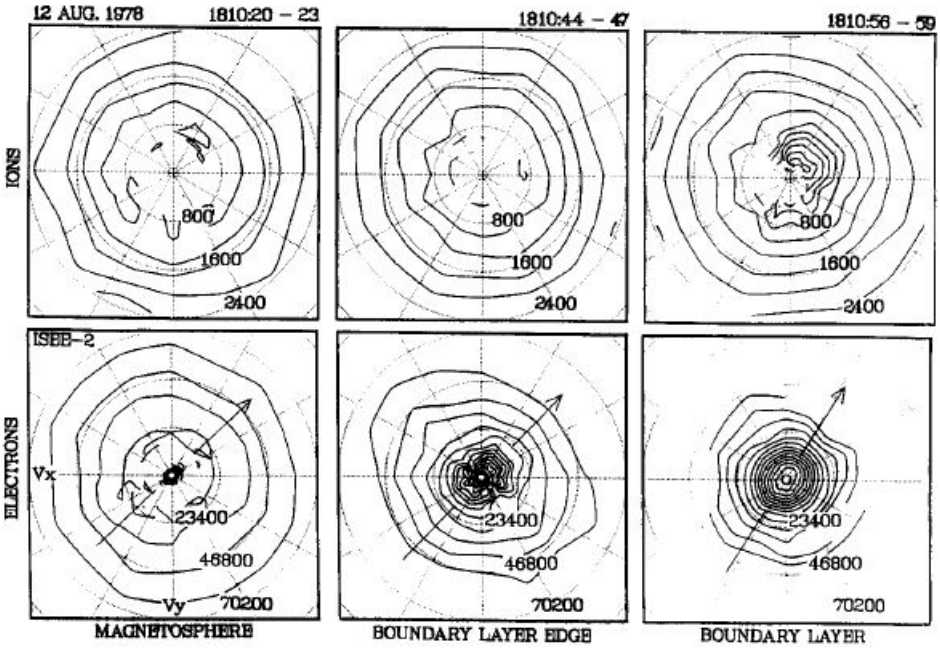

Figure 1.14: A series of simultaneous snapshots of 2-D ion (above) and electron (below) velocity distribution functions during an outward traversal of the earthward edge of the LLBL on August 12, 1978. The distribution are shown as contours of constant phase-space density separated logarithmically, (two contours per decade). Numbers on the dotted circles indicate the velocity scale in km/s. Vectors drawn represent the projection of the magnetic field onto the xy plane. Adapted from *Gosling et al.* [1990]

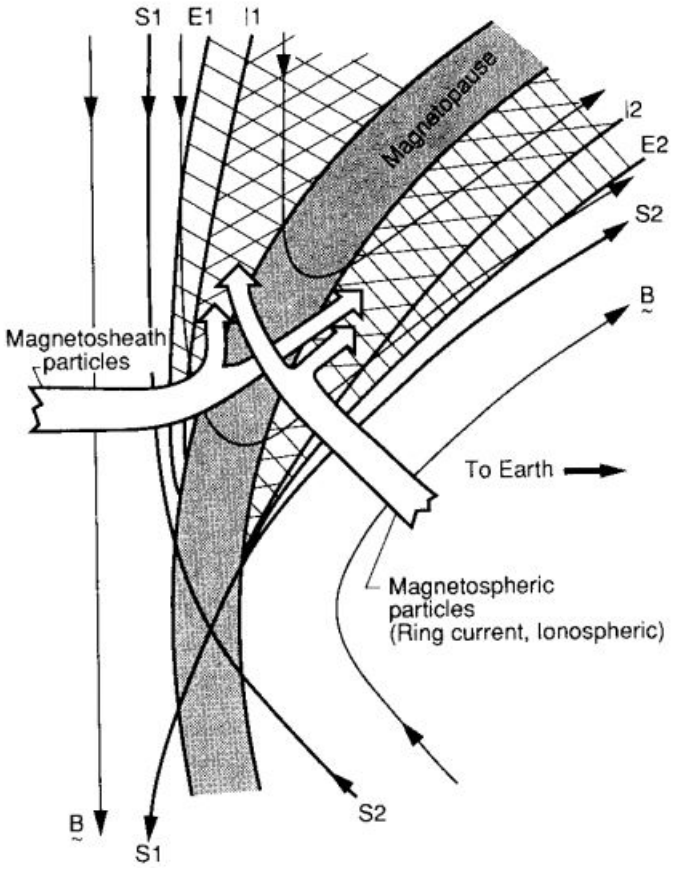

Figure 1.15: Sketch of the magnetopause region for quasi-stationary reconnection. Adapted from *Gosling et al.* [1990]

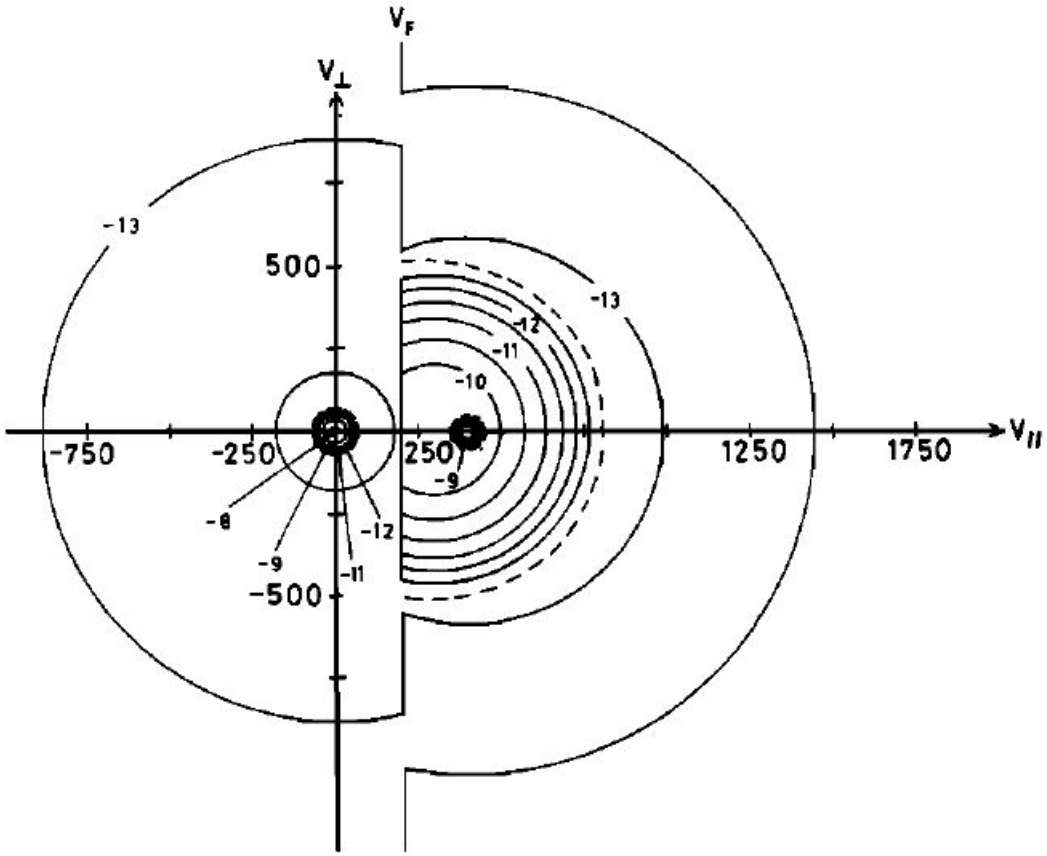

Figure 1.16: Illustration of velocity space distributions of ions expected just inside the magnetopause in the magnetosphere for a quasi-steady single X-line reconnection case. The contours are of constant distribution functions marked with value of $log_10 f(s^3 m^{-6})$), the accelerated D-shaped distributions are simply taken to be a mirror image of the inflowing distributions, reflected in the plane $V_\parallel = V_F$, where the de Hoffmann-Teller velocity V_F has been taken to be $200 kms^{-1}$.Adapted from *Cowley* [1982]

distribution for magnetosheath transmitted ions, which is illustrated in Figure 1.16. Since only the particles with parallel velocity toward the magnetosphere in the reference frame of field line convection can penetrate to the Earth, the accelerated D-shaped distributions have a low $V_{\parallel}$ cut-off at $V_{\parallel} = V_F$, where V_F is the de Hoffmann-Teller velocity. Except for the magnetosheath sourced ions, ion populations of cold magnetospheric ion of ionosphere origin is also one of the main ion populations [*Cowley*, 1982] at the location as shown in Figure 1.16.

As shown above, satellite data supports the argument that reconnection could be a very important process in magnetospheric physics. But in most cases, the satellite crossings not through the electron diffusion region of reconnection directly. Thus, although various observations have implied reconnection sites under various IMF and solar wind conditions [*Marcucci and Polk*, 2000; *Trattner et al.*, 2007] based on certain models/methods, there has been few observations simultaneously in both the diffusion and the outflow regions that justify the implied location of reconnection. Plus, observations of the magnetopause reconnection have often generated contradictory opinions [*Fuselier et al.*, 2000; *Russell et al.*, 2000]. Figure 1.17 shows an example that for the same event, *Fuselier et al.* [2000] connected the event with component reconnection equatorward of the cusp and considered a negative cut-off velocity as an artifact at location M while [*Russell et al.*, 2000] treated the negative cut-off velocity as valid data, which indicated a slow-drifting of plasmas outside the current sheet. As a result, two groups inferred the reconnection sites to different locations as shown in the cartoons of Figure 1.17. The controversy is whether component reconnection occurred equatorward of the cusp. For complex plasma process in the magnetosphere, computer simulation are often used to help scientist to understand the process of reconnection at the magnetopause.

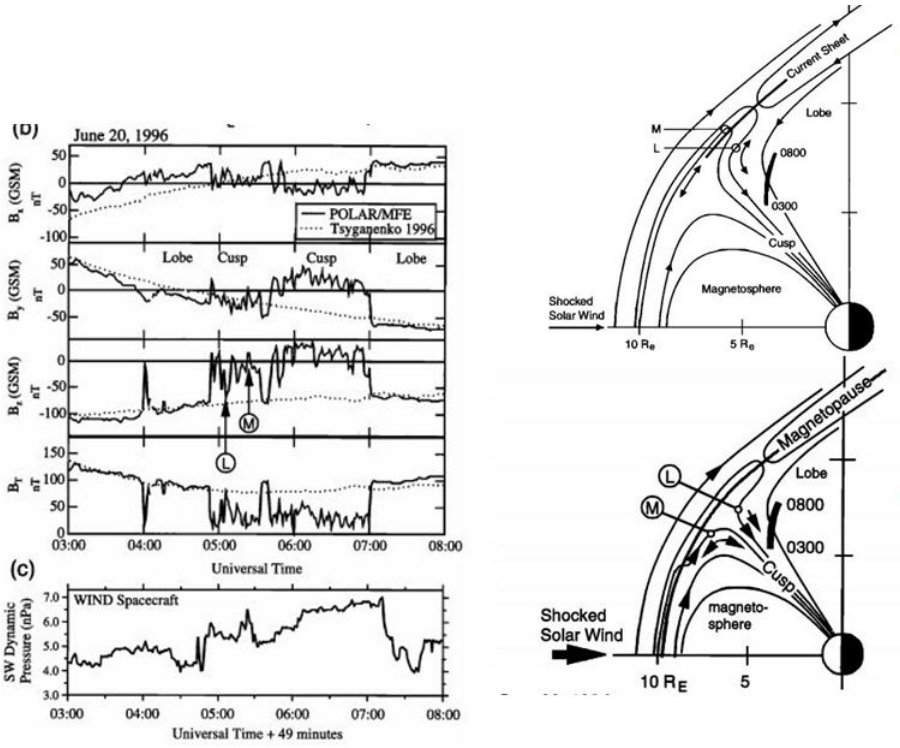

- The interpretation of June 20, 1996 event by *Fuselier et al [2000]*.
- The alternative interpretation of June 20, 1996 event by *Russell et al [2000]*.

Figure 1.17: Example that for the same event, two groups inferred the reconnection sites to different locations. Adapted from *Fuselier et al.* [2000] and *Russell et al.* [2000]

1.3 Types of Simulation Model in Space Plasma Physics

Today computers are utilized to solve equations to address problems in space plasma physics, which deal with multi-scale, multi-species, complex systems of plasmas. Generally, simulation models in space plasma physics fall into several categories: magnetohydrodynamic (MHD) models, 2-fluid or hall MHD models, hybrid models and fully kinetic particle-in-cell (PIC) models. In a kinetic model, a distribution function $f(\mathbf{x}, \mathbf{v}, \mathbf{t})$ of the kinetic species is introduced, where the variables $\mathbf{x}$,$\mathbf{v}$ and t are position, velocity and time, respectively. Kinetic models work in a way that the charges and currents are determined by the distribution functions self-consistently via Maxwell's equations.

In an MHD model, all plasma species are treated as a single or multiple fluid. MHD simulations have been carried out for the fluid properties and field line topology associated with reconnection [*Scholer*, 1989a,b; *Shi and Lee*, 1990; *Lin and Lee*, 1999]. Since the kinetic effects have been fully neglected, the behavior of kinetic waves generated in reconnection [*Chaston et al.*, 2005; *Lin and Lee*, 1994; *Kraussvarban and Omidi*, 1995], signature of non-Maxwellian particle transports as observed by satellites at the dayside magnetopause can not be explained by MHD models. The upside of using MHD models for global scale simulation is that MHD requires less computing resources, and thus can be used to investigate large scale structure of the magnetosphere.

In a PIC model, electrons and ions are treated as individual particles that move in imposed electric and magnetic field, where no approximations are made to the basic laws of mechanics, electricity and magnetism. The PIC models have been utilized to investigate the triggering mechanism of reconnection process [*Terasawa*, 1981; *Price et al.*, 1986; *Hoshino*, 1987; *Shay et al.*, 2001; *Hesse and Winske*, 1998]. It is found that the reconnection rate is insensitive to the mechanisms that initiate the reconnection at the X line [*Drake et al.*, 2003; *Birn et al.*, 2005; *Birn and Hesse*, 2001; *Shay et al.*, 2001; *Pritchett*, 2001; *Drake et al.*, 2005]. Due to the limited computing resources, most PIC models address reconnection problem in a way that the simulation domain is at the vicinity of the reconnection X line

and boundary conditions are applied locally. This may not be correct when it comes to the magnetopause reconnection as it is of a multi-scale, long-term evolution of the global system. Another concern of using PIC models for magnetopause reconnection is that some artifacts are introduced to expedite the simulation in PIC models. For example, proton to electron mass ratio much less than 1836 is adopted.

Hybrid models are between MHD and PIC models, in which one or more plasma species are treated as a single or multiple fluids, while the remaining species are treated kinetically as particles. The hybrid model in this thesis treats ions as particles, while electrons are treated as massless fluid. Sometimes electron inertial and non-gyrotropic pressure effects are also included in hybrid models [*Kuznetsova et al.*, 2000]. In general, the hybrid models are valid in studying the physics with wave frequency $\omega \approx \Omega_i$, and have been successful in explaining the structure of magnetic field, kinetic waves and the ion signatures observed in reconnection at the magnetopause [*Gosling et al.*, 1986]. 1-D and 2-D hybrid simulations have shown the presence of slow shocks and rotational discontinuities [*Lin and Lee*, 1994; *Lin*, 2001; *Lin and Swift*, 1996; *Nakamura and Scholer*, 2000] in collisionless reconnection and the structure of FTEs [*Karimabadi et al.*, 2005; *Omidi and Sibeck*, 2007].

1.4 Objectives and Outline of the Thesis

As shown in previous sections, magnetic reconnection is very important physical process at the dayside magnetopause when the magnetic shear across the magnetopause is large enough. The challenge to the understanding of FTEs in the magnetopause reconnection is that they are of 3-D nature, embedded in a multi-scale solar wind-magnetosphere global system, in which the ion physics is a very important. Inclusion of plasma kinetic physics is necessary for the modeling of the generation and evolution of magnetopause reconnection as well as the understanding of their internal structure. Although local simulations provide better resolution for processes which involve small scales, the 3-D global approach accommodates the interaction of different parts of the magnetosphere. So far, there has been no

such a model in the investigation of magnetic reconnection in the magnetosphere. Given the importance of magnetic reconnection in the global transport of the magnetosphere, it is expected that such a study will push forward our understanding of the transport process. By using a global-scale hybrid model, we aim to investigate:

(1) The magnetic field configuration under a southward IMF with or without the guide field B_y.

(2) The evolution and internal structure of FTEs caused by reconnection process after their onset.

(3) The quasi-steady reconnection under a purely southward IMF.

(4) The spectra of cusp precipitating ions associated with the dayside magnetopause reconnection.

In Chapter 2, our simulation model, initial and boundary conditions are explained in detail. In Chapter 3, the package for data visualization is introduced briefly. Starting from Chapter 4, we presents the simulation results from different IMF conditions. In Chapter 4, we represent the simulation results from 2 cases with a purely southward IMF, focusing on the field configuration and the evolution and internal structure of FTEs caused by reconnection. In Chapter 5, we explains the dayside magnetopause reconnection impact on the spectra of cusp precipitating ions under a purely southward IMF. In Chapter 6, we report preliminary simulation results from a case with a finite guide field B_y. In Chapter 7, we summarize and give a glimpse of future work.

Chapter 2

Global-Scale Hybrid Simulation Model

The global hybrid simulation scheme is described by *Swift* [1996] and implemented by *Lin and Wang* [2005] for 3-D simulations of the dayside magnetosphere. Note that our simulation addresses the reconnection processes within the dayside convection time scale and not for the entire global magnetosphere.

2.1 The Scheme

Except for the inner magnetosphere of $r < 7R_E$, the ions (protons) are fully kinetic particles, and the equation in the simulation units for ion motion, is given by

$$\frac{d\mathbf{v_i}}{dt} = \mathbf{E} + \mathbf{v_i} \times \mathbf{B} - \nu(\mathbf{V_i} - \mathbf{V_e}), \tag{2.1}$$

where $\mathbf{v_i}$ is the ion particle velocity, $\mathbf{E}$ is the electric field in units of ion acceleration, $\mathbf{B}$ is the magnetic field in units of the ion gyrofrequency [*Swift*, 1996] while $\mathbf{V_e}$ is the bulk flow velocities of the electrons and $\mathbf{V_i}$ is the particle ion bulk flow velocity. A small ad hoc current-dependent collision frequency, $\nu \simeq 0.01\Omega J/J_0$, is imposed in order to model ad-hoc anomalous resistivity and trigger magnetic reconnection in the simulation, where Ω is the local ion gyrofrequency and $J_0 = B_0/\mu_0\lambda_0$ (here λ_0 is the ion inertial length of the solar wind). A fluid approximation is used to model the inner magnetosphere of $r < 7R_E$, given that the fluid plasma in this region is not expected to affect the kinetics in the region of the magnetopause.

The electrons are treated as a massless fluid, and quasi charge neutrality is assumed in the calculation. The electric field is determined by the electron momentum equation

$$\mathbf{E} = -\mathbf{V_e} \times \mathbf{B} - \nu(\mathbf{V_e} - \mathbf{V_{ti}}) - \nabla \mathbf{P_e}/\mathbf{N}, \tag{2.2}$$

where $\mathbf{V_e}$ is the electron bulk flow velocity, $\mathbf{V_{ti}}$ is the total bulk flow velocity, P_e is the thermal pressure of electrons and N is the electron number density.

The total ion bulk flow velocity $\mathbf{V_{ti}}$ in Equation 2.2 is given by

$$\mathbf{V_{ti}} = \frac{\mathbf{n_i}}{\mathbf{n}}\mathbf{V_i} + \frac{\mathbf{n_f}}{\mathbf{n}}\mathbf{V_f}, \tag{2.3}$$

where the subscripts i an f stand for discrete particle and fluid, respectively and the n's are the densities. Note that at the radial distance $r \geq 7$ and as r increases, the particle ion bulk flow velocity $\mathbf{V_i}$is the dominant component for total ion bulk flow velocity.

The equation for fluid ion velocity is given by

$$\frac{d\mathbf{V_f}}{dt} = \mathbf{E} + \mathbf{V_f} \times \mathbf{B} - \nu(\mathbf{V_f} - \mathbf{V_e}) \tag{2.4}$$

The electron flow speed is evaluated from Ampere's law

$$\mathbf{V_e} = \mathbf{V_{ti}} - \frac{\nabla \times \mathbf{B}}{\alpha \mathbf{n}}, \tag{2.5}$$

where a constant $\alpha = (4\pi e^2/m_i c^2)$ is introduced. Note that $(\alpha n)^{\frac{-1}{2}}$ is the ion inertial length.

The magnetic field is updated by Faraday's law

$$\frac{\partial \mathbf{B}}{\partial t} = -\nabla \times \mathbf{E}. \tag{2.6}$$

The equations above then are written in a form more convenient for time-stepping, where magnetic field, particle motion and fluid term are kept while electric field $\mathbf{E}$ is eliminated.

The particle equations are advanced with one time step dt and the fluid and magnetic field equations are advance using $0.1dt$, one tenth of the time step used for the particle motion.

Note that magnetic field $\mathbf{B}$ is expressed as

$$\mathbf{B} = \mathbf{B_0} + \mathbf{B_1}, \tag{2.7}$$

where $\mathbf{B_0}$ is a time independent and curl-free portion and only $\mathbf{B_1}$ is updated.

As for the time-stepping algorithm, the velocities are known at the half time step, and the positions and fields are at the even time step. The fourth order Ronger-Kutta Method and the leapfrog technique are the two options for the subcycle update of the magnetic fields. Interpolation has been used for the update of both fields and particles. Second-order accuracy have been obtained in the discretization.

2.2 Curvilinear Coordinates

This section describes the use of the curvilinear coordinates. The corresponding Cartesian positions of the curvilinear grid points can be calculated through a table of geometrical coefficients. Figure 2.1 shows a curvilinear coordinate cell, of which the center is at the grid point i, j, k, while the coner point is at $i+\frac{1}{2}$, $j+\frac{1}{2}$, $k+\frac{1}{2}$ and $i+\frac{1}{2}$, $j+\frac{1}{2}$, $k-\frac{1}{2}$, etc. Correspondingly, a dual cell is defined as a cell with centers at the half grid points and corners at the whole grid points, i, j, k. The magnetic field components are shown as vectors on cell faces with the components pointing normal to the faces while the electric field resides on the cell edges. The magnetic field components can be presented by taking the scaler product of $\mathbf{B}$ with the unit vector normal to the cell surfaces. In another word, the magnetic field can be presented in contraviant components.

$$\mathbf{B} = \mathbf{l_1}\hat{\mathbf{B}}^{\mathbf{1}} + \mathbf{l_2}\hat{\mathbf{B}}^{\mathbf{2}} + \mathbf{l_3}\hat{\mathbf{B}}^{\mathbf{3}}, \tag{2.8}$$

where $\mathbf{l_1}$, $\mathbf{l_2}$,and $\mathbf{l_3}$ are tangent vectors, while $\hat{B}^1$, $\hat{B}^2$, and $\hat{B}^3$ are contravarient tensor components. Note that a set of reciprocal basis vectors ω's can also be defined so that the magnetic field can be expressed as

$$\mathbf{B} = \omega^{\mathbf{1}}\hat{\mathbf{B}}_{\mathbf{1}} + \omega^{\mathbf{2}}\hat{\mathbf{B}}_{\mathbf{2}} + \omega^{\mathbf{3}}\hat{\mathbf{B}}_{\mathbf{3}}, \tag{2.9}$$

where $\omega^{\mathbf{i}} \cdot \mathbf{l_j} = \delta^{\mathbf{i}}_{\mathbf{j}}$. Applying this to the right-facing face of the parallelepiped cell, which is centered at $(i + \frac{1}{2}, j, k)$, the discretization of Farady's law gives

$$\begin{aligned}[\frac{(\hat{B}^1)^{n+1} - (\hat{B}^1)^n}{\Delta t} \cdot \frac{\mathbf{l_1}}{l_1} \cdot \mathbf{A^1}]_{\mathbf{i+\frac{1}{2},j,k}} =& (\hat{\mathbf{E}}^{\mathbf{n+\frac{1}{2}}} \cdot \mathbf{l_3})_{\mathbf{i+\frac{1}{2},j-\frac{1}{2},k}} - (\hat{\mathbf{E}}^{\mathbf{n+\frac{1}{2}}} \cdot \mathbf{l_3})_{\mathbf{i+\frac{1}{2},j+\frac{1}{2},k}} \\ &+ (\hat{\mathbf{E}}^{\mathbf{n+\frac{1}{2}}} \cdot \mathbf{l_2})_{\mathbf{i+\frac{1}{2},j,k+\frac{1}{2}}} - (\hat{\mathbf{E}}^{\mathbf{n+\frac{1}{2}}} \cdot \mathbf{l_2})_{\mathbf{i+\frac{1}{2},j,k-\frac{1}{2}}},\end{aligned} \tag{2.10}$$

where $l_{2,3}$ are lengths of the cell edges and reside at the center of the edges. $\mathbf{A^1} = \mathbf{l_2} \times \mathbf{l_3}$ is the area of the correspoing cell surface and l_1 is the correspoding dual cell tangent vector.

The length of tangent vectors (l's) are the difference between coordinates points specified in the coefficient table as mentioned previously. I.e.,

$$(\mathbf{l_2})_{\mathbf{i+\frac{1}{2},j,k+\frac{1}{2}}} = (\mathbf{r})_{\mathbf{i+\frac{1}{2},j+\frac{1}{2},k+\frac{1}{2}}} - (\mathbf{r})_{\mathbf{i+\frac{1}{2},j-\frac{1}{2},k+\frac{1}{2}}}, \tag{2.11}$$

where the $\mathbf{r}$'s are the position of the coordinate points.

The particle position is updated from

$$(q^i)^{n+1} = (q^i)^n + \Delta t \mathbf{M^i} \cdot \mathbf{v}^{\mathbf{n+\frac{1}{2}}}, \tag{2.12}$$

where the vector tensor $\mathbf{M^i}$ convert $\mathbf{v}$ into particle position q^i in a contravariant form. Note that the positions of particles are also position dependent and so they are interpolated from the grid to the particle position using PIC weighting.

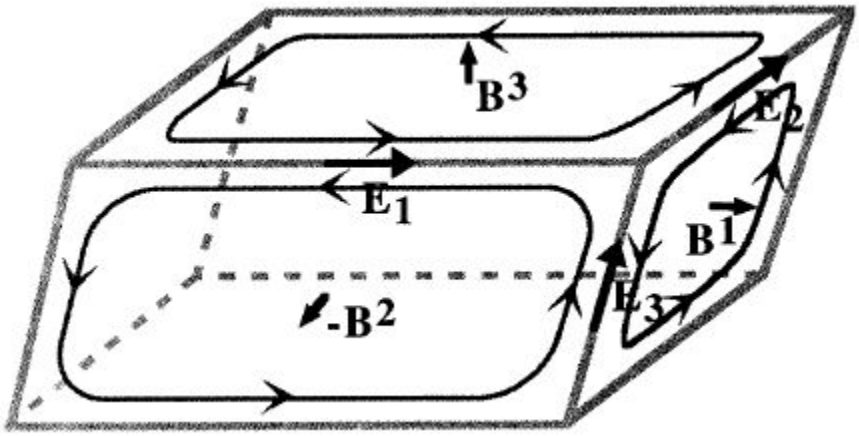

Figure 2.1: A coordinates cell showing the position and orientation of curvilinear components of the magnetic and electric fields. Adatped from [*Swift*, 1996]

2.3 Simulation Domain

The simulation domain contains the system of the bow shock, magnetosheath, and magnetosphere in the dayside region with $x > 0$ as shown in Figure 2.2 and a geocentric distance $4 \leq r \leq 24.5$. The Earth is located at the origin $(x, y, z) = (0, 0, 0)$. Outflow boundary conditions are utilized at $x = 0$, while inflow boundary conditions of the solar wind are applied at $r = 24.5$. The inner boundary at $r = 4$ is perfectly conducting.

Spherical coordinates are used in the simulation. The polar angle θ is measured from the positive z axis, and the azimuthal (longitudinal) angle ϕ from the negative y axis.

2.4 Initial and Boundary Conditions

Initially, a geomagnetic dipole field plus a mirror dipole is assumed in $r < 10R_E$ [*Lin and Wang*, 2005], and a uniform solar wind with the IMF B_0 of $B_{x0} = 0$, $B_{y0} = 0$ and $B_{z0} = -1$ is imposed for $r > 10R_E$. The mirror dipole in the initial setup is to speed up the formation of the bow shock and magnetopause. The bow shock, magnetosphere and magnetosheath are formed by interaction between the solar wind and the dipole field.

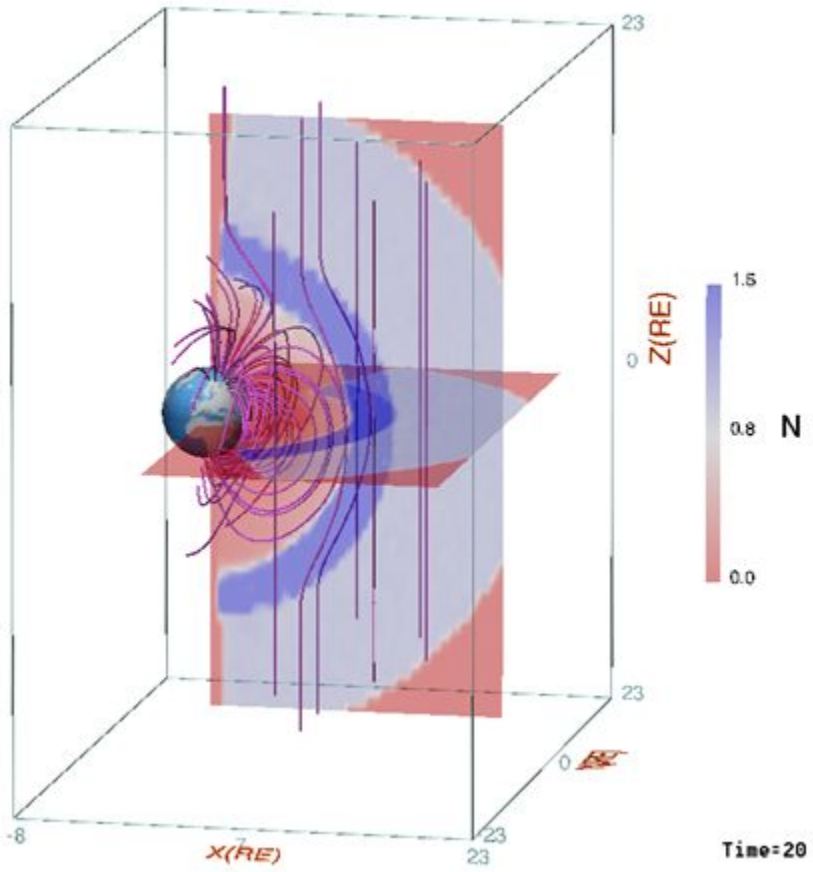

Figure 2.2: Simulation domain in the GSM system

We choose a uniform solar wind with $\beta_i = \beta_e = 0.5$ and an Alfvén Mach number $M_A = 5$. The solar wind flows into the system along the $-x$ direction with an isotropic drifting-Maxwellian distribution. The ion number density in the solar wind is set to be $N_0 = 11,000 R_E^{-3}$ for macro particles in this kinetic simulation, and a total of $\sim 4 \times 10^8$ particles are used in a run. For a typical ion gyrofrequency of 0.1 s^{-1}, the corresponding IMF is $\simeq 10$ nT.

Non-uniform grid spacing Δr is used to produce a higher resolution near the magnetopause, where $\Delta r \simeq 0.09 R_E$. A total grid of 160×104×130 is used. The time step to advance the positions of ions is $0.05\Omega_0^{-1}$, where Ω_0^{-1} is the inverse of the solar wind ion gyrofrequency (Ω_0^{-1}).

In the presentation below, the magnetic field B is scaled by the IMF B_0; the ion number density N by the solar wind density N_0; the time t by the inverse of the solar wind ion gyrofrequency (Ω_0^{-1}); the flow velocity V by the solar wind Alfvén speed V_{A0}; the temperature by V_{A0}^2; the length in units of the Earth's radius R_E.

In order to accommodate to the available computing resources, a larger-than-reality ion inertial length $\lambda_0 = 0.1 R_E$ of the solar wind is chosen in the simulation. Note that $V_{A0} = \lambda_0 \Omega_0$. In an effort to examine the effects of various values of λ_0, we have also run a case with $\lambda_0 = 0.05 R_E$, although still about 3 times larger than that in reality. The resulting structures of the magnetopause reconnection are qualitatively the same as that shown in this thesis.

Three cases are presented in this thesis. In case 1, the dipole axis is tilted sunward by 15°, so that the northern cusp region is well within the simulation domain. Case 2 is similar to case 1, except that the dipole tilt angle is equal to zero. Case 3 is also similar to case 1, except that the IMF is $B_{x0} = 0$, $B_{y0} = -0.707$ and $B_{z0} = -0.707$.

Chapter 3

Data Visualization

The raw data generated from supercomputers are processed and visualized, using desktop computers. As a joint effort with Dr. Wang Xueyi, the visualization tool of 3-D data is developed in MATLAB, which is a numerical computing environment and fourth-generation programming language. Note that a certain fraction of open source code mainly from the website of Mathworks is also included in the package. Figure 3.1 shows the main graphic user interface of the visualization package.

As seen in Figure 3.1, the data processing consists of two parts. The first part is data conversion and data reading, as shown in the upper part of the main interface. There are several options for data format, including 'BOX-DATA', 'RAW-DATA' and 'COV-DATA'. 'RAW-DATA' is the ASCII (American Standard Code for Information Interchange) output from Fortran 90 program, which is in spherical coordinates. The icon 'RAW-DATA CONVERSION' provides a function to convert the raw data to a HDF (Hierarchical Data Format) format, namely, the format of 'COV-DATA' as shown in the interface. Note that the 'COV-DATA' is in the Cartesian coordinate system.

The lower part of the main interface are the main menu for plotting. Most of our data are 3-D. After reading data, clicking icon '3D PLOT' leads to the 3-D data plotting menu. Figure 3.2 showcases an example of 3-D data visualization. The contours are the total magnetic field in the noon meridian and equatorial planes, supposed with the isosurface of $B = 4.5$ in the simulation units.

Figure 3.3 shows the capability of slice plotting integrated in the the 3-D data visualization package. Not only planes of a constant x, y or z in the GSM system but also planes with a rotation around the three principle axes can be chosen to plot contours.

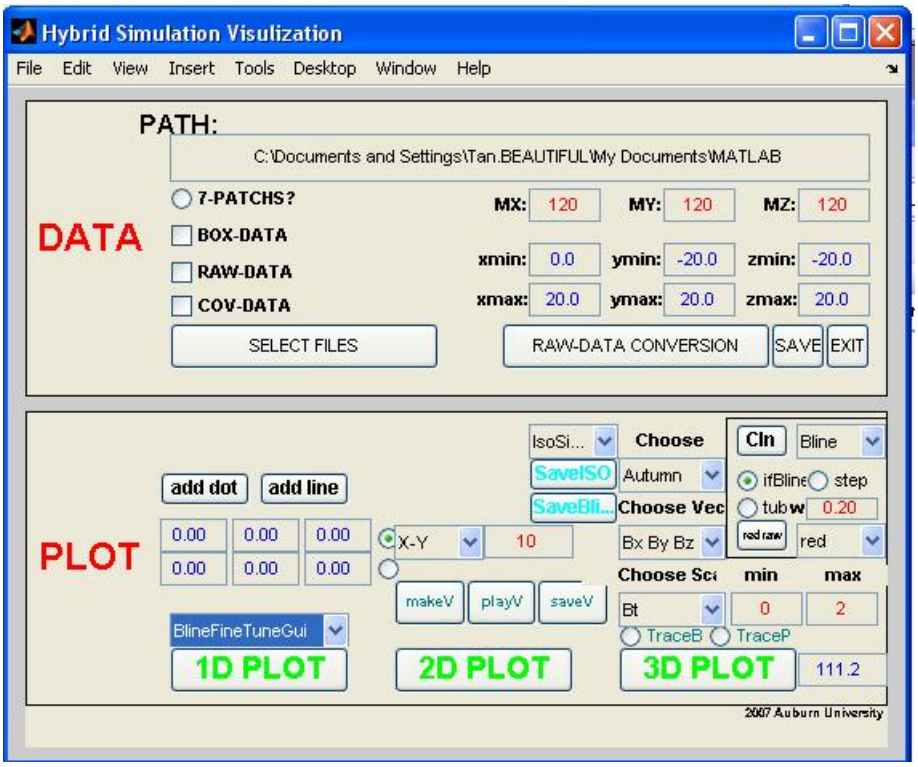

Figure 3.1: Graphic user interface of the visualization package

Figure 3.3 shows the capability of isosurface plotting integrated in the the 3-D data visualization package. Lighting and transparency can be adjusted as needed.

Both scaler data sets such ion density, temperature and vector data sets such as velocity and magnetic field can be visualized in the 3-D frame. For magnetic field, field lines can be plotted interactively. In the field line plotting mode, clicking a point inside a plotted slice within the 3-D visualization frame will enable the package to plot a field line through that point. Figure 3.5 is the graphic user interface of fine tuning magnetic field lines. Clicking the icon 'x-' changes the position of the point through which the visualization package plots the magnetic field line by a small step, e.g., 0.1, in the negative x direction.

In addition to the general 3-D plotting capability, new graphic objects such as particle trajectories can be plotted within the same 3-D figure. The package also has relatively independent functions for one dimensional (1-D) plotting and 2-D (two dimensional) plotting as indicated in the main interface.

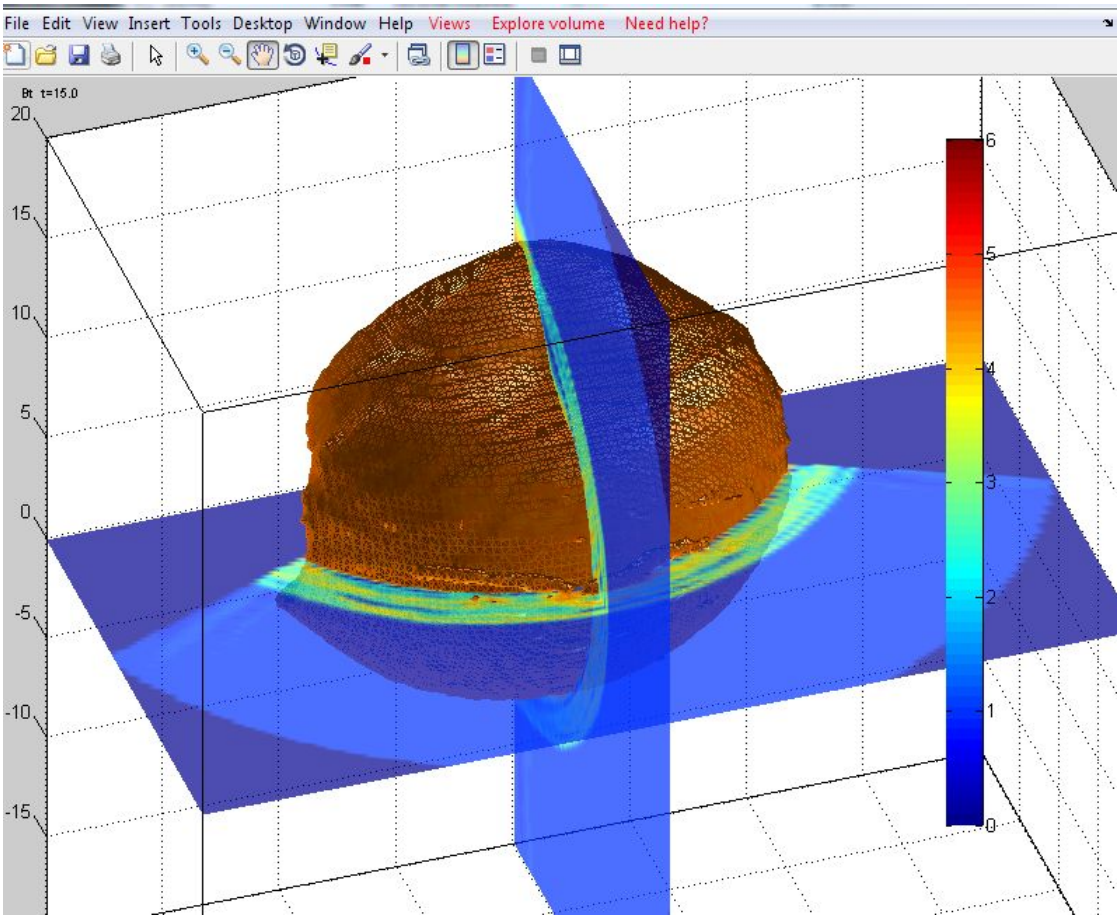

Figure 3.2: An example of 3-D data visualization: The contours are the total magnetic field in the noon meridian and equatorial planes, supposed with the isosurface of $B = 4.5$ in the simulation units.

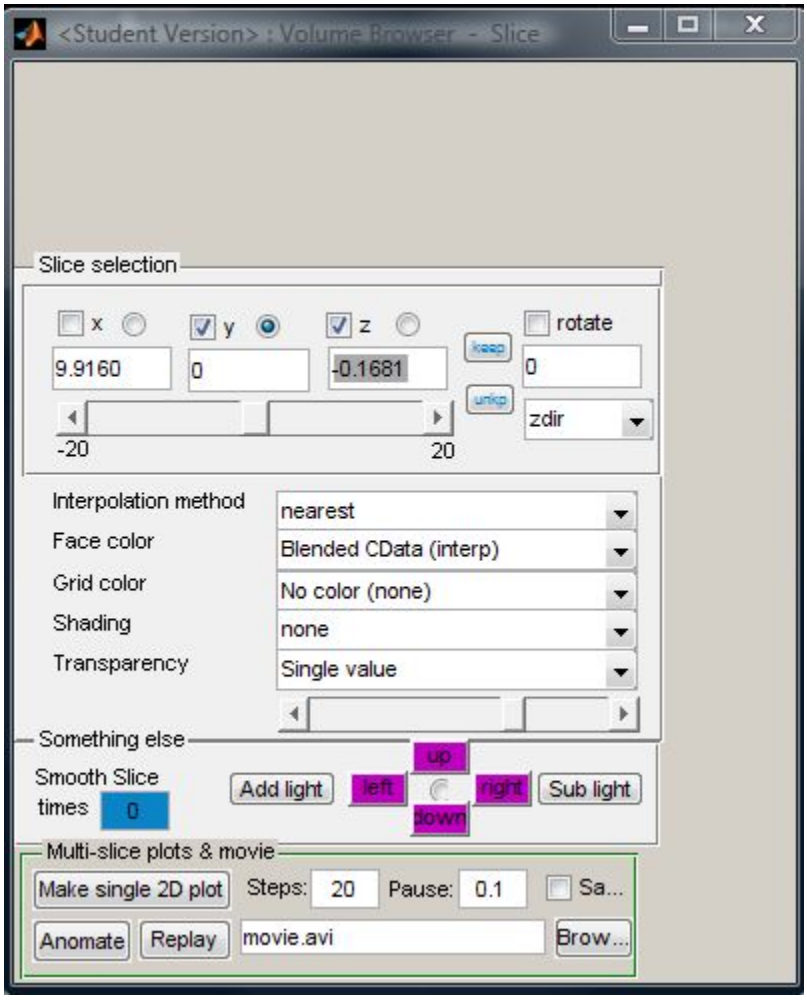

Figure 3.3: Slice plotting integrated the 3-D data visualization package.

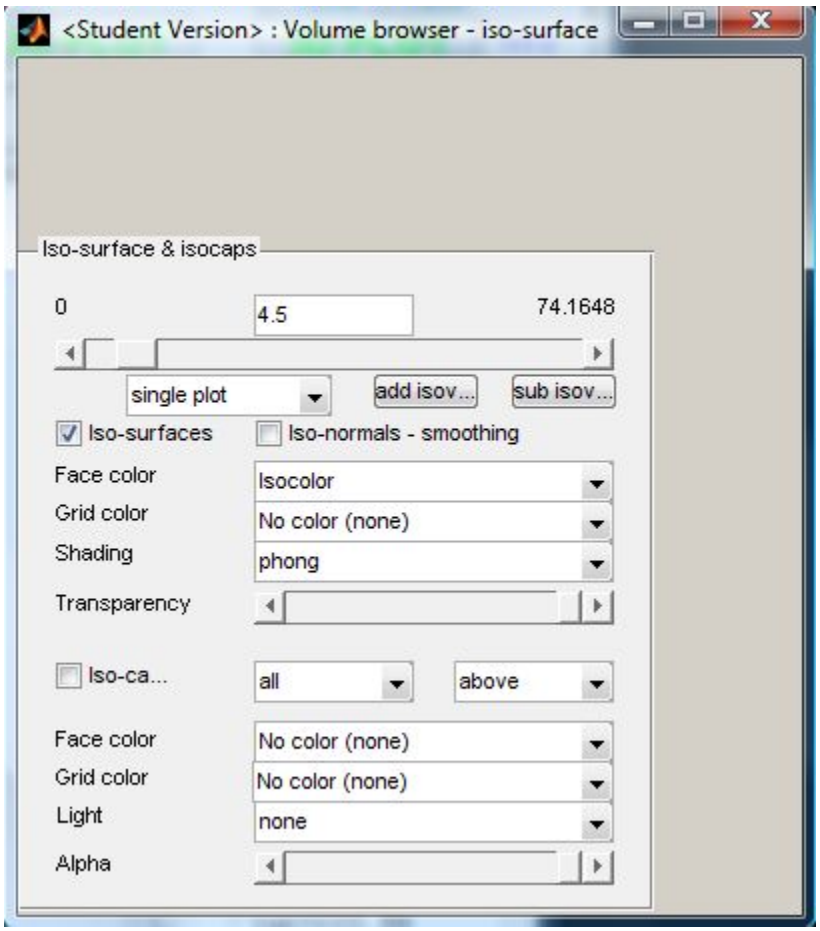

Figure 3.4: Isosurface plotting integrated the 3-D data visualization package.

Figure 3.5: Graphic user interface of fine tuning magnetic field lines.

The sample source code in the appendix is the function in MATLAB for contours plotting and fine tuning field lines, which contain frequently used technique in the package.

Chapter 4

Dayside Magnetic Reconnection Under a Purely Southward IMF: Structure and Evolution of Reconnection

4.1 Introduction

As we discussed in Chapter 1, magnetic reconnection is believed to play an important role in geomagnetic and magnetospheric plasma processes. Without magnetic reconnection, the magnetosphere of the Earth is a relatively 'isolated' space from the solar wind. With the magnetospheric field lines opened up by the reconnection process, solar wind plasma is able to penetrate through the magnetopause; momentum and energy can also be transferred from the solar wind and interplanetary magnetic field (IMF) into the magnetosphere as the connectivity of the magnetic field lines changes.

One of the important questions about magnetic reconnection is the magnetic configuration of connectivity associated with it, i.e., whether the reconnection occurs through a single X line or multiple X lines [*Winglee et al.*, 2008]. According to the time scales of the in-situ observation results, magnetic reconnection events fall into two categories: (1) quasi-stationary magnetic reconnection; (2) transient magnetic reconnection. A quasi-stationary magnetic reconnection might have a time scale of hours [*Gosling et al.*, 1982], which is dominated by a single X-line. The transient counterpart usually has a quasi-period around 8 minutes [*Rijnbeek et al.*, 1984]. Flux transfer events (FTEs), which are widely considered to be associated with transient magnetic reconnection nearby[e.g., *Hasegawa et al.*, 2006; *Kuznetsova et al.*, 2009], were first discovered by *Russell and Elphic* [1978]. Initially, FTEs were thought to be flux tubes that are the products of single-X-line, patchy reconnection [*Russell and Elphic*, 1978]. Due to complicated geometries and the multi-scale nature of reconnection, numerical simulations have been utilized to investigate the reconnection physics.

Lee and Fu [1985] suggested that FTEs are multiple-X-line flux ropes with helical internal structures, in which a magnetic field line is reconnected at two or more reconnection sites. Alternative models were also proposed to account for the formation of FTEs. For example, *Scholer* [1988] suggested that the variation of reconnection rate could give rise to a loop-like field lines based on the single X-line reconnection.

Since local simulation models have strong dependence on the boundary conditions, three-dimensional (3-D) global simulations using modern computers have become a powerful tool to study the reconnection and the associated structure of the dayside magnetopause. The latest work includes global magnetohydrodynamic (MHD) simulations by *Fedder et al.* [2002], *Raeder* [2006], *Dorelli and Bhattacharjee* [2009], *Kuznetsova et al.* [2009] and *Winglee et al.* [2008]. *Dorelli and Bhattacharjee* [2009] point out that it is likely that the resistive MHD Ohm's law may fail to capture much of the physics relevant to the FTE generation when the model assumption is no longer valid under certain circumstances.

The challenge to the understanding of FTEs in the magnetopause reconnection is that they are of 3-D nature, embedded in a multi-scale solar wind-magnetosphere global system, in which the ion physics is a very important. Inclusion of plasma kinetic physics is necessary for the modeling of the generation and evolution of magnetopause reconnection as well as the understanding of their internal structure. For the first time, here we present a numerical simulation of dayside reconnection using a 3-D global scale hybrid model, in which fully-kinetic ion physics is solved in a self-consistent electromagnetic field [*Lin and Wang*, 2005]. The reconnection events are identified by the connectivity change of magnetic field lines and supported by the presence of reconnection jets away from the reconnection sites. Both multiple X-line and single X-line type structures are examined, where the term 'X lines' is defined in the context of local 3-D field configuration [e.g., *Priest and Forbes*, 2000;]. The detailed definition will be given in section 3.2. Note that our definition of X line is different from the one used by *Dorelli and Bhattacharjee* [2009], which defines the X line as a separator line, the intersection of two north pole, and closed field lines. Based on a

global MHD simulation, *Dorelli and Bhattacharjee* [2009] have found that the instability associated with FTEs is triggered by a movement of the flow stagnation point away from the magnetic separator, which modifies the subsolar stagnation point flow.

In this chapter, two cases with a purely southward IMF are investigated. In the presence of a strong southward IMF, the Earth's dipole field is anti-parallel to the IMF around the equatorial plane, leading to the occurrence of magnetic reconnection at the low latitude magnetopause. Statistical studies show that majority of FTEs are observed during a southward IMF [*Rijnbeek et al.*, 1984; *Sibeck and Lin*, 2010].

4.2 Simulation Results

4.2.1 Magnetic Field Line Configuration under Southward IMF

We first present results from case 1, with a 15° dipole tilt angle and a purely southward IMF. As the solar wind ions convect earthward carrying the IMF, the bow shock, magnetosheath, and magnetopause form gradually in a self-consistent manner. Most magnetic reconnection events originate in the equatorial region, which are related to X-lines of nearly anti-parallel magnetic field reconnection. Flux ropes are generated above and below the equator and reconnected magnetic field lines are approximately symmetric about the noon meridian plane.

Figure 4.1 shows the magnetic field line configuration obtained from case 1 in a global view, emphasizing field lines in the northern hemisphere at $t = 5$, 15, 25 and 35. The blue sphere at the origin represents the Earth. The contours in the equatorial plane show the ion density. Outward from the Earth, the boundary region with a sharp ion density increase is the magnetopause, at a standoff distance of $r \simeq 9.5 \sim 10$. The bow shock is the boundary region with a sharp density decrease. The black lines are the closed field lines of the geomagnetic dipole field. The yellow lines are open field lines of the shocked IMF before magnetic reconnection. Field lines in other colors are reconnected field lines with one end

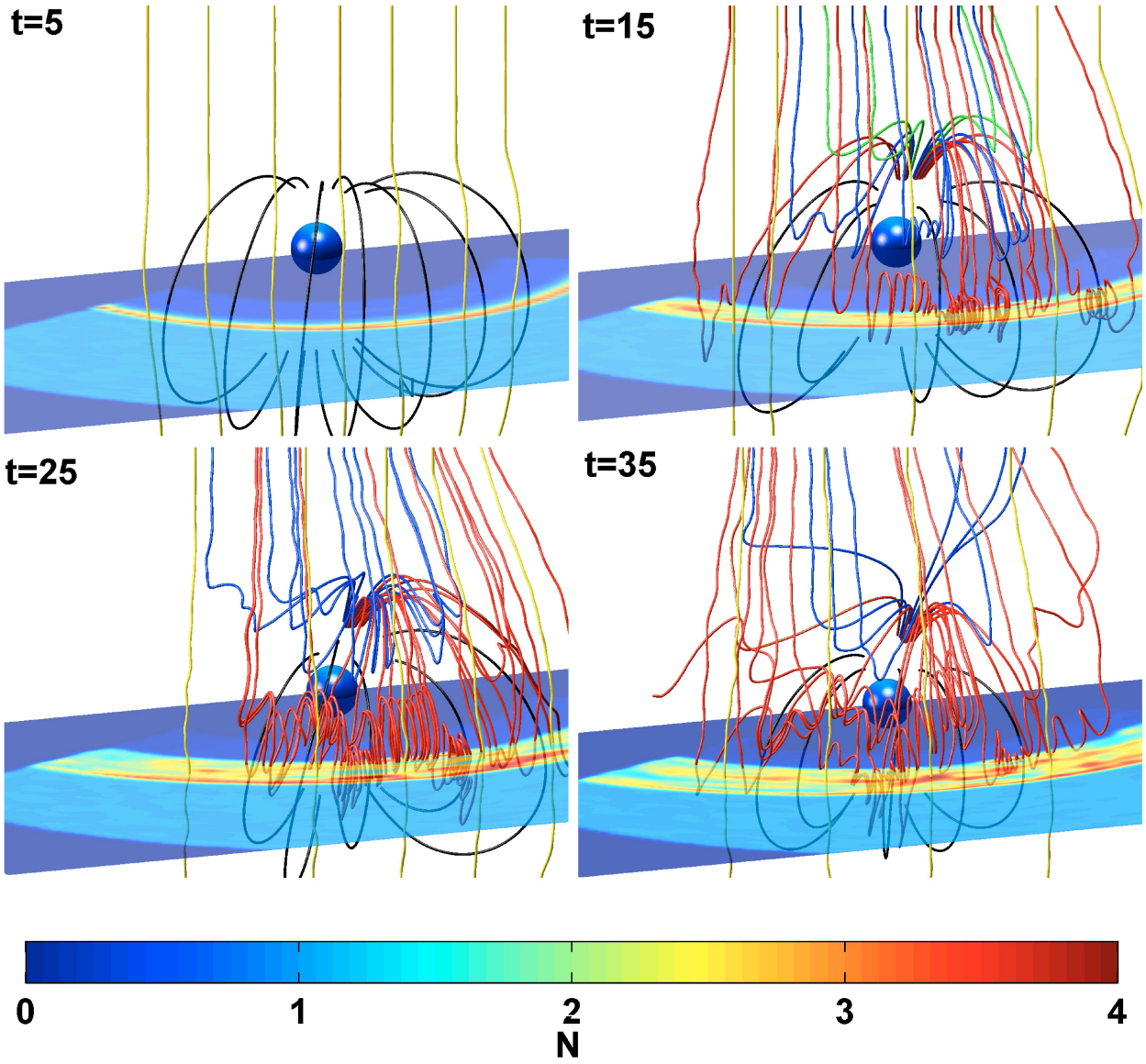

Figure 4.1: Magnetic field line configuration in a global view obtained in case 1 at $t = 5$ (top left), $t = 15$ (top right), $t = 25$ (bottom left), and $t = 35$ (bottom right), respectively. The closed dipole field lines are in black. Yellow lines are open field lines before magnetic reconnection. Field lines in other colors are reconnected field lines between the IMF and dipole field in different regions. Contours in the equatorial plane show the ion density.

connecting to IMF and the other end to the magnetosphere, where the colors are used to distinguish different regions of magnetic reconnection as in the description below.

The upper left plot of Figure 4.1 shows the magnetic configuration of the initial phase at $t = 5$, or $t \simeq 25\Omega^{-1}$ with Ω^{-1} being the local ion gyrofrequency. There appears to be no significant evidence of magnetic reconnection at this time.

At $t = 15$ (Figure 4.1, upper right), looped flux ropes (FTEs), form in between two neighboring X lines, while the X lines of finite length lie in the dawn-dusk direction. The axial extent of the flux ropes is limited as seen in the plot. Around the equator, there are both looped flux ropes and adjacent single X-line magnetic reconnection shown by the red field lines. FTEs are found to be localized looped flux ropes corresponding to multiple X-line reconnection (MXR) [*Raeder*, 2006; *Hasegawa et al.*, 2006] with helical internal structures, which generate signatures consistent with in situ observations. The bipolar FTE signature of B_n, the local normal component of magnetic field, will be discussed below. A Walén test will also be performed for the single X-line reconnection to investigate the presence of relevant MHD discontinuities, using the data from case 2.

The blue field lines in the mid latitudes show another layer of looped flux ropes (FTEs), while the green field lines in the northern high latitudes show the occurrence of a single X-line-type reconnection with no obvious looped field lines.

At $t = 25$ (Figure 4.1, lower left), or $t \simeq 125\Omega^{-1}$, the looped flux ropes illustrated by the red field lines of $t = 15$ have moved poleward with a noticeable expansion of their azimuthal size. The blue FTEs at $t = 15$ have also propagated towards the cusp and tailward, and meanwhile toward dawn/dusk side.

At $t = 35$ (Figure 4.1, lower right), part of the red flux ropes around the equator at $t = 15$ have moved to the middle latitudes, so have segments of X lines adjacent to the FTEs. The blue FTEs in the middle latitudes at $t = 15$ also continue moving tailward and poleward, and part of them have disintegrated during the interaction with the cusp while the rest have convected past the pole.

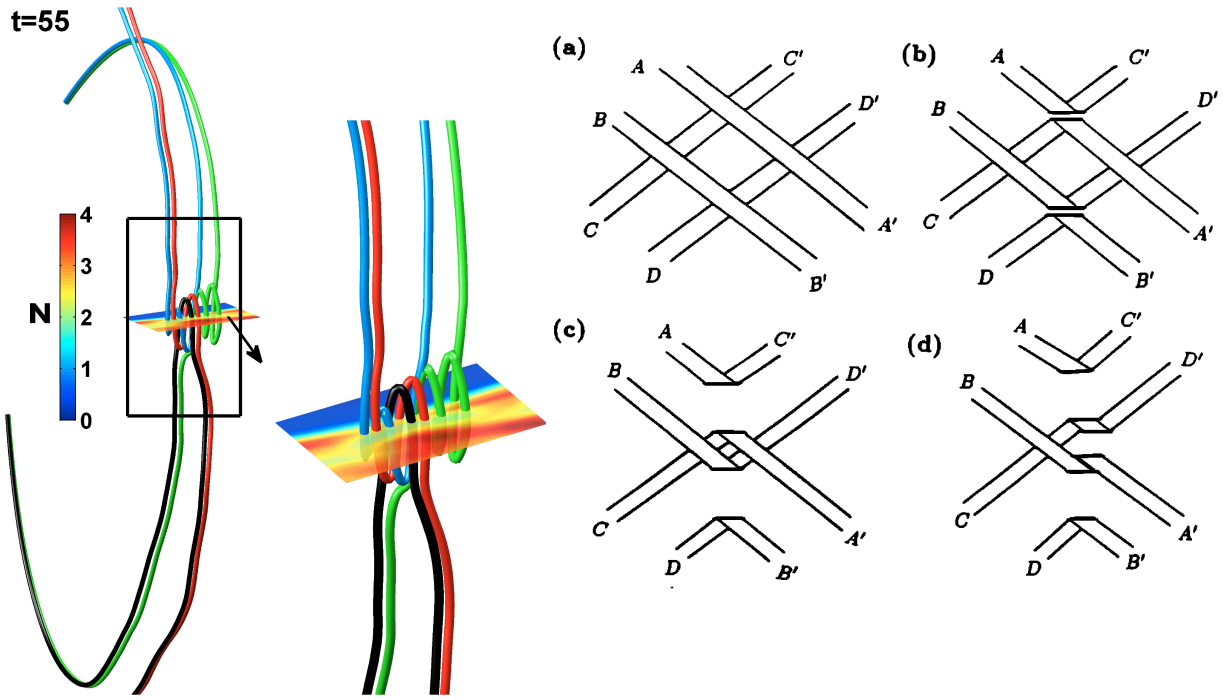

Figure 4.2: (Left) Four field lines of different topologies in case 1 at $t = 55$. (Right) Illustration of how the patchy reconnection and multiple reconnection can explain the coexistence of the four field lines in the left plot [*Lee et al.*, 1993].

In our simulation, the magnetopause reconnection is found to generate not only the reconnected field lines connecting the IMF to the dipole field, but also other topologies due to 3-D effects, including both purely closed reconnected field lines as well as purely open reconnected field lines. The color plots in Figure 4.2 show four field lines of case 1 at $t = 55$, in which the flux ropes are mainly located at $x \simeq 9.5$-10, $y \simeq -0.6$--1.8 and $z \simeq -0.5$-1. In addition to the blue and black field lines that are between the magnetosphere and the magnetosheath, there also exist the green closed field lines that are connected from the magnetospheric field to the magnetospheric field, threading from the northern cusp to the southern cusp, as well as the red open field line from the magnetosheath to the magnetosheath. The rectangular contour slice shows ion density at $z = 0.5$ around the reconnection site. Note that the sliver of green density on the slice is adjacent and on the sunward side of the flux ropes.

The green and red field lines in Figure 4.2 are associated with the FTE flux ropes, and thus are different from the unperturbed closed geomagnetic field lines and open solar wind field lines. A previous 3-D MHD simulation of *Lee et al.* [1993] shows that due to the non-uniformity along the plane of the current sheet, four possible topologies of FTE field lines can be generated. They are the field lines connected (1) from IMF to the Earth's dipole field (field lines between solar wind and north pole); (2) from the Earth's dipole field to the Earth's dipole field; (3) from the Earth's dipole field to IMF (field lines between solar wind and south pole); and (4) from IMF to IMF. The right plots (a)-(d) in Figure 4.2 (Right) [*Lee et al.*, 1993] can be used to illustrate how the patchy, multiple reconnection events can explain the coexistence of the four types of field lines obtained from our 3-D simulation as shown in the color plots of Figure 4.2. The patchy reconnection indicates that the size of the reconnection region has a fairly limited extent in space [*Kan*, 1988; *Pinnock et al.*, 1995]. At the initial stage (a), flux tubes AA$'$ and BB$'$ are two bundles of magnetosheath fields and CC $'$ and DD$'$ are of magnetospheric fields. At the second stage (b), reconnection takes place at two patches. At the third stage (c), the reconnected flux tubes BD$'$ and CA$'$ move

toward each other so that at the fourth stage (d) a re-reconnection has occurred, leading to the formation of closed flux tube CD′. Flux tubes CD′ and BA′ correspond to the green (closed) and red (open) field lines in the color plots of Figure 4.2. Since flux ropes form between multiple X lines, a position shift of neighboring X lines relevant to flux ropes can also play a critical role in determining the connectivity of field line [*Lee et al.*, 1993].

The existence of reconnected field lines from the magnetosphere to the magnetosphere or from IMF to the IMF, in addition to the opened magnetospheric field lines and the unperturbed magnetosheath field lines, has also been suggested by *Lui et al.* [2008] and *Kuznetsova et al.* [2009]. We note that our study is the first global simulation that shows these four types of field lines. The reason why a 3-D global hybrid simulation 'shows' but a 3-D global MHD simulation does not deserves further investigation. In our simulation, localized flux ropes at low latitudes with dominant purely closed field lines do not occur often and can not survive more than $20\Omega_0^{-1}$. Further investigation is needed to address how long their life time is for more general cases with a finite IMF B_y component.

4.2.2 Structure and Evolution of Flux Transfer Events (FTEs)

The structure and evolution of FTEs are illustrated in Figure 4.3 around the dayside magnetopause. Here, we give our definition of the reconnection X line before the discussion on physical quantities associated with 3-D reconnection. We adopt a procedure like the one described by *Priest and Forbes* [2000b], which defines reconnection in a general way.

We seek a set of singular lines, near which the magnetic field has an X-type configuration. The first row of Figure 4.3 illustrates how a singular line, or in another word, "X line" is defined, which is the intersection of two surfaces that separate distinct field lines of four different local regions (earthward side of the magnetopause current sheet, sunward side of the current sheet, from the sunward side to the earthward side, and from the earthward side to the sunward side following the magnetic field direction). The black tubes are field lines traced in the 3-D space. The X-type configuration is determined by mapping the 3-D field

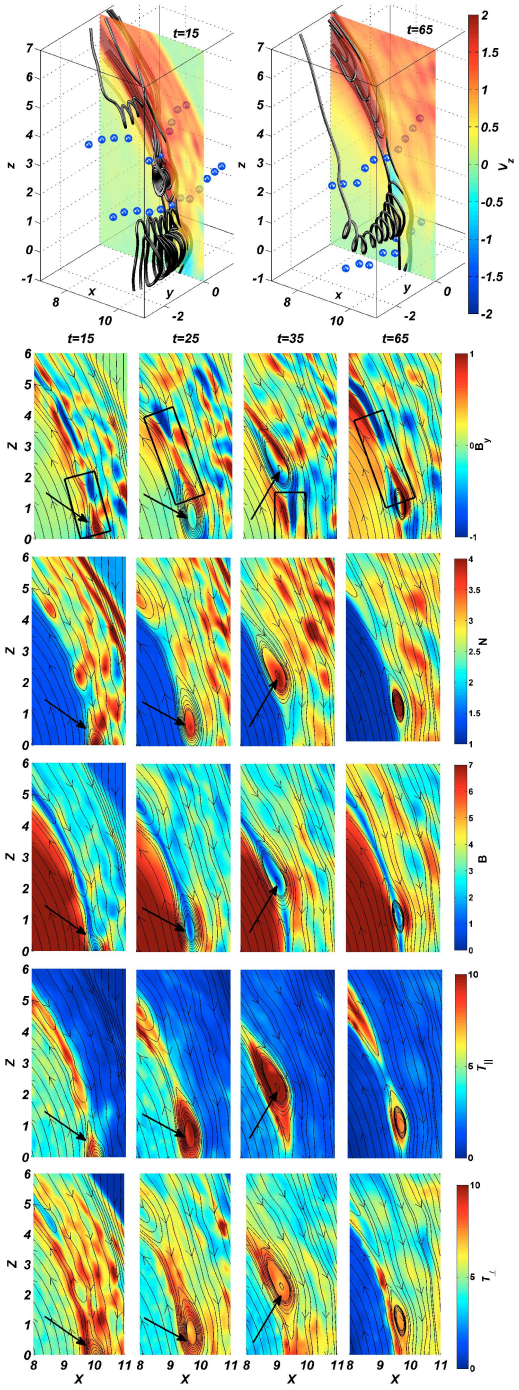

Figure 4.3: Three dimensional plots (first row) illustrate how X line is defined, with V_z contours in the noon meridian plane. Two dimensional intensity plots of B_y (second row), ion density (third row), total magnetic field (fourth row), parallel temperature (fifth row) and perpendicular temperature (bottom row) are also in the noon-midnight meridional plane, zoomed around the dayside magnetopause at t = 15, 25, 35, 65, respectively (from left to right).

lines into an x-z reference plane. An X point of the X line that separates local areas of four different magnetic connectivity types is found, shown as a blue dot. By connecting the X points in a series of such planes, an X line segment naturally forms. Other supporting evidence of the X line, such as the existence of opposite flow jets and the quadrupole magnetic field structure in the guide field, is given below. The FTEs to be discussed in this chapter are of an O-line that requires two X-lines.

As shown in the left plot of the first row, there are two X-line segments as in blue dots at $t = 15$. There are also two X lines at $t = 65$. But the previous two at $t = 15$ are not seen at $t = 65$ as they have moved northward. The northern X line segment at $t = 65$ was below the plane of $z = -1$ at $t = 15$ before it moves to its present location in this case with a tilted dipole axis.

In order to illustrate the presence of reconnection jets from the X lines, the contours in the first row of Figure 4.3 show V_z, the z component of ion bulk flow velocity in the noon-midnight meridional plane obtained from case 1. Our definition of the 3-D magnetic reconnection is consistent with observations that plasma jets are moving away from X lines due to reconnection. At $t = 65$, two opposite jets with V_z of opposite sign occur inside the FTE flux ropes between the two X lines. The V_z of magnetosheath plasmas near FTEs increases as the latitude increases. Although two opposite jets are expected from an X line, the southward jet at $t = 15$ appears missing, due to the the non-zero northward background V_z of the ambient magnetosheath plasmas. Meanwhile, strengths of the two opposite jets from two adjacent X lines inside one FTE are not necessarily equal to each other. As in the case at $t = 15$ shown in the top left plot of Figure 4.3, one direction of ion acceleration is dominant inside the FTE between the two X lines.

The intensity plots in Figure 4.3 show B_y (second row), ion density N (third row), magnetic field strength B (fourth row), parallel ion temperature $T_\parallel$ (fifth row), and perpendicular ion temperature $T_\perp$ (bottom row) in the noon-midnight meridional plane at $t = 15, 25, 35$ and 65. The black lines superposed on the contours are two dimensional (2-D) field lines

projected onto the noon meridian plane. Note that the density of 2-D field lines shown here does not represent the magnetic field strength. The locations of FTEs can be identified from the magnetic islands traced by the field lines in the contour plots. The center of a highlighted FTE island is marked with arrows in the plots from t = 15-35.

The FTE marked in Figure 4.3 forms around $t = 15$ at the subsolar region, and moves poleward as time proceeds. The FTE speeds up as it moves away from the equator. At $t = 65$, another FTE forms near the subsolar region, which reflects the quasi-periodic generation of FTEs. Between $t = 35$ and $t = 65$, there is a relative quiescent period, and magnetic reconnection remains single X-line-like in the region.

Perturbations in B_y are obtained in the vicinity of X lines, as indicated by the black rectangles in Figure 4.3. Because the initial B_y in the solar wind is set to be zero, the intensity of B_y in the plot can be viewed as a perturbation. The B_y pattern is consistent with the Hall effects due to the ion kinetic effects [*Sonnerup*, 1979; *Terasawa*, 1983; *Pritchett*, 2001; *Shay et al.*, 2001]. In a simple 2-D reconnection model, plasma flows into the vicinity of an X line. Electrons are frozen-in to the field lines and ions lag behind due to their larger inertia, which produces a net current and a corresponding B_y perturbation. This leads to a negative B_y above and a positive B_y below the X line on the magnetosheath side, with a negative B_y below and a positive B_y above the X line on the magnetospheric side. For the dayside magnetopause, it is expected that the polarity on the magnetosheath side dominates the Hall pattern due to the much larger density on the magnetosheath side, which is different from the quadrupole structure of B_y for a nearly symmetric current sheet [*Karimabadi et al.*, 1999; *Pritchett*, 2001; *Birn et al.*, 2008].

In contrast to a dominant polarity on the magnetosheath side, B_y perturbations with near equal strength are seen in the multiple X-line reconnection at $t = 25$, 35 and 65 in our simulation, as shown in Figure 4.3. The quadrupole B_y perturbations are within a boundary layer, of which the sunward thickness is $\sim 0.5R_E - 1.0R_E$. The plasma density level in the boundary layer adjacent to the magnetosphere is about 1.0, comparable to 2.0, in the

ambient magnetosheath. The local plasma density adjacent to the magnetosphere may be enhanced by the trapped ions around the nearby O line of an FTE. The presence of near quadrupole B_y may be due to the thick boundary layer around the FTEs.

The third row of Figure 4.3 reveals that the FTEs are associated with ion density enhancements at the core. Note that the low density region at $t = 15$, $x = 10$-11 and $z = 5$-6 are in the solar wind. Corresponding to the density enhancement, the magnetic field strength is found to dip in the core of the FTE as seen in the fourth row of Figure 4.3. Such results are consistent with the 2-D hybrid simulation results of *Omidi and Sibeck* [2007] for a similar case of a purely southward IMF, in which the reconnection is mainly of anti-parallel field type. It has been suggested [e.g., *Hasegawa et al.*, 2006; *Scholer et al.*, 2003] that whether an FTE possesses a strong core field may be associated with whether the reconnection is an anti-parallel or component merging.

In the upper panel of Figure 4.4, ion density contours at $x = 9.5$ at $t = 80$ are shown as well as field lines, while a close-up plot around three FTEs at the magnetopause is shown in the lower panel. The flux ropes are seen to wrap around a filament of relatively higher ion density. The peak density is about 2 times that of the ambient plasma inside the boundary layer. Our results indicate that the density at the FTE core may be larger than that near the edge, and that the spatial profile of the density along a path through the core may be very different from that through the edge.

Ion heating is found in the FTEs, as shown in the bottom two rows of Figure 4.3. Stronger enhancement in the parallel ion temperature $T_{\parallel}$ is seen inside FTEs, while the perpendicular temperature $T_{\perp}$ shows a mild increase compared with that in the ambient magnetosheath. The enhancement of $T_{\parallel}/T_{\perp}$ in magnetic reconnection has also been reported in satellite observations[*Klumpar et al.*, 1990] and numerical simulations[*Birn and Hesse*, 2001]. Note that the fading of the ion temperature in the closed field line region between $t = 15$ and $t = 65$ is due to the loss of ion particles in the magnetosphere because the returned

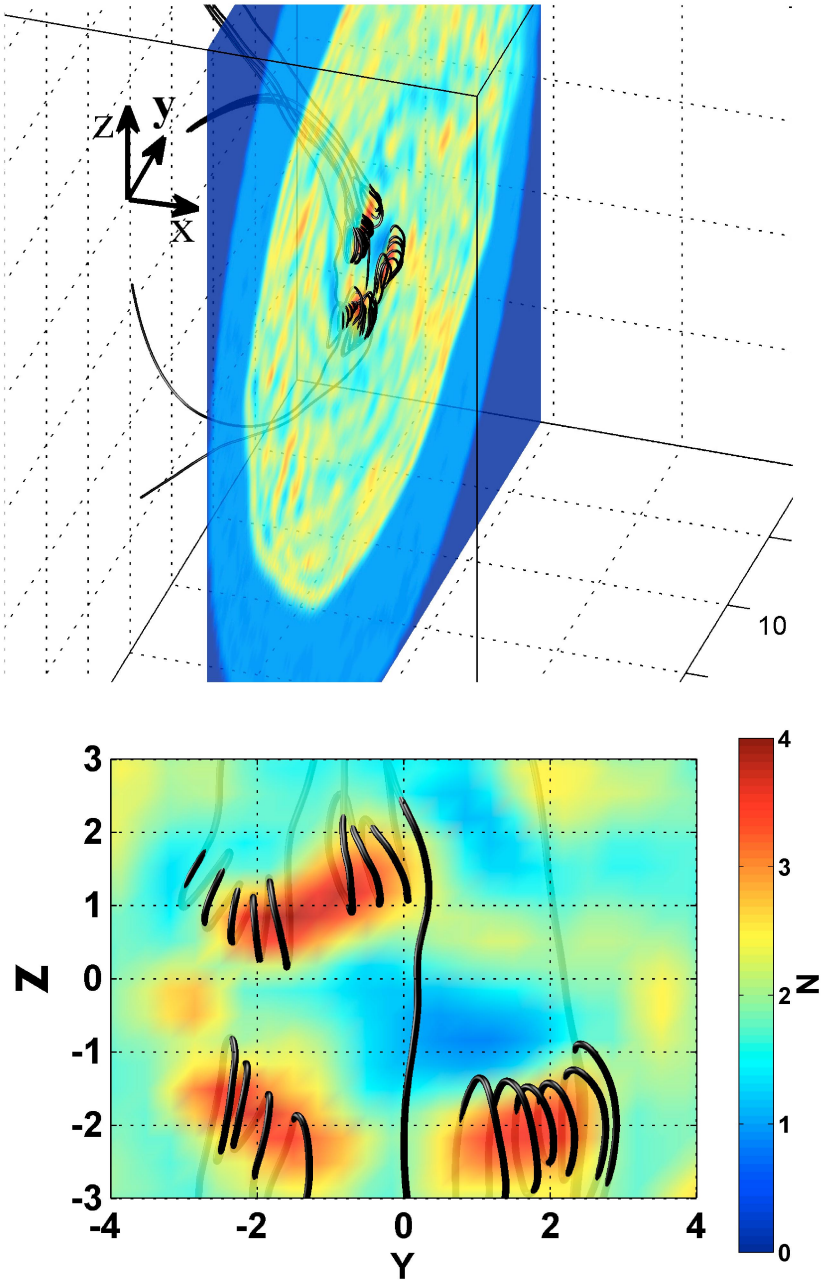

Figure 4.4: Ion density filaments inside FTEs of case 1. The upper panel shows ion density contours at $x = 9.5$ and $t = 80$, superposed onto a field-line plot, and the lower panel is a close-up of the same plane.

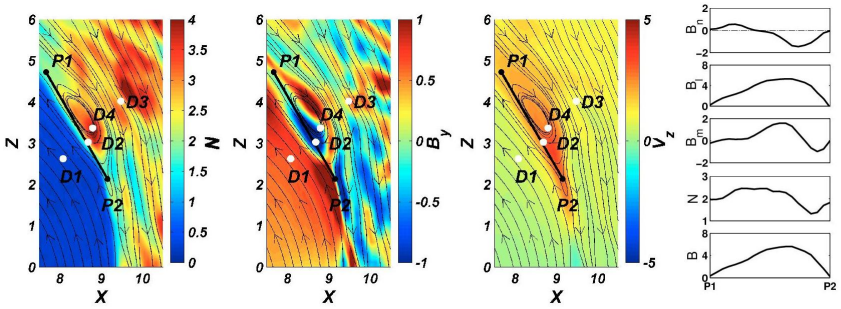

Figure 4.5: Ion density filaments inside FTEs of case 1. The upper panel shows ion density contours at $x = 9.5$ and $t = 80$, superposed onto a field-line plot, and the lower panel is a close-up of the same plane.

ions from the magnetotail are not included in the simulation model. Only the transmitted ions from the magnetosheath are emphasized in the simulated magnetopause reconnection.

4.2.3 Magnetic Field Signature and Ion Velocity Distributions in FTEs

Bipolar signature of the normal component of magnetic field, B_n, has been considered a typical signature of the observed FTEs [e.g., *Russell and Elphic*, 1978; *Dorelli and Bhattacharjee*, 2009]. Viewed in the local normal coordinates, satellites traveling through an FTE along the magnetopause usually observe a transient magnetic field structure in which B_n changes either from + to − or from − to +.

The flux ropes obtained in our simulation indeed produce the bipolar signature similar to satellite observations. The rightmost plot in Figure 4.5 shows the spatial variation of the magnetic field and ion density along a virtual satellite path through the magnetospheric edge of an FTE at $t = 40$ in the simulation of case 1. In the contour plots of Figure 4.5, the path is from point $P1$ to point $P2$ along the magnetopause, illustrated by the thick black line. The contours are of N, B_y and V_z in the noon meridian plane, with 2-D black field lines superposed on.

The top three panels in the rightmost plot of Figure 4.5 show the spatial variations of B_n, B_l, and B_m components of magnetic field, where the local normal direction $\hat{\mathbf{n}}$ of the

lmn local coordinate system is determined by the minimum variance method [*Sonnerup and Cahill*, 1967]. In this coordinate system, three directions $\hat{\mathbf{l}}$, $\hat{\mathbf{m}}$ and $\hat{\mathbf{n}}$ complete a right-handed orthogonal system with $\hat{\mathbf{l}}$ defined as $(\hat{\mathbf{z}} - \hat{\mathbf{n}}(\hat{\mathbf{n}} \cdot \hat{\mathbf{z}}))/|\hat{\mathbf{z}} - \hat{\mathbf{n}}(\hat{\mathbf{n}} \cdot \hat{\mathbf{z}})|$ and $\hat{\mathbf{m}}$ as the vector product $\hat{\mathbf{n}} \times \hat{\mathbf{l}}$.

The local normal direction $\hat{\mathbf{n}}$ is found to be $(0.8259, 0.0139, 0.5636)$ and $\hat{\mathbf{m}}$ is nearly $-\hat{\mathbf{y}}$ in the GSM system. As shown in the top panel, B_n changes from positive near $P1$ to negative as the virtual satellite 'flies' toward $P2$, consistent with the typical bipolar magnetic field signature of FTE. The B_l component remains a positive magnetospheric value during the crossing. The magnitude of B_m is approximately equal to $-B_y$. The two bipolar enhancements of B_m are due to two parts of the adjacent Hall field perturbations from two X-lines as illustrated in the contours of B_y. Near the center of the FTE, the ion density goes up as the virtual satellite cuts through the density filament inside the flux ropes as shown in the contours of N. The bottom panel shows the field strength B, which exhibits a pattern that is not of a simple anti-phase relationship with ion density.

To investigate the properties of ion particles around FTEs, we 'probe' in Figure 4.6 the ion velocity distributions at the specific FTE highlighted with white dots in Figure 4.5. Figure 4.6 plots the parallel velocities (relative to the local magnetic field) $v_{i\parallel}$ of ion particles versus one of the two perpendicular ion velocities, $v_{i\perp 1}$. Here, the perpendicular direction $\hat{\mathbf{e}}_{\perp \mathbf{1}}$ is chosen to be in the direction of $\mathbf{B} \times \hat{\mathbf{y}}$. The top left, top right, bottom left and bottom right plots of Figure 4.6 show the distributions at four chosen locations centered at $D1$, $D2$, $D3$ and $D4$, respectively, which are marked in the contours of Figure 4.5.

The top left of Figure 4.6 corresponds to location $D1$ centered at $(x, y, z) = (8.08, 0, 2.62)$. Among the four locations, $D1$ is the closest to the magnetosphere but still on open field lines. The velocity distribution features a tenuous ion population, and the majority of ions possess near zero bulk velocity. The bottom left plot of Figure 4.6 corresponds to location $D3$ centered at $(x, y, z) = (9.48, 0, 4.02)$ in the magnetosheath outside the FTE. This dense ion population convects northward with the bulk $V_{i\parallel} < 0$, opposite to the southward IMF.

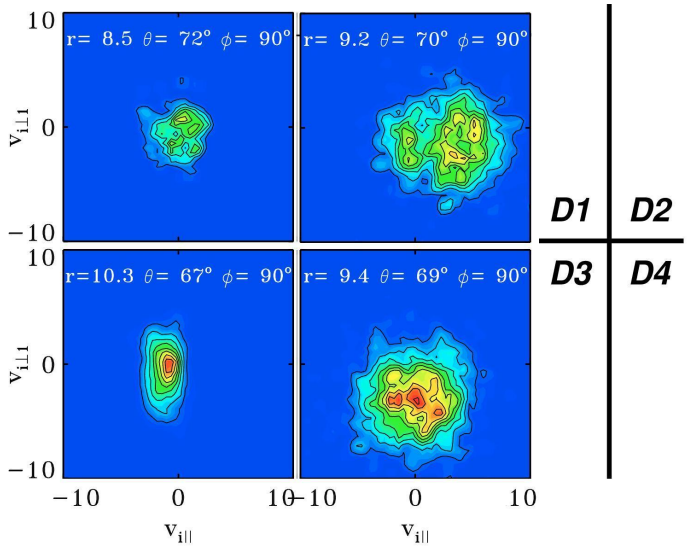

Figure 4.6: Top left, top right, bottom left and bottom right show the ion velocity distributions at four chosen locations centered at $D1$, $D2$, $D3$ and $D4$ in Figure 4.5, respectively.

The top right plot of Figure 4.6 corresponds to location $D2$, centered at $(x, y, z) = (8.69, 0, 3.03)$, which is well inside the flux ropes. The bottom right plot of Figure 4.6 corresponds to location $D4$, centered at $(x, y, z) = (8.83, 0, 3.27)$, which is near the center of the flux ropes. Mixtures of multiple ion beams transmitted from the magnetosheath are seen in the $v_{i\parallel}$-$v_{i\perp 1}$ plane. The presence of multiple ion beams in FTEs has also been reported from satellite observations [e.g., *Hasegawa et al.*, 2006]. The velocity distributions at $D2$, $D4$ feature the highest ion temperatures among the selected locations, with $T_\parallel > T_\perp$ as indicated by the larger extent of the contours in $v_{i\parallel}$ than that in the perpendicular velocity space of $v_{i\perp 1}$ and $v_{i\perp 2}$ (not shown). The majority of ions possess a large positive velocity $v_{i\parallel}$ at $D2$ while the majority of ions at $D4$ possess a large negative velocity $v_{i\perp 1}$. Positive $v_{i\parallel}$ at $D2$ and negative $v_{i\perp 1}$ at $D4$ both indicate that these ions are accelerated northward away from the X line south to the FTE that the four locations are associated with. Several other locations to the north of $D2$ and $D3$ and inside the FTE were "probed" and the results show that ions are also accelerated northward away, which is consistent with the positive V_z shown in the contour plot.

4.2.4 Walén Test of Rotational Discontinuity in a Quasi-Steady Reconnection

To evaluate the influence of the tilt angle of the Earth's dipole field, we have run case 2 with the same parameters except that the tilt angle is chosen to be zero. It is found that under the new condition, X lines also form and move poleward. Although the time scale of the reconnection in case 2 is of the same order as in case 1, the average time of reoccurence of FTEs from the subsolar region in case 2 is longer. The top left plot of Figure 4.7 shows an example of case 2 at $t = 100$, where that the magnetic reconnection structure north to the subsolar looped flux ropes is 'single-X-line-like'. The semi-transparent contour plot shows V_z, the z component of the ion flow velocity in the noon meridian plane, illustrating plasma jets away from X lines. As the plot in fact is a 3-D one with a view from dawn to dusk, the black tubes that sometimes pass through the noon meridian plane are true 3-D field lines.

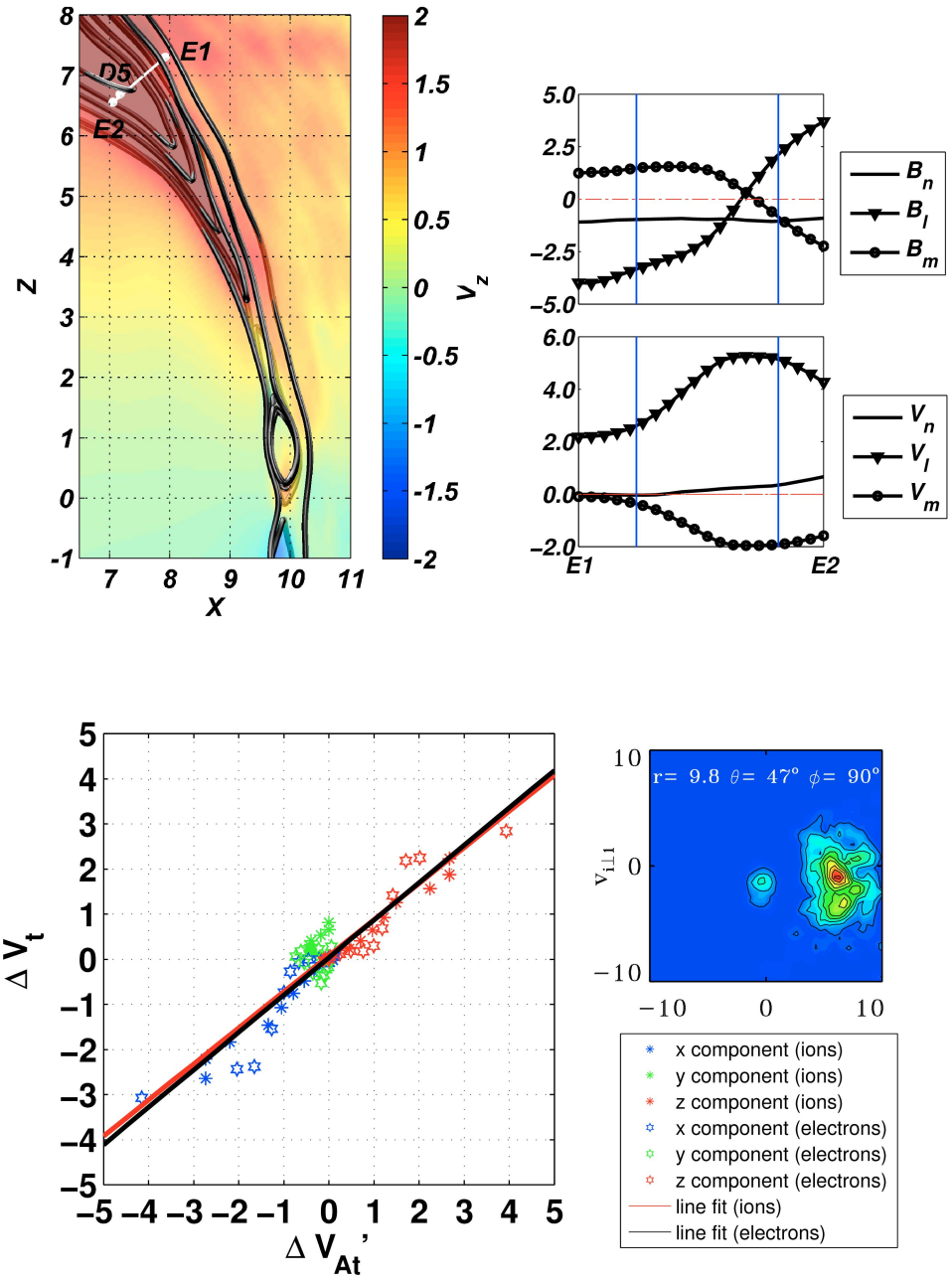

Figure 4.7: Walén test in case 2 in the northern hemisphere at $t = 100$. The top left contour plot shows the ion flow velocity V_z in the noon meridian plane, in which $E1$-$E2$ is a line segment in the r direction across a rotational discontinuity. Spatial cuts of field components B_l, B_m, B_n and ion flow velocities V_l, V_m, V_n along $E1$-$E2$ are shown in the top right plot. The result of Walén test is shown in the bottom left. The ion velocity distribution at location $D5$ between $E1$ and $E2$ is shown in the bottom right.

While the FTE flux ropes are forming at the subsolar region in the northern hemisphere, a rotational discontinuity is found north to the subsolar looped flux ropes, associated with a single X line. Note that in case 1 with a dipole tilt of 15°, the magnetopause is dominated by FTEs as also found in the 3-D global MHD simulation of *Raeder* [2006]. No clear rotational discontinuities are found in case 1.

Both theoretical models [e.g., *Lin and Lee*, 1994], and observations [*Phan et al.*, 1994] show that a large amplitude rotational discontinuity, an intermediate-mode MHD discontinuity, may exist in outflow regions of quasi-steady reconnection at the magnetopause. Here, we examine the existence of a rotational discontinuity in the magnetopause boundary layer in our 3-D global scale hybrid simulation. The Walén relation is applied to identify the rotational discontinuity [*Sonnerup et al.*, 1981], which states that across the rotational discontinuity the tangential plasma flow velocity $\mathbf{V_t}$ changes, as

$$\Delta \mathbf{V_t} = \pm \mathbf{\Delta V_{At}}' = \pm \mathbf{\Delta V_{At}} [\mathbf{1} - (\beta_{\parallel} - \beta_{\perp})/\mathbf{2}]^{\mathbf{1/2}}, \tag{4.1}$$

where $\Delta \mathbf{V_t}$ is the change of the tangential flow velocity across the rotational discontinuity and $\Delta \mathbf{V_{At}}'$ is the corresponding change in the tangential Alfvén velocity corrected by a temperature anisotropy factor. The plus (minus) sign is applied to discontinuities with a normal component of the upstream inflow velocity parallel (anti-parallel) to the normal component of the magnetic field [*Paschmann et al.*, 1986]. In satellite observations [*Sonnerup et al.*, 1981; *Phan et al.*, 1996] and a previous hybrid simulation [*Lin*, 2001], equation (4) is not exactly satisfied. Instead, Walén ratio $A \equiv |\Delta \mathbf{V_t}|/|(\mathbf{\Delta V_{At}}[\mathbf{1} - (\beta_{\parallel} - \beta_{\perp})/\mathbf{2}]^{\mathbf{1/2}})|$ usually ranges from 0.6 to 0.9 for ions, and for electrons the Walén relation can be nearly satisfied [*Scudder et al.*, 1999].

Figure 4.7 shows an example of Walén test around a single X line reconnection site in case 2 in the northern hemisphere at $t = 100$. The contour plot on the upper left side of Figure 4.7 shows the V_z component of ion bulk flow velocity in the noon meridian plane, in which

the black tubes are 3-D field lines. The magnetic field lines in this plot sometimes cross the noon meridian plane, indicating a non-zero B_y component. $E1$-$E2$ is a line segment in the r direction across the discontinuity to be studied below, while $E1$ is at $(x, y, z) = (7.926, 0, 7.3)$ and $E2$ at $(x, y, z) = (7.059, 0, 6.55)$. Point D5 is centered at $(r, \theta, \phi) = (9.8, 47°, 90°)$, also on the path $E1$-$E2$.

A rotational discontinuity is identified along the line cut, of which the local normal direction to the discontinuity, $\hat{\mathbf{n}}$, is determined by the minimum variance method used in Section 3.3. The $\hat{\mathbf{l}}$, $\hat{\mathbf{m}}$, $\hat{\mathbf{n}}$ are $(-0.6643, -0.2307, 0.7110)$, $(0.3281, -0.9446, -0.0000)$ and $(0.6716, 0.2333, 0.7032)$ in the GSM coordinate system, respectively. Spatial cuts of magnetic field components B_l, B_m, B_n and ion flow components V_l, V_m, V_n along $E1$-$E2$ are shown in the top right plot Figure 4.7. Whereas the rotational discontinuity is identified between the two blue vertical lines, across the magnetopause current layer. From $E1$ to $E2$, the normal component of magnetic field remains nearly constant while B_l changes sign. The B_m component, although possessing a sign change too, is dominated by $B_m > 0$, or $B_y < 0$, unlike the quadrupole B_y pattern shown around the case 1 FTEs (Figure 4.3). Through the sharp kinks of field lines from $E1$ to $E2$ across the magnetopause, the dominant flow component V_l is accelerated from 2.5 in the magnetosheath to 5.3 in the boundary layer, a change of $\simeq 1.46$ local Alvén speed, by the field tension force.

The bottom left plot of Figure 4.7 shows the result of the Walén test. Throughout the points from $E1$ to the right blue vertical line along the path $E1$-$E2$, $\Delta\mathbf{V_t}$ is obtained by calculating the difference between local $\mathbf{V_t}$ and that at $E1$ on the upstream side of the discontinuity, and the change in Alfv'en velocity $\Delta\mathbf{V'_{At}}$ is calculated similarly [*Paschmann et al.*, 1986]. The blue, green and red hexagrams represent the change of x, y and z component of electron tangential flow velocity versus the change of $\mathbf{V'_{Atx}}$, $\mathbf{V'_{Aty}}$ and $\mathbf{V'_{Atz}}$, respectively. The star-shaped markers show the data for ions. Linear fitting based on the method of least squares is performed to obtain the Walén ratio. The red line is the line fitting result for ions while the black line for electrons. Both slopes are positive because the inflow velocity is

parallel to the normal component of magnetic field. The Walén ratio for the electron fluid is about 0.83, shown as the slope of black line, and for ions the number is 0.80, shown as the slope of the red line. This rotational discontinuity is not fully developed as expected for discontinuities not far enough from the X line [*Lin*, 2001]. As a result of our simulation, the perturbation in δB_y is small and the slopes of ions and electrons are not well separated as predicted by the two-fluid theory [*Wu and Lee*, 2000].

The bottom right plot of Figure 4.7 shows the ion velocity distributions at location $D5$ in the magnetopause boundary layer. The main population of ions have a positive parallel velocity with a fairly clear cut along a constant minimum $v_{i\parallel}$, and the distributions in the $v_{i\parallel}$-$v_{i\perp 1}$ plane appears to be a D-shaped distribution [*Cowley*, 1982; *Fuselier et al.*, 1991]. A small fraction (5.2%) of ions, which possess near zero average velocities, are the cold ions initially loaded in the magnetosphere. In contrast, no clearly D-shaped velocity distributions of transmitted magnetosheath ions are found at locations around the FTEs in case 1. Along the path $E1$-$E2$, the perpendicular ion temperature $T_\perp$ is larger than the parallel ion temperature $T_\parallel$ on the magnetosheath side while $T_\parallel$ again, increases significantly in the boudary layer near $D5$.

4.2.5 Summary

The main results of this 3-D self-consistent global scale hybrid simulation for cases under a steady, purely southward IMF are summarized below.

1. As a result of magnetic reconnection, magnetic field line configuration in the case with a 15° dipole tilt angle exhibits multiple reconnection sites around the equator and mid-latitude. Flux ropes form spontaneously in between multiple X lines of finite length, which are able to generate clear bipolar signatures of the local normal magnetic field, which has been used to identify FTEs in observations. Around the noon meridian plane, contours of the B_y component show a nearly quadrupole Hall signature near FTEs due to ion kinetic effects. There usually appears an ion density enhancement of plasma core inside the flux

ropes, leading to a filamentary density structure along the reconnected flux tube. Heating and multiple beams of magnetosheath ions are found inside FTEs.

2. Four types of topologies of reconnected magnetic field lines (magnetosphere-to-IMF, IMF-to magnetosphere, IMF-to-IMF, magnetosphere-to-magnetosphere) are obtained in the simulation, which can be explained by combinations of patchy single reconnection and multiple X-line reconnection.

3. In the case in which the dipole tilt angle is 0°, single X line reconnection coexists with multiple-X-line reconnection, while the single X-line process produces 1-D like structures. A Waĺen test is performed to confirm the existence of a rotational discontinuity, which is expected for a quasi-steady like reconnection. A D-shaped ion velocity distribution with a cutoff at minimum $v_{i\|}$ is obtained, whereas no clear D-shaped distributions are developed in the region trailing an FTE closely.

Finally, it should be noted that the scale length λ_0 used in our simulation is about 6 times larger than that in reality. The solar wind convection speed in the simulation is thus 6 times faster than the typical value in reality due to the larger Alf́en speed used in the simulation. The larger convection speed is expected to lead to a faster magnetic flux removal and a shorter reoccurrence period of FTEs at the magnetopause. In the simulation, the average time of reoccurrence of FTEs at the subsolar region is found to be $\sim 60\Omega_0^{-1}$, where $\Omega_0^{-1} \sim 1$s is the ion gyroperiod in the solar wind. Considering the 6 times difference of the convective from reality, the recurrence period of FTEs is estimated to be $6 \times 60s \sim 6min$, which is comparable to that inferred from magnetosphere observations.

Chapter 5

Global Hybrid Simulation of Dayside Magnetic Reconnection Under a Purely Southward IMF: Cusp Precipitating Ions Associated With Magnetopause Reconnection

5.1 Introduction

The dayside cusp is the region where downward precipitating ions reflect magnetic reconnection at the magnetopause. The precipitating cusp particles as observed by satellites inside the magnetosphere often show an energy-latitude dispersion, i.e, decreasing energy with increasing latitude [*Rosenbauer et al.*, 1975; *Reiff et al.*, 1977]. The observed, dispersive structure exhibits 'stepped' ion signatures with variations in flux levels and sudden changes in the energy [*Newell et al.*, 1991]. Two-dimensional models have associated the observed dispersive energy spectra [*Onsager et al.*, 1993; *Lockwood et al.*, 1994] with ongoing magnetic reconnection at the magnetopause. And statistical research shows that the cusp precipitation depends on the magnetopause merging rate in both quantitative and qualitative ways [*Newell et al.*, 2007]. Although researchers have made a lot of efforts to understand them, in some cases ambiguity cannot be eliminated in the interpretation of observed energy spectra of precipitating ions because of limited spatial coverage of spacecrafts [*Onsager et al.*, 1995; *Trattner et al.*, 2007]. Thus, a simulation study will provides a new perspective as it shows direct and clear connection between the large scale magnetic field configuration and local structures of the cusp ion signatures due to magnetopause reconnection.

In Chapter 4, we presented a numerical simulation case of dayside magnetic reconnection during southward interplanetary magnetic field (IMF) with the dipole tilt angle of 15°, focusing on the magnetic configuration and evolution of FTEs. A 3-D global hybrid model was utilized in the simulation, in which the fully-kinetic ion physics is solved in the self-consistent electromagnetic field. In this chapter, we analyze the precipitating ions in the

cusp region from that simulation. In section 2, we briefly describe the simulation model, and the results are presented in section 3, followed by a summary in section 4.

5.2 Simulation Results

5.2.1 Reconnection Events and Spatial Energy Spectrum

Although the frequency of FTEs generation in the northern hemisphere are not exactly the same as that in the southern hemisphere, it is found that the 15 degree sunward dipole tilt does not introduce qualitative interhemispheric asymmetry. In this chapter, we continue to focus on the magnetic reconnection in the northern hemisphere. As the solar wind ions convect carrying the IMF, the bow shock, magnetosheath, and magnetopause gradually form approximately $t > 10$ in a self-consistent manner. The reconnection events discussed in Chapter 4 as well as in this chapter are identified by the connectivity change of magnetic field lines.

The upper panel of Figure 5.1 is basically part of Figure 4.3 in Chapter 4, which illustrates the magnetic field configuration around the magnetopause in the northern hemisphere before $t = 40$. The left 3-D plot shows the magnetic field configuration at $t = 15$. The black lines are magnetic field lines. Note that the magnetic field lines are approximately symmetric about the noon meridian plane. There are two X-line segments shown as in blue dots. Note that other supporting evidence of X lines include the existence of opposite flow jets and the quadrupole magnetic field structure in the guide field, which is discussed in detail as in Chapter 4. Under the purely southward IMF, X line segments are approximately parallel to the equatorial plane along the dayside magnetopause.

In addition to the two X lines illustrated by blue dots, there is another X line below all the FTEs in the 3-D figure and illustrated by red line segments. The reconnection events that we will discuss in this chapter are associated with these three X lines.

The contours in the upper panel of Figure 5.1 show V_z, the z component of ion bulk flow velocity in the noon-midnight meridional plane obtained from case 1. Although two opposite

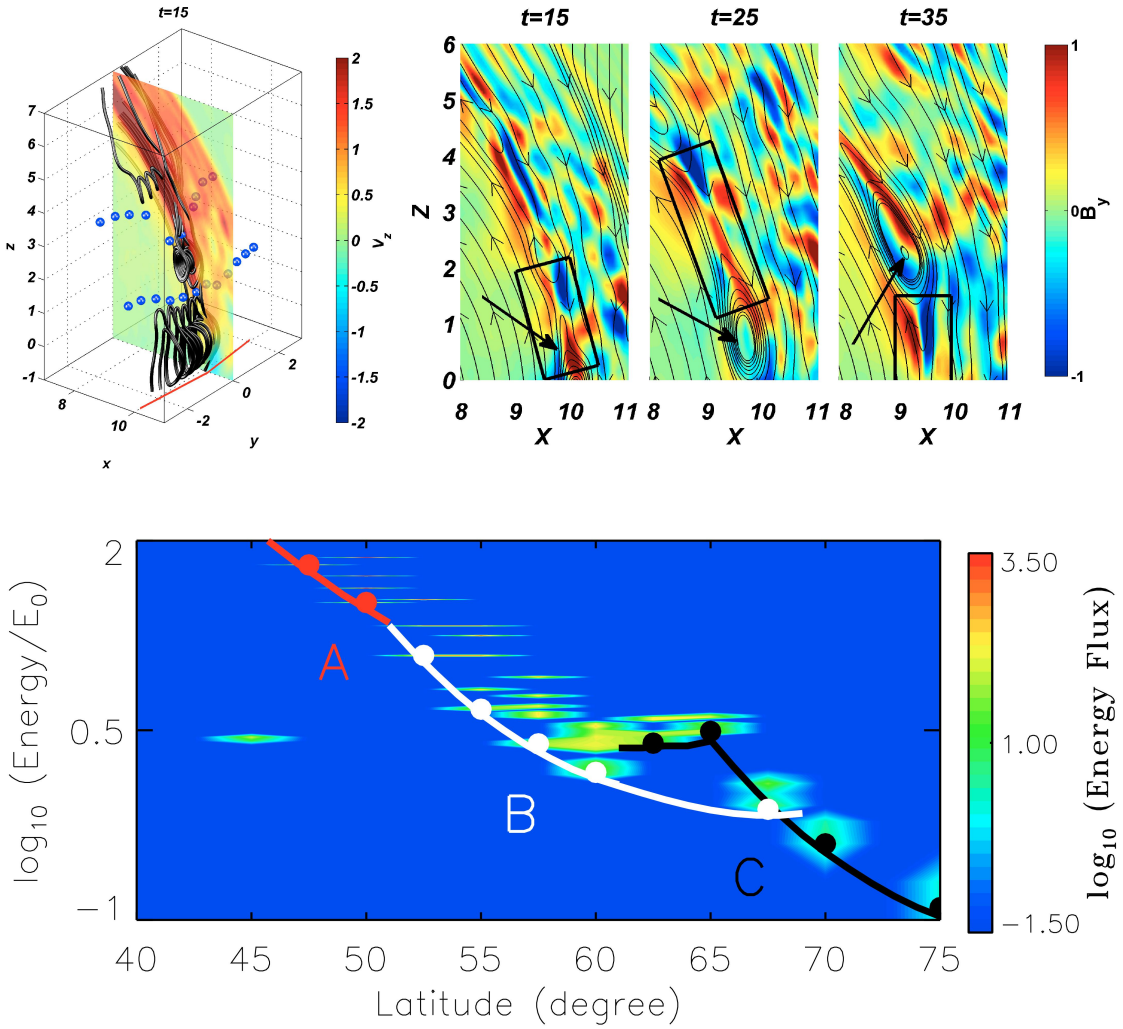

Figure 5.1: (Upper) The 3-D plot in the left shows reconnection X lines in blue dots and red line segment at $t = 15$ with ion bulk flow contours in the noon meridian plane. The contours in the right show B_y component in the noon meridian planes and projected magnetic field lines at $t = 15, 25, 35$, respectively. (Lower) Spatial energy spectrum of cusp precipitating ions in the logarithmic scale showing a dispersive feature. The black, white, and red dots indicate energies of some typical ions at low-cutoff energies of parts A, B, and C, respectively, which are related to three reconnection events.

jets are expected from an X line, the southward jet at $t = 15$ appears missing as seen in the figure for the flux ropes in the middle, due to the the non-zero northward background V_z of the ambient magnetosheath plasmas. The flux ropes that can generate the bipolar signature of FTEs are of an O-line that requires two X lines. The two X lines seen in the 3-D plot of Figure 5.1 move northward as well as the FTEs, which are illustrated by the looped black field lines, as time proceeds.

The three contour plots in the upper panel of Figure 5.1 correspond to B_y components in the noon meridian plane at $t = 15, 25, 35$. The black lines are projected field lines. The boundary region with a dramatic field direction change is the magnetopause. The arrows indicate that the same FTE at the lowest latitude in the 3-D figure of Figure 5.1 is moving northward.

The lower panel of Figure 5.1 shows the typical energy flux spectrum of the precipitating transmitted magnetosheath ions obtained from case 1 during the magnetopause reconnection, where the latitudes are related to the spherical polar angle. Near field-aligned particles with pitch angle less than 10.0° are shown for $r = 7.5\ R_E$. The critical pitch angle is chosen so that it is as close as possible to zero degree while the recorded spectrum includes enough particles. The energy gaps at constant latitudes in the energy spectrum are due to the limited number of 'particles' at the position where ion fluxes are recorded.

It is found that three parts of the spectrum, A, B, and C, shown in the lower panel of Figure 5.1, are related to the entrance areas of the cusp precipitating particles associated with the three reconnection X lines on the magnetopause, as indicated with three lines along the low-energy cutoff, i.e., the minimum energy at each latitude in the spatial spectrum. To interpret observation data, the low-velocity cutoff has been used to infer the reconnection sites on the magnetopause [*Trattner et al.*, 2007] by tracing particles at the low-energy cutoff back along the magnetic field lines. Overall, the resulting particle spectrum in each of the three parts roughly replicates the dispersive feature in spacecraft data under similar IMF conditions [*Onsager et al.*, 1995] that shows higher energy particles at lower latitudes and

lower energy particles at higher latitudes, under IMF conditions similar to the ones in the case shown here. Notice the overlap and 'step' between the low-energy cutoff parts B and C in the spectrum, between latitudes 60° - 70°.

5.3 Precipitating Ions at Low-energy Cutoff

In this subsection, we will explain how and where precipitating ions at low-energy cutoff are transmitted from the solar wind into the magnetosphere via direct magnetic reconnection related to the three X lines shown in Figure 5.1, by tracing the trajectory of the ions. One reconnection region is associated with the X line shown in red line segments, which we will refer to as region A as it is the source region of the ions at the low-energy cutoff in part A of the spectrum we show in Figure 5.1. Similarly, ions at the low-energy cutoff in part B of the spectrum come from the reconnection region associated with the X line in the blue dots at middle latitudes in Figure 5.1. This region is defined as region B. As for ions at the low-energy cutoff in part C of the spectrum, they are found to be from reconnection region associated with the X line in blue dots at high latitudes in Figure 5.1, which is defined as region C.

Figure 5.2 shows the total speed, not the parallel speed only, of precipitating ions as a function of time for typical precipitating ions associated with the reconnection in region A (red curve), region B (orange curve), and region C (blue curve). As indicated by the y axis label, the speed is normalized to the magnitude of Alv́en velocity in the solar wind $|V_{A0}|$.

In the following subsections, we will describe magnetic reconnection in each region as well as their impact on the spatial spectrum shown in Figure 5.1, and explain in Figure 5.2 how the particles at low-energy cutoff accelerate and decelerate during the reconnection process.

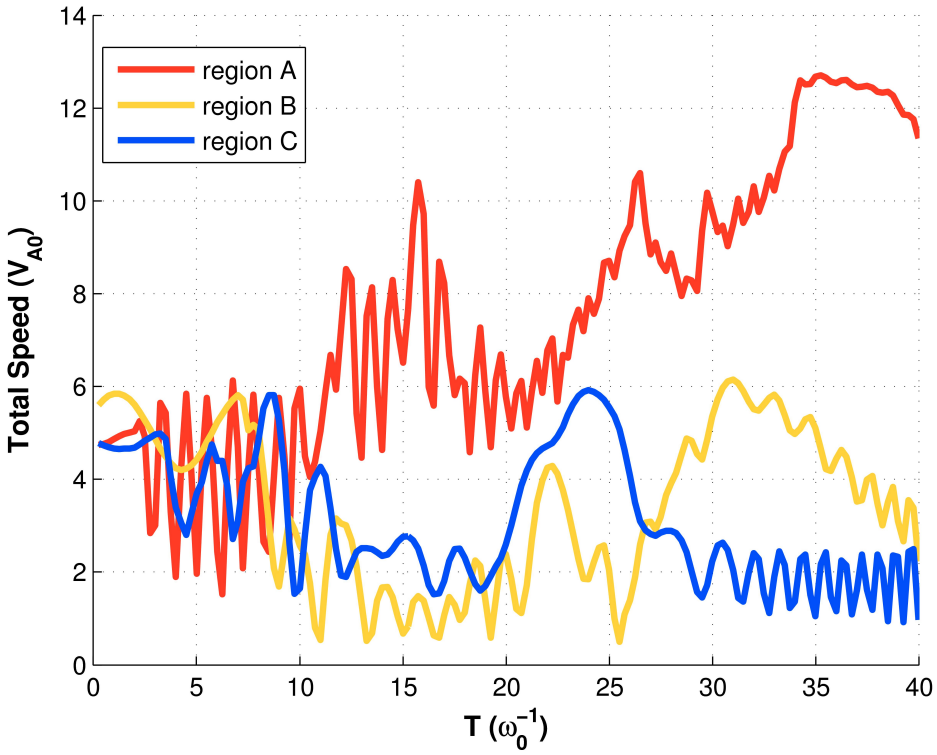

Figure 5.2: Particle speed as a function of time for typical ions associated with reconnection A, B, and C, shown by the red, orange, and blue curves.

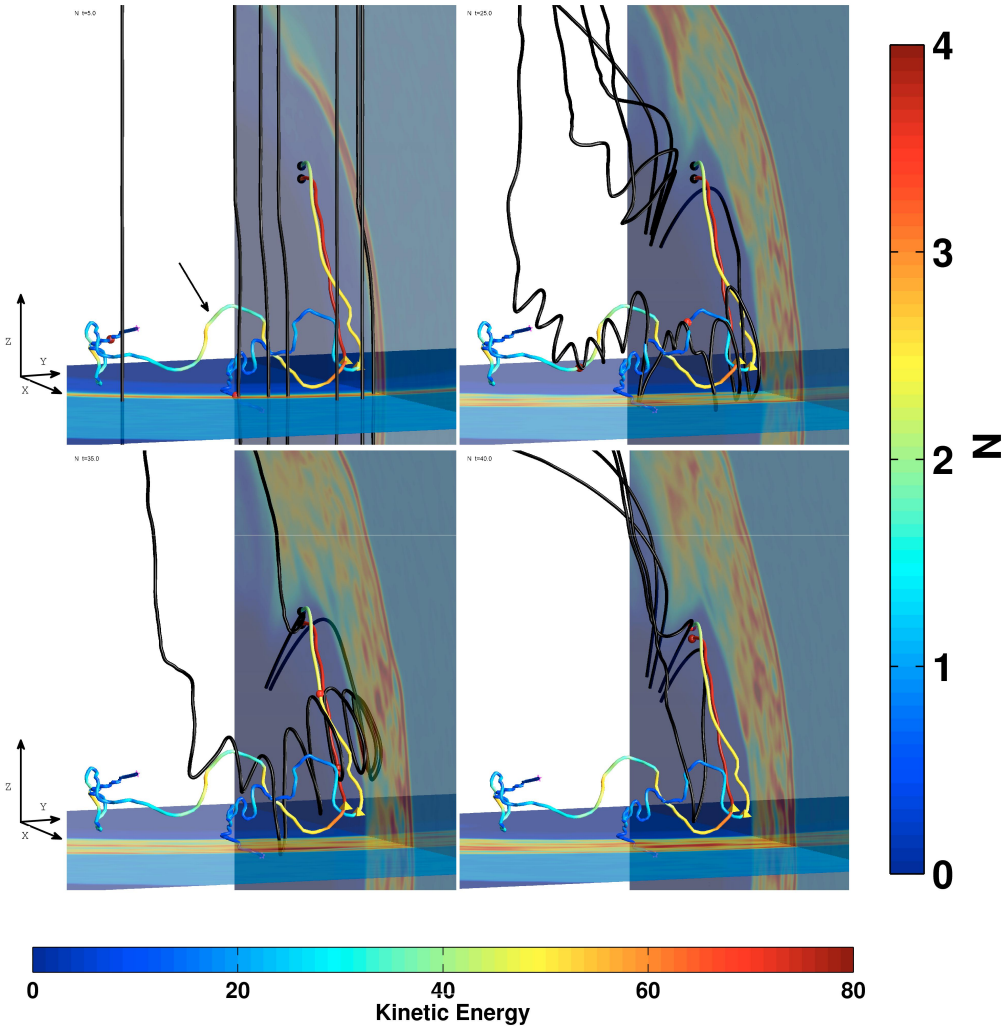

Figure 5.3: The trajectories in colored tubes of particles at low-energy cutoff from region A and the magnetic field configuration in black lines at $t = 5$ (upper left), 25 (upper right), 35 (bottom left) and 40 (bottom right) in the GSM system. Axis direction is shown in the left of either row. The trajectories are color-coded with their current kinetic energy. Also shown are the contours of ion density N

5.3.1 Precipitating Ions at Low-energy Cutoff Associated with Region A

Figure 5.3 shows in the GSM system particle trajectories of the two particles at low-energy cutoff from reconnection in region A, which possess the highest final energies at $t = 40$ and reach the lowest latitudes of 47.5° and 50° at $t = 40$. The trajectories are colored tubes coded logarithmically with the kinetic energies of the particles at each time step. The starting positions of particles are marked with a star. The current positions of particles are marked by colored balls along the trajectories while the black balls indicate the final positions. The kink of a particle trajectory that is the closest to the final position, marked with a yellow pyramid, is where the corresponding particle enters the magnetopause due to magnetic reconnection. The entry region of these particles is well localized near the noon-midnight meridian. The black field lines illustrate magnetic field configuration near the two particles at $t = 5, 25, 35$ and 40. The contours show ion density in the noon meridian and equatorial planes.

The particle ending at the latitude of 47.5° has a final kinetic energy of 64.3, while that ending at the latitude of 50° has a final kinetic energy of 32.4. Note that an ion possessing a speed of $|V_{A0}|$ has kinetic energy of 0.5 in the simulation units. Particles at low-energy cutoff tend to be at locations close to the X lines when magnetic reconnection occurs because a short distance of flight compensates a low parallel speed.

At $t = 5$, both particles are on open field lines, shown in the upper left plot of Figure 5.3. The red curve in Figure 5.2 corresponds the ion at the low-energy cutoff that ends at the latitude of 47.5° in Figure 5.3, has a speed of $v_p \sim 4.5$ around $t = 5$ before entering the magnetopause boundary layer. In the upper left plot of Figure 5.3, the trajectory of the 'red curve' particle has been marked with a black arrow.

At $t \simeq 11$, the 'red curve' particle undergoes gyro-motion plus drift motion as seen from the wiggles in Figure 5.2. It is slightly accelerated to $v_p \sim 7$ at $t \simeq 16$ when being trapped in the flux rope shown in the upper right plot of Figure 5.3. The flux rope forms between

the two X lines we mentioned previously. Note that the two X lines have moved northward, compared to their location at $t = 15$ shown in the upper panel of Figure 5.1.

At $t \simeq 35$ and later, the 'red curve' particle is gradually accelerated to $v_p \sim 12.5$ at $t \simeq 35$ as seen in Figure 5.2 when passing the entry point on the magnetopause marked by the yellow pyramid in Figure 5.3. The entry point is near the X line that is previously shown as red line segments. The speed is increased by nearly twice the local Alfvén speed while reconnected field lines convect with an average speed of ~ 0.9 local Alfvén speed of ~ 1.7, as expected for acceleration in Alfvén type large-amplitude waves in magnetic reconnection [*Lin and Lee*, 1994]. Over all, near the entry point at the magnetopause, the particles are accelerated, while deceleration occurs when they come into the magnetosphere. The acceleration in the FTE is caused by the $\mathbf{E} \times \mathbf{B}$ motion, where the reconnection electric field $\mathbf{E} = -\mathbf{V_e} \times \mathbf{B}$ is nearly in the $+y$ direction. Note that ions become magnetized again after they leave the reconnection sites.

The particle then remains at nearly the same speed while traveling in the boundary layer toward high latitudes until it is slightly decelerated to $v_p \sim 11.4$ at $t = 40$ in the magnetosphere earthward of the kinked field line region of the boundary layer. Because the ion picks up speed mainly in the direction of $\mathbf{E} \times \mathbf{B}$ force, which is perpendicular to the magnetic field, it is decelerated when the field line convection speed (plasma perpendicular speed) drops in the cusp at the final position of the ion.

The average speed of this particle after the entry point at $t = 34$ is about 12.3, which is larger than an average speed of 9.3 for the other particle at the low-energy cutoff and ending at the latitude of 50°. The particle ending at the latitude of 50° enters the magnetopause at $t \simeq 31$, a slightly earlier time than the particle ending latitude 47.5°. A longer time of flight for the slower particle compensates an energy difference of 32.4, which is consistent with the time of flight or velocity filter effect suggested by *Shelley et al.* [1976] and *Reiff et al.* [1977]. Note that only particles moving with a positive parallel velocity relative to the poleward convecting field lines can enter the magnetosphere [*Cowley*, 1982], which should

lead to a D-shaped ion velocity distribution of the transmitted magnetosheath ions if the field line convection speed is nearly a constant, as in quasi-steady reconnection [*Tan et al.*, 2010].

5.3.2 Precipitating Ions at Low-energy Cutoff Associated with Region B

In this subsection, we discuss the precipitating ions at low-energy cutoff associated with region B, of which the trajectories are shown in Figure 5.4. The format of Figure 5.4 is similar with Figure 5.3, except that the trajectories are color coded with the final energy of each particle. Particles precipitating at these latitudes have been accelerated at the middle latitudes in the pre-noon flank of the magnetopause. The ion ending at a latitude of 60° and associated with reconnection B is used as an example in Figure 5.4 to illustrate how the precipitating ions at low-energy cutoff associated with region B enter the magnetopause and reach their final position, of which the speed is shown as the 'orange curve'. In the upper left plot of Figure 5.4, the trajectory of the 'orange curve' particle has been marked with a black arrow.

At $t = 5$, all the particles are on open field lines, shown in the upper left plot of Figure 5.4. As in Figure 5.2, the 'orange curve' ion has an initial speed about the same as that of the 'red curve' particle from region A. Different from the 'red curve' particle, the 'orange curve' particle is originally moving tailward with the magnetosheath bulk flow but then dragged sunward by a reconnected field line on the flank side of the magnetopause, resulting in a deceleration at $t \simeq 10$, as shown in Figure 5.3.

At $t = 15$, one of the particles from region B has passed the entry point and been inside the magnetopause as seen in the upper right plot of Figure 5.4. The 'orange curve' particle enters the magnetopause at $t \simeq 25$ and is then accelerated by a much smaller factor than that of region A due to the weaker kink in the field line and thicker boundary in the higher latitude, reaching only $v_p \sim 6$ around $t \simeq 31$, as shown in Figure 5.2. The motion is then followed by a deceleration in the magnetosphere when the particle loses the perpendicular

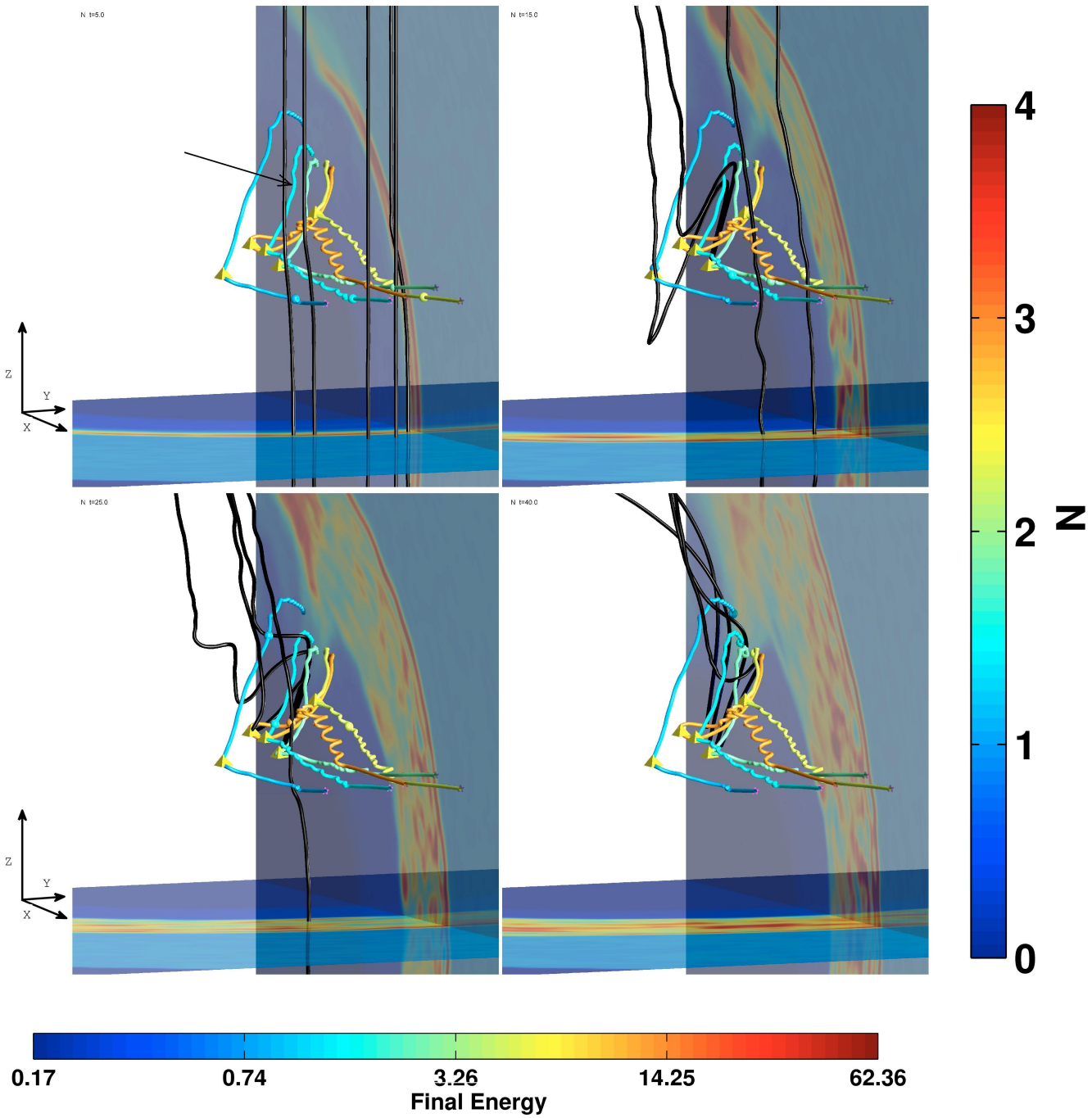

Figure 5.4: The trajectories in colored tubes of particles at low-energy cutoff from region B and the magnetic field configuration in black lines at $t = 5$ (upper left), 25 (upper right), 35 (bottom left) and 40 (bottom right) in the GSM system. Axis direction is shown in the left of either row. The trajectories are color-coded with their final energy. Starting from 52.5°, particles at low-energy latitude in the part B of spectrum have final energies of $12.37, 4.65, 2.47, 1.47$ and 0.82, respectively. Also shown are the contours of ion density N.

speed due to a reduced field line convection speed. It is also found that the site in the cusp where the number of precipitating particles peaks is correlated with region B.

Over all, the mechanism for part B of the dispersive spectrum appears to be quite different from that for part A. The particles at low-energy cutoff enter from region B with a smaller average speed of ~ 4.4, compared to the average speed of 10.8 for region A. The standard deviation of their average energy after entering is less than 5.0, compared with the energy range of 32.4 for region A as we mentioned earlier. Thus, the energy difference is not enough to account for the latitudinal separation in the corresponding cusp spectrum. Rather, particles ending at different latitudes over the spectral range enter the magnetosphere at different times from $t = 15$ to $t = 31$, as the X line moves poleward and sunward and thus the entry points of particles appear to have shifted accordingly. Note that the X line corresponding to region A is located near the equator, of which the poleward movement is less significant than that for the X line of region B.

Particles ending at lower latitudes enter the magnetopause at later times so that by $t = 40$ the corresponding field lines have convected shorter latitudinal distances. The energies of these particles, therefore, must be higher in order to reach the same cusp altitude within the shorter time intervals. Moreover, the foot point of the latest-reconnected field line shifts equatorward with time due to the erosion of magnetospheric field lines within one generation quasi-period of FTEs at the low latitudes under the purely southward IMf as we will show in Figure 5.5, which also contributes to the appearance of higher low-energy cutoff at lower latitudes.

5.3.3 Precipitating Ions at Low-energy Cutoff Associated with Region C

Particles associated with reconnection region C have entry points localized in the pre-noon flank of the high-latitude magnetopause. The trajectories for the precipitating ions at the low-energy cutoff from region C are not shown because they are similar with that from

region B while the typical speed change is shown in Figure 5.2 as the blue curve, which corresponds to the particle that reaches a final position at a latitude of 70°.

Similar to the 'orange curve' particle for region B, the 'blue curve' particle also undergoes a deceleration and then acceleration in the magnetopause, followed by a final deceleration in the magnetosphere. Since the particle enters the magnetosphere from a higher latitude, it is accelerated in an even wider layer at the magnetopause. The particles in part C of the spectrum are around the highest latitudes in the cusp. The field line convection speed (perpendicular plasma speed) becomes small in the northern cusp at the final position of the region C ions, where the radial distance is smaller and the field lines are close to 90 degree of geomagnetic latitude, compared to that at the dayside subsolar region. Thus the energy of the 'blue' particle thus quickly drops back to its original value before the acceleration as the acceleration are mainly perpendicular to the magnetic field due to $\mathbf{E} \times \mathbf{B}$ motion. The fact that three part of the ion spectrum are associated with the three independent X line segments, as in our discussion for Figure 5.1 previously, explains the independency of each part of the spectrum. During the time dependent reconnection, different locations and extensions of the X line segment cause "energy plateaus" and "energy step" between the three parts in the spectrum shown in the lower panel of Figure 5.1.

5.3.4 Energy Flux due to Precipitating Ions as a Function of Time

For satellite observations, energy spectrum is a combination of both spatial and temporal effects. In this section, we focus on the impact of temporal effect on energy spectrum of the cusp precipitation. The upper panel of Figure 5.5 plots energy spectrum as a function of time while our virtual satellite is stationed at the fixed location of $r = 7.5\ R_E$ and latitude of 52.5° in the noon meridian plane. The y axis is the particle energy on a logarithmic scale, while the color represents the energy flux levels, also on a logarithmic scale. The reoccurred of precipitating ions and the trend of the low-energy cutoff in the spectrum are found to be associated with the oscillation of the open/close field line boundary.

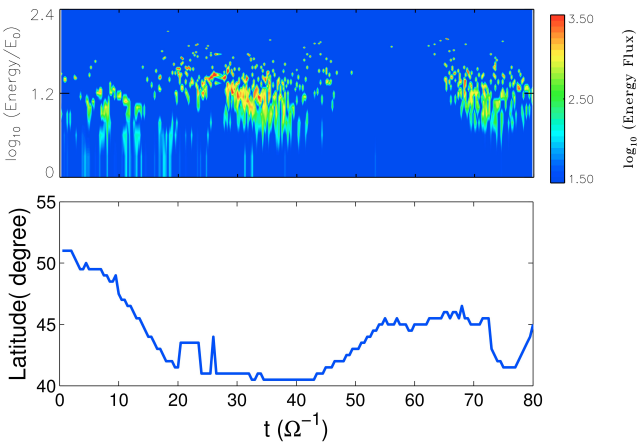

Figure 5.5: (Top) Particle energy spectrum in the logarithmic scale as a function of time at a fixed position of $r = 7.5\ R_E$ and latitude of 52.5°. (Bottom) latitudinal position of the dayside open/close field boundary, at $r = 7.5\ R_E$, as a function of time.

The lower panel of Figure 5.5 plots the latitudinal position of the dayside open/close field line boundary in the noon meridian plane at $r = 7.5$ as a function of time, from $t = 0$ to $t = 80$. The open/closed field line boundary is determined by the reconnection at the lowest latitude (region A) and oscillates with time due to the time variation of the reconnection rate there. Our analysis focuses on the spectrum after $t = 15$ because the spectrum collected in the 'cusp' at earlier stage might be associated with the initialization. From $t = 15$ to $t = 40$, the probe location is well inside the cusp while the open/close field boundary is located at 41° latitude, and a continuous temporal spectrum of ion precipitation is observed. When the open/close field boundary of the low-latitude cusp moves to a higher latitude around $t = 50$, the ion precipitation becomes scarce and then disappears at the specific location. This is because as the cusp moved poleward of the stationary "virtual satellite" so that no precipitating ions are recorded at that location following the poleward motion of the cusp. Later at $t = 70$, the field-aligned ion flux recurs as the open/close field boundary retreats to lower latitudes again.

The low-energy cutoff at $t > 15$, after the formation of the bow shock, magnetosheath, and magnetopause, clearly trends down in the temporal spectrum when the open/closed field boundary of the cusp moves to lower latitudes, and up when the boundary moves to higher

latitudes. Our simulation shows that as the subsolar reconnection (region A) gets weaker, which results in a high-latitude shift of the open/closed field boundary, the magnetopause reconnection is dominated by events at higher latitudes. As reconnection site moves to the higher latitudes, it corresponds to a shorter time of flight for particles ending at the specific cusp latitude, leading to an increased low-energy cutoff of particles.

5.4 Summary

In summary, cusp ion injections associated with magnetopause reconnection are investigated with 3-D hybrid simulation. Under a purely southward IMF, both spatial and temporal energy spectra of cusp precipitating ions are obtained.

The spatial spectrum of field-aligned particles at a constant geocentric radius in the cusp replicates the observed dispersive feature of particles. Multiple parts of the spectrum, however are found to be associated with multiple reconnection events at the dayside magnetopause. Both the multiple X-line reconnection with flux ropes and single-X line type reconnection events result in similar dispersive ion spectra.

In the temporal energy spectrum recorded at a certain location, the occurrence and disappearance of ion precipitation reflect the latitudinal oscillation of the open/closed field line boundary of the cusp. Data from satellite crossings of the cusp are expected to be a combination of the spatial and temporal effects.

The simulations reported here show that the dispersive ion spectra of particles entering the cusp observed by satellites is more involved than the 2-D pictures based upon time of flight effects. It has been shown that (1) the reconnection responsible for the particle entry is neither steady in time nor localized in space; (2) the particle acceleration does not occur at a single point in space and time as the particle crosses a thin magnetopause distinguished by a kink in the field line, but is a much more involved process; and (3) different degrees of acceleration for particles entering the magnetopause at different latitudes also contribute to the latitudinal energy dispersion.

Chapter 6

Dayside Magnetic Reconnection under an IMF with a Finite Guide Field B_y

6.1 Introduction

It is well accepted that the antiparallel reconnection may occur at or near the locus at the dayside magnetopause along which magnetosheath and magnetospheric fields are antiparallel. For purely southward IMF condition, we have shown in Chapter 4 that in our simulation antiparallel reconnection is the dominant reconnection process at the dayside magnetopause, where the reconnecting component of the magnetic field is maximal. Besides anti-parallel reconnection, the component reconnection (or, component merging) hypothesis states that that reconnection can occur at the locations where the shear angle of the magnetic field across the magnetopause is less than 180°.

Recently, observations pointed to that the component reconnection is a competitive process for non-zero B_y conditions. *Chandler et al.* [1999] presented an reconnection event where the spacecraft detected D-shaped ion distributions, which has been considered as a signature of reconnection. In this event, the absence of ions in the antiparallel direction to the upstream magnetic field is taken as the evidence that component reconnection was occurring at a location southward of the spacecraft and equatorward of the Southern Hemisphere cusp under a northward IMF. But so far, when and where the component reconnection occurs at the dayside magnetopause is still not completely understood.

To model the location of reconnection under an IMF of a finite *By*, *Moore et al.* [2002] developed a method to calculate the dayside reconnection X line under different IMF directions. Their hypothesis is that reconnection occurs along a locus determined by integrating the local X line direction away from that region with the largest reconnecting field magnitude. They developed a description of the magnetospheric and magnetosheath magnetic

fields at the magnetopause, compute the angle between the sheath and boundary layer fields, the reconnecting component, and the orientation of the local reconnection X line everywhere on the magnetopause. The direction of local X line is the direction normal to which the two reconnecting fields have equal and opposite component. The last step of Moore's method is to integrate the local X line across the magnetopause from a starting point or points where the reconnecting component is maximal. In this step, to trace the local X line from that point or points is as one would trace the streamlines of any vector field.

Moore's result is shown in Figure 6.1, where the white curve represents the X line on the dayside Magentopause. Note that the clock angle of the IMF is defined as the angle from z direction in the GSM system to the direction of the IMF while the x component of the IMF is zero. Thus, the purely northward IMF has a clock angle of 0° and an IMF of $B_{x0} = 0$,$B_{y0} = 0.707$ and $B_z = -0.707$ has a clock angle of 135°.

A more recent work regarding to the location of dayside reconnection is done by [*Hu et al.*, 2009] through a global MHD simulation. The merging line (black solid line) for different IMF clock angles are projected in the $\phi' - \lambda$ planes as in Figure 6.2, where λ is the latitude, and ϕ' is related to ϕ (defined in Chapter 2) by $\phi' = \phi - 90°$.

Fiugre 6.1 and Figure 6.2 show that the merging line always pass through the subsolar for a non-zero IMF B_y. This indicates that both work support that component reconnection is the reconnection process under a non-zero IMF B_y as the magnetic fields across the subsolar magnetopause are not anti-parallel to each other. For a clock angle of 135°, both Moore and Hu infer that the merging line is located south to the equator plane in the dawn side and north to the equator plane in the dusk side. But over all, the merging line inferred by Moore's group significantly deviated from Hu's result. Under a northward IMF with the clock angle of 45°, the merging lines calculated by Moore have a different shape, compared with Hu's calculation. Under a southward IMF when the clock angle is not 180°, the merging line are in different locations at the flank of the magnetopause in the two models.

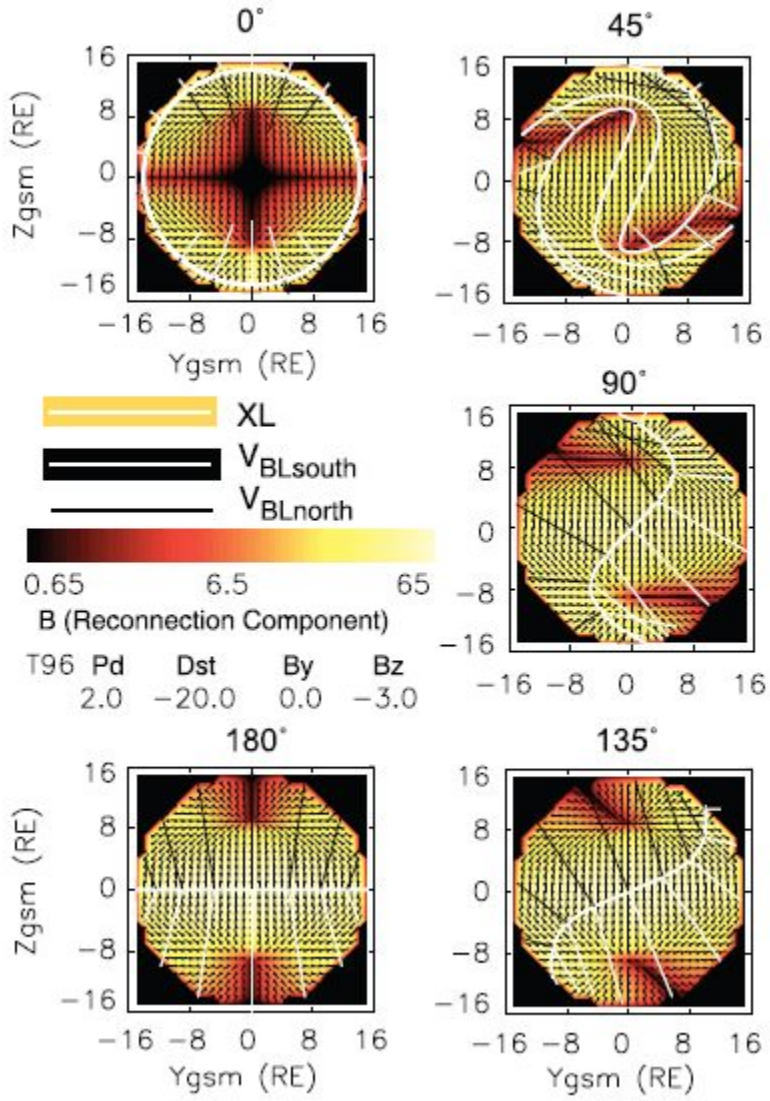

Figure 6.1: The configuration of magnetic field just inside the virtual magnetopause (small black arrows), the reconnecting component magnitude (color scale), and resultant X line (XL) when integrated away from the point of maximal reconnecting component. Boundary layer flow (white and black vectors) for field lines rooted in each hemisphere, on each side of the XL, as projected on the plane normal to a view from the Sun. Individual plots represent the results for various interplanetary magnetic field clock angles according to their labels. Adapted from [*Moore et al.*, 2002]

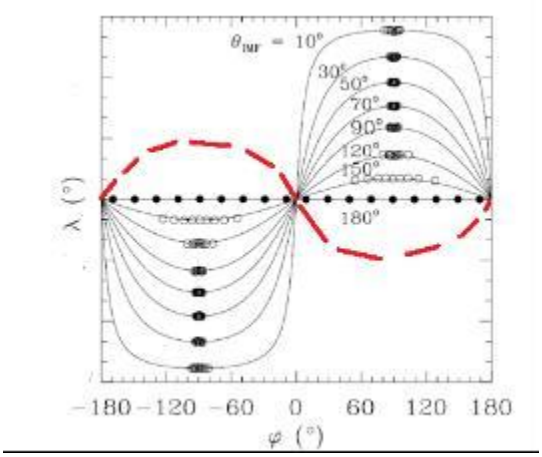

Figure 6.2: Solid black lines shows magnetic merging line of the compound field [*Hu et al.*, 2009], superposed y the Earth's dipole field and the IMF of strength 10nT, projected in the $\phi' - \lambda$ planes for several typical IMF clock angles, where ϕ' stands for the longitude so that $\phi' = 0$ corresponds to the noon meridian plane and λ for the latitude. By symmetry, the merging line for a clock angle of 225°, the clock angle in our simulation is expected as the red dashed line.

Since the location of reconnection under a finite B_y at the dayside magnetopause is still an unsolved issue, in this chapter a simulation for a case under a finite B_y is carried out to investigate the location of the reconnection. The related spectra of precipitating ions at the high latitudes are also obtained and compared with that for a purely southward IMF.

6.2 Simulation Results

As the third case (case 3) presented in this thesis, the initial condition of the simulation is the same as case 1, except that the IMF is $B_{x0} = 0$, $B_{y0} = -0.707$ and $B_z = -0.707$. The corresponding IMF clock angle is 225°.

Figure 6.3 illustrates the typical magnetic field topology near the dayside magnetopause under the given IMF condition. The red field lines are reconnected field lines. The contours of ion density are shown in three planes, the equatorial plane, the noon meridian plane and the meridian plane of $\phi' = -20°$, or $\phi = 70°$. It is found that component magnetic reconnection occurs at a location that magnetic field has a shear angle less than 180° at the

dayside magnetopause, indicated by the red arrow. Furthermore, the dominant location of component reconnection is on the dawn side of the dayside magnetopause (around the plane of $\phi' = -20°$) in the north hemisphere, near the red reconnected field lines. This finding is qualitatively consistent with the merging line at the subsolar magnetopause found by *Hu et al.* [2009] and *Moore et al.* [2002] under the current IMF clock angle.

To understand the ion dynamics associated with reconnection in case 3, we also computed the energy spectra of precipitating cusp ions as a function of time in different planes of $\phi' = constant$. Figure 6.4 shows the temporal spectra in a format similar to that in the upper pannel of Figure 5.5 in the two planes of $\phi' = -20°$ and $\phi' = 20°$.

As shown in Figure 6.4 in the northern hemisphere, ion precipitation is much heavier in the plane of $\phi' = -20°$ than that of $\phi' = 20°$. We argue that this can be explained with the location of merging line, which is located in the northern hemisphere in the dawn side magnetopause ($\phi' < 0°$) and in the southern hemisphere in the dusk side magnetopause ($\phi' > 0°$). The outflow ions from the reconnection sites in one hemisphere are much easier to reach the cusp in the same hemisphere than the opposite hemisphere, given that the plasma convection speed increases as the latitude increases in both hemispheres. Compared with a typical energy spectrum as a function of time in the upper panel of Figure 5.5, the low energy cut-off of cusp precipitating ions in the B_y case is generally lower than that in case 1, a case of purely southward IMF.

As for spatial energy spectrum of cusp precipitating ions, we choose a virtual satellite path at $r = 7.5R_E$ and $t = 40$ in the meridian plane $\phi' = -20°$. As in Chapter 5, precipitating ions with a pitch less than 10° are used to compute the spectrum in Figure 6.5. It is found that the ions at the low energy cut-off in the logarithmic scale indicated by a black line may also exhibit a dispersive feature.

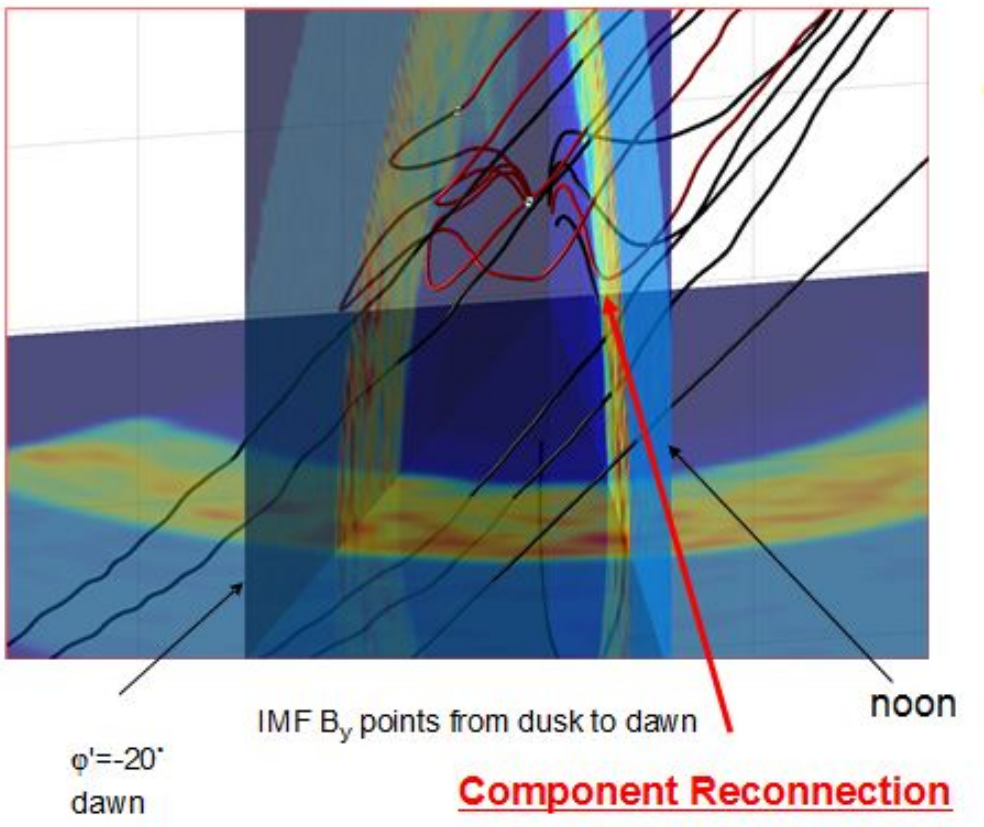

Figure 6.3: Illustration of the location of component magnetic reconnection at the dayside magnetopause when the IMF is $B_{x0} = 0, B_{y0} = -0.707$ and $B_z = -0.707$ as indicated by the red arrow. The red field lines are reconnected field lines. The field lines of the Earth's dipole and the IMF are shown as black lines. The contours of ion density are shown in three planes, the equatorial plane, the noon meridian plane and the maridian plane of $\phi' = -20°$, or $\phi = 70°$. The two boundary regions featuring sharp ion density are the bow shock and magnetopause.

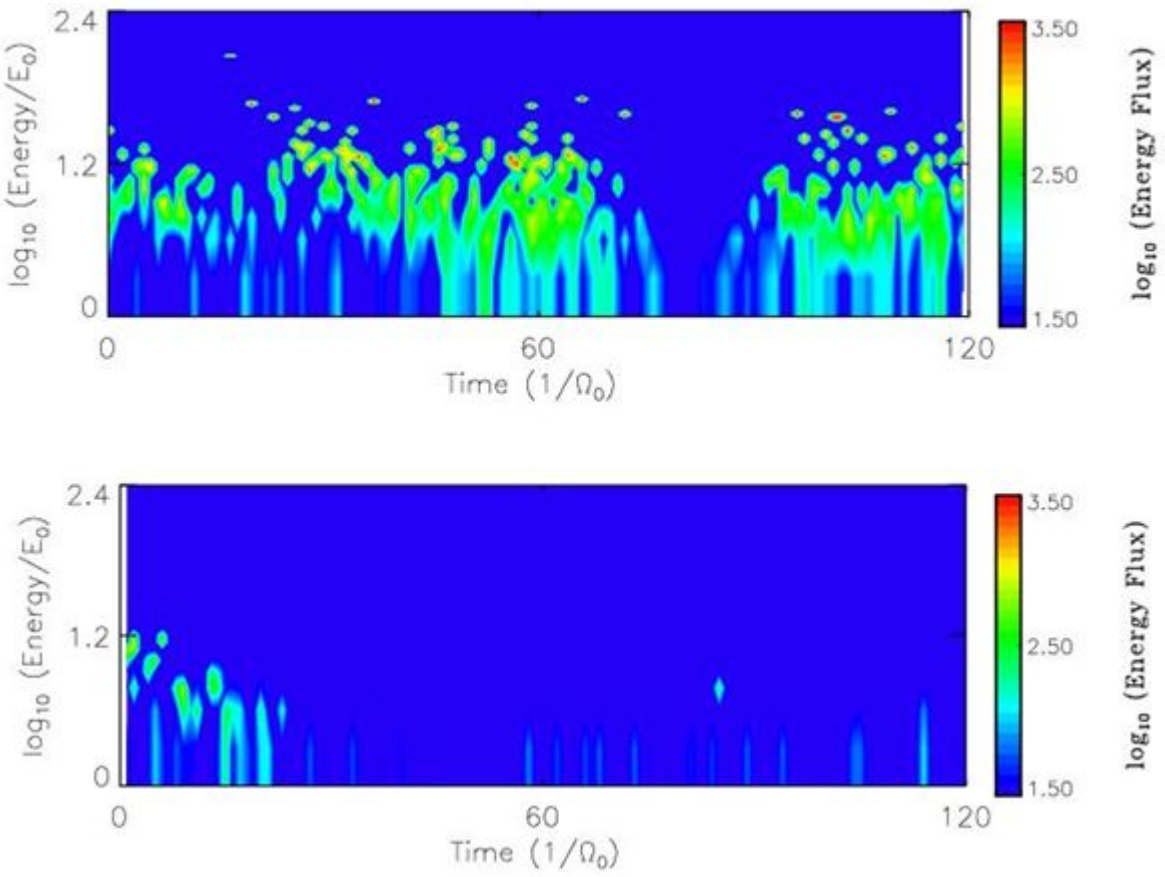

Figure 6.4: Typical spatial energy spectrum of cusp precipitating ions in the logarithmic scale for $r = 7.5R_E$, *Latitude* $= 57.5°$ and $t = 40$, recorded in the plane of $\phi' = -20°$ (upper) and $\phi' = 0°$ (lower)

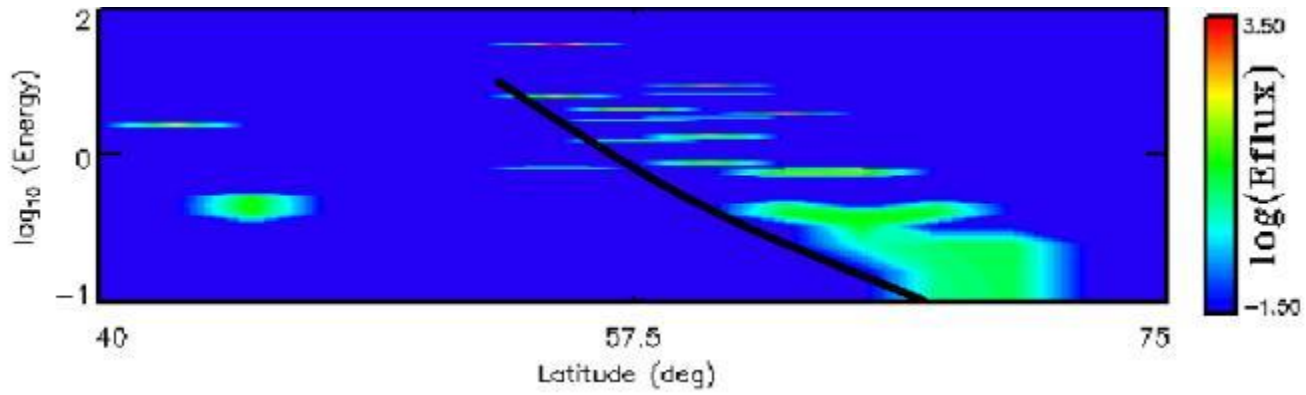

Figure 6.5: Spatial energy spectrum of cusp precipitating ions of $r = 7.5R_E$ and $t = 40$ in the plane $\phi' = -20°$ under a IMF of $B_{x0} = 0, B_{y0} = -0.707$ and $B_z = -0.707$. The low energy cut-off in the logarithmic scale indicated by a black line

6.3 Summary

The investigation of the dayside magnetopause reconnection under the IMF of $B_{x0} = 0$,$B_{y0} = -0.707$ and $B_z = -0.707$ reveals that the component reconnection is the dominant reconnection process, especially near the noon meridian plane, which is confirmed by the location shift of cusp precipitating ions. When the IMF clock angle is larger than 180°, the heaviest precipitation shifts to the dawn side of the dayside magnetopause in the northern hemisphere and to the dusk side of the dayside magnetopause in the southern hemisphere. As for spatial spectra, dispersive feature is also shown in for precipitating ions in the cusp.

Chapter 7

Summary and Future Work

In this work, 3-D global hybrid simulations have been carried out to investigate magnetic reconnection at the magnetopause, using massively parallel computation. Substantial visualization package has been developed to illustrate the 3-D results.

(1) For a case under a purely southward IMF and a tilt angle of 15°, it is found that:

a. FTEs are dominant in a case with a tilt angle of 15 degree. In this case, FTEs can be generated from multiple X line reconnection.

b. There are four types of reconnected field lines, which is confirmed by a recent observation.

c. Quadrapole-like signature of B_y perturbation exists near X lines.

d. There is ion density and parallel ion temperature enhancement inside FTEs. Heating and multiple beams of magnetosheath ions are found inside FTEs.

(2) For a case under a purely southward IMF and a tilt angle of 0°, it is found that:

a. Single X line reconnection is found to be quasi-steady.

b. Rotational Discontinuities (RDs) is identified in quasi-steady reconnection with Walen relation satisfied in RDs.

c. D-shaped ion velocity distributions exists in single X line reconnection, but not in FTEs.

d. The presence of D-shaped and RDs is consistent with observations and previous local hybrid simulations

(3) Energy spectra of cusp precipitating ions are investigated in a case with a purely southward IMF and a tilt angle of 15° and it is found that:

a. Dispersive feature in the low energy cutoff for spatial energy spectra consistent with observations.

b. Different parts in spatial spatial spectra could be associated with different reconnection events and time of flight effect still hold in the 3-D reconnection process, but particle acceleration does not occur at a single point in space/time as the particle crosses the kinked field lines, but is a much more involved process.

c. Different degrees of acceleration for particles entering the magnetopause at different latitudes also contribute to the latitudinal energy dispersion.

(4) IMF B_y effects:

a. The reconnection under an steady southward IMF of a finite B_y is dominated by component reconnection.

b. When the IMF clock angle is larger than 180°, the heaviest precipitation shift to the dawn side of the dayside magnetopause in the northern hemisphere.

c. Dispersive feature is also shown in spatial spectra for precipitating ions in the cusp.

As seen in the previous chapters, the current work only address the impact of the uniform IMF conditions to the magnetosphere. There are a still a lot of questions that demand answers in magnetospheric physics. The following lists a few that we can do.

1. Understand how perturbations in the solar wind such as shocks interacts with the magnetosphere.

2. Time-dependent structures of FTEs: how FTEs decay, where those trapped particles go, how to distinguish a newly formed FTE from an old one?

3. Wave behavior: Alfvén waves? compressional waves?

4. Extend the global scale model to the night side of the Earth. This improvement will enable the model to tackle the problems such as reconnection at the tail, and mechanism of substorms and etc.

5. In the long run, explore the possibility of new models, or incorporate new physics into the current model. Couple the current model to the model that describe the ionosphere

(inside the current domain) and the model that describe the solar wind (outside the current domain), which will expand the applications. Ultimately, the goal could be forecasting the space weather around the Earth as the incoming solar wind varies.

Bibliography

Akasofu, S. I. (1974), Aurora and magnetosphere - chapman memorial lecture, *Planet .Space. Sci.*, *22*(6), 885–923.

Antiochos, S. K., C. R. DeVore, and J. A. Klimchuk (1999), A model for solar coronal mass ejections, *Astron. J.*, *510*(1), 485–493.

Birn, J., and M. Hesse (2001), Geospace environment modeling (gem) magnetic reconnection challenge: Resistive tearing, anisotropic pressure and hall effects, *J. Geophys. Res.*, *106*(A3), 3737–3750.

Birn, J., K. Galsgaard, M. Hesse, M. Hoshino, J. Huba, G. Lapenta, P. L. Pritchett, K. Schindler, L. Yin, J. Buchner, T. Neukirch, and E. R. Priest (2005), Forced magnetic reconnection, *Geophys. Res. Lett.*, *32*(6), L06,105.

Birn, J., J. E. Borovsky, and M. Hesse (2008), Properties of asymmetric magnetic reconnection, *Phys Plasmas*, *15*(3), 032,101, doi:10.1063/1.2888491.

Chandler, M. O., S. A. Fuselier, M. Lockwood, and T. E. Moore (1999), Evidence of component merging equatorward of the cusp, *J. Geophys. Res.*, *104*(A10), 22,623–22,633.

Chaston, C. C., T. D. Phan, J. W. Bonnell, F. S. Mozer, M. Acuna, M. L. Goldstein, A. Balogh, M. Andre, H. Reme, and A. Fazakerley (2005), Drift-kinetic alfven waves observed near a reconnection x line in the earth's magnetopause, *Phys. Rev. Lett.*, *95*(6), 065,002.

Cowley, S. W. H. (1980), Plasma populations in a simple open model magnetosphere, *Space Sci. Rev.*, *26*(3), 217–275.

Cowley, S. W. H. (1982), The causes of convection in the earths magnetosphere - a review of developments during the ims, *Rev. Geophys.*, *20*(3), 531–565.

Cowley, S. W. H. (1996), The earth's magnetosphere, *Eearth in Space*, *8*(6), 9.

Dorelli, J. C., and A. Bhattacharjee (2009), On the generation and topology of flux transfer events, *J. Geophys. Res.*, *114*, A06,213, doi:10.1029/2008JA013410.

Drake, J. F., M. Swisdak, C. Cattell, M. A. Shay, B. N. Rogers, and A. Zeiler (2003), Formation of electron holes and particle energization during magnetic reconnection, *Science*, *299*(5608), 873–877.

Drake, J. F., M. A. Shay, W. Thongthai, and M. Swisdak (2005), Production of energetic electrons during magnetic reconnection, *Phys. Rev. Lett.*, *94*(9), 095,001.

Dungey, J. W. (1961), Interplanetary magnetic field and auroral zones, *Phys. Rev. Lett.*, *6*(2), 47–48.

Fedder, J. A., S. P. Slinker, J. G. Lyon, and C. T. Russell (2002), Flux transfer events in global numerical simulations of the magnetosphere, *J. Geophys. Res.*, *107*(A5), 1048, doi:10.1029/2001JA000025.

Fuselier, S. A., D. M. Klumpar, and E. G. Shelley (1991), Ion reflection and transmission during reconnection at the earths subsolar magnetopause, *Geophys. Res. Lett.*, *18*(2), 139–142.

Fuselier, S. A., K. J. Trattner, and S. M. Petrinec (2000), Cusp observations of high- and low-latitude reconnection for northward interplanetary magnetic field, *Journal of Geophysical Research-space Physics*, *105*(A1), 253–266.

Gosling, J. T., J. R. Asbridge, S. J. Bame, W. C. Feldman, G. Paschmann, N. Sckopke, and C. T. Russell (1982), Evidence for quasi-stationary reconnection at the dayside magnetopause, *J. Geophys. Res.*, *87*(NA4), 2147–2158.

Gosling, J. T., M. F. Thomsen, S. J. Bame, and C. T. Russell (1986), Accelerated plasma flows at the near-tail magnetopause, *J. Geophys. Res.*, *91*(A3), 3029–3041.

Gosling, J. T., M. F. Thomsen, S. J. Bame, T. G. Onsager, and C. T. Russell (1990), The electron edge of the low latitude boundary-layer during accelerated flow events, *Geophys. Res. Lett.*, *17*(11), 1833–1836.

Hasegawa, H., B. U. O. Sonnerup, C. J. Owen, B. Klecker, G. Paschmann, A. Balogh, and H. Reme (2006), The structure of flux transfer events recovered from cluster data, *Ann. Geophys.*, *24*(2), 603–618.

Hesse, M., and D. Winske (1998), Electron dissipation in collisionless magnetic reconnection, *Journal of Geophysical Research-space Physics*, *103*(A11), 26,479–26,486.

Hoshino, M. (1987), The electrostatic effect for the collisionless tearing mode, *J. Geophys. Res.*, *92*(A7), 7368–7380.

Hu, Y. Q., Z. Peng, C. Wang, and J. R. Kan (2009), Magnetic merging line and reconnection voltage versus imf clock angle: Results from global mhd simulations, *Journal of Geophysical Research-space Physics*, *114*, A08,220.

Huba, J. D. (2009), *NRL plasma formulary*, Naval Research Laboratory.

Hughes, W. J. (1995), Magnetic reconnection, in *Introduction to space physics*, edited by M. G. Kivelson and C. T. Russell, pp. 227–287, Cambridge Univeristy Press, Cambridge, United Kingdom.

Hundhausen, A. J. (1995), The solar wind, in *Introduction to space physics*, edited by M. G. Kivelson and C. T. Russell, pp. 91–128, Cambridge Univeristy Press, Cambridge, United Kingdom.

Kan, J. R. (1988), A theory of patchy and intermittent reconnections for magnetospheric flux-transfer events, *J. Geophys. Res.*, *93*(A6), 5613–5623.

Karimabadi, H., D. Krauss-Varban, N. Omidi, and H. X. Vu (1999), Magnetic structure of the reconnection layer and core field generation in plasmoids, *J. Geophys. Res.*, *104*(A6), 12,313–12,326.

Karimabadi, H., W. Daughton, and K. B. Quest (2005), Antiparallel versus component merging at the magnetopause: Current bifurcation and intermittent reconnection, *J. Geophys. Res.*, *110*(A3), A03,213.

Klumpar, D. M., S. A. Fuselier, and E. G. Shelley (1990), Ion composition measurements within magnetospheric flux-transfer events, *Geophys. Res. Lett.*, *17*(13), 2305–2308.

Kraussvarban, D., and N. Omidi (1995), Large-scale hybrid simulations of the magnetotail during reconnection, *Geophys. Res. Lett.*, *22*(23), 3271–3274.

Kuznetsova, M. M., M. Hesse, and D. Winske (2000), Toward a transport model of collisionless magnetic reconnection, *J. Geophys. Res.*, *105*(A4), 7601–7616.

Kuznetsova, M. M., D. G. Sibeck, M. Hesse, Y. Wang, L. Rastaetter, G. Toth, and A. Ridley (2009), Cavities of weak magnetic field strength in the wake of ftes: Results from global magnetospheric mhd simulations, *Geophys. Res. Lett.*, *36*, L10,104.

Lee, L. C., and Z. F. Fu (1985), A theory of magnetic-flux transfer at the earths magnetopause, *Geophys. Res. Lett.*, *12*(2), 105–108.

Lee, L. C., Z. W. Ma, Z. F. Fu, and A. Otto (1993), Topology of magnetic-flux ropes and formation of fossil flux-transfer events and boundary-layer plasmas, *J. Geophys. Res.*, *98*(A3), 3943–3951.

Levy, R. H., H. E. Petschek, and G. L. Siscoe (1964), Aerodynamic aspects of the magnetospheric flow, *Aiaa Journal*, *2*(12), 2065–2076.

Lin, Y. (2001), Global hybrid simulation of the dayside reconnection layer and associated field-aligned currents, *J. Geophys. Res.*, *106*(A11), 25,451–25,465.

Lin, Y., and L. C. Lee (1994), Structure of reconnection layers in the magnetosphere, *Space Sci. Rev.*, *65*(1-2), 59–179.

Lin, Y., and L. C. Lee (1999), Reconnection layers in two-dimensional magnetohydrodynamics and comparison with the one-dimensional riemann problem, *Phys. Plasmas*, *6*(8), 3131–3146.

Lin, Y., and D. W. Swift (1996), A two-dimensional hybrid simulation of the magnetotail reconnection layer, *J. Geophys. Res.*, *101*(A9), 19,859–19,870.

Lin, Y., and X. Y. Wang (2005), Three-dimensional global hybrid simulation of dayside dynamics associated with the quasi-parallel bow shock, *J. Geophys. Res.*, *110*(A12), A12,216.

Lockwood, M., and M. F. Smith (1992), The variation of reconnection rate at the dayside magnetopause and cusp ion precipitation, *Journal Of Geophysical Research-Space Physics*, *97*(A10), 14,841–14,847.

Lockwood, M., T. G. Onsager, C. J. Davis, M. F. Smith, and W. F. Denig (1994), The characteristics of the magnetopause reconnection x-line deduced from low-altitude satellite-observations of cusp ions, *Geophysical Research Letters*, *21*(24), 2757–2760.

Lui, A. T. Y., D. G. Sibeck, T. Phan, J. P. McFadden, V. Angelopoulos, and K. H. Glassmeier (2008), Reconstruction of a flux transfer event based on observations from five themis satellites, *J. Geophys. Res.*, *113*, A00C01.

Marcucci, M. G., and J. E. Polk (2000), Nstar xenon ion thruster on deep space 1: ground and flight tests (invited), *Rev. Sci. Instrum.*, *71*(3), 1389–1400.

Meyer-Vernet, N. (2007), Structure and perturbations, in *Basics of the solar wind*, pp. 291–333, Cambridge Univeristy Press, Cambridge, United Kingdom.

Moore, T. E., M. C. Fok, and M. O. Chandler (2002), The dayside reconnection x line, *Journal of Geophysical Research-space Physics*, *107*(A10), 1332.

Nakamura, M., and M. Scholer (2000), Structure of the magnetopause reconnection layer and of flux transfer events: Ion kinetic effects, *J. Geophys. Res.*, *105*(A10), 23,179–23,191.

Newell, P. T., W. J. Burke, C. I. Meng, E. R. Sanchez, and M. E. Greenspan (1991), Identification and observations of the plasma mantle at low altitude, *Journal Of Geophysical Research-Space Physics*, *96*(A1), 35–45.

Newell, P. T., S. Wing, and F. J. Rich (2007), Cusp for high and low merging rates, *J. Geophys. Res.*, *112*(A9), A09,205.

Omidi, N., and D. G. Sibeck (2007), Flux transfer events in the cusp, *Geophys. Res. Lett.*, *34*(4), L04,106.

Onsager, T. G., C. A. Kletzing, J. B. Austin, and H. Mackiernan (1993), Model of magnetosheath plasma in the magnetosphere - cusp and mantle particles at low-altitudes, *Geophysical Research Letters*, *20*(6), 479–482.

Onsager, T. G., S. W. Chang, J. D. Perez, J. B. Austin, and L. X. Janoo (1995), Low-altitude observations and modeling of quasi-steady magnetopause reconnection, *J. Geophys. Res.*, *100*(A7), 11,831–11,843.

Paschmann, G., G. Haerendel, I. Papamastorakis, N. Sckopke, S. J. Bame, J. T. Gosling, and C. T. Russell (1982), Plasma and magnetic-field characteristics of magnetic-flux transfer events, *J. Geophys. Res.*, *87*(NA4), 2159–2168.

Paschmann, G., I. Papamastorakis, W. Baumjohann, N. Sckopke, C. W. Carlson, B. U. O. Sonnerup, and H. Luhr (1986), The magnetopause for large magnetic shear - ampte/irm observations, *J. Geophys. Res.*, *91*(A10), 1099–1115.

Patsourakos, S., and A. Vourlidas (2011), Evidence for a current sheet forming in the wake of a coronal mass ejection from multi-viewpoint coronagraph observations, *Astron. Astrophys.*, *525*, A27.

Petschek, H. E. (1964), Magnetic field annihilation, in *AAS-NASA symposium on the physics of solar flares*, vol. SP, pp. 425–439, NASA Spec. Publ.

Phan, T. D., G. Paschmann, W. Baumjohann, N. Sckopke, and H. Luhr (1994), The magnetosheath region adjacent to the dayside magnetopause - ampte/irm observations, *J. Geophys. Res.*, *99*(A1), 121–141.

Phan, T. D., G. Paschmann, and B. U. O. Sonnerup (1996), Low-latitude dayside magnetopause and boundary layer for high magnetic shear .2. occurrence of magnetic reconnection, *J. Geophys. Res.*, *101*(A4), 7817–7828.

Phan, T. D., C. P. Escoubet, L. Rezeau, R. A. Treumann, A. Vaivads, G. Paschmann, S. A. Fuselier, D. Attie, B. Rogers, and B. U. O. Sonnerup (2005), Magnetopause processes, *Space Science Reviews*, *118*(1-4), 367–424.

Pinnock, M., A. S. Rodger, J. R. Dudeney, F. Rich, and K. B. Baker (1995), High spatial and temporal resolution observations of the ionospheric cusp, *Ann. Geophys.*, *13*(9), 919–925.

Pizzo, V. J. (1985), Interplanetary shock on the large scale: a retrospective on the last decade's theoretical efforts., in *Collisonless shocks in the helisphere: reviews of current research*, edited by B. T. Tsurutani and R. G. Stone, pp. 51–68, American Geophyiscal Union, Washington, DC.

Price, C. P., D. W. Swift, and L. C. Lee (1986), Numerical-simulation of nonoscillatory mirror waves at the earths magnetosheath, *J. Geophys. Res.*, *91*(A1), 101–112.

Priest, E. R., and T. Forbes (2000a), Introduction, in *Magnetic reconnection: MHD theory and applications*, pp. 1–39, Cambridge Univeristy Press, Cambridge, United Kingdom.

Priest, E. R., and T. Forbes (2000b), *Magnetic reconnection: MHD theory and applications*, 231-245 pp., Cambridge Univeristy Press, Cambridge, United Kingdom.

Pritchett, P. L. (2001), Geospace environment modeling magnetic reconnection challenge: Simulations with a full particle electromagnetic code, *J. Geophys. Res.*, *106*(A3), 3783–3798.

Raeder, J. (2006), Flux transfer events: 1. generation mechanism for strong southward imf, *Ann. Geophys.*, *24*(1), 381–392.

Reiff, P. H., T. W. Hill, and J. L. Burch (1977), Solar-wind plasma injection at dayside magnetospheric cusp, *J. Geophys. Res.*, *82*(4), 479–491.

Rijnbeek, R. P., S. W. H. Cowley, D. J. Southwood, and C. T. Russell (1984), A survey of dayside flux-transfer events observed by isee-1 and isee-2 magnetometers, *J. Geophys. Res.*, *89*(NA2), 786–800.

Rosenbauer, H., H. Grunwaldt, M. D. Montgomery, G. Paschmann, and N. Sckopke (1975), Heos-2 plasma observations in distant polar magnetosphere - plasma mantle, *Journal Of Geophysical Research-Space Physics*, *80*(19), 2723–2737.

Russell, C. T. (1995), The structure of the magnetosphere, in *Physics of the magnetopause*, edited by P. Song, B. O. U. Sonnerup, and M. F. Thomsen, pp. 81–108, American Geophyiscal Union, Washington, DC.

Russell, C. T., and R. C. Elphic (1978), Initial isee magnetometer results - magnetopause observations, *Space Sci. Rev.*, *22*(6), 681–715.

Russell, C. T., G. Le, and H. Kuo (1995), The occurrence rate of flux transfer events, in *Three-dimensional magnetopshere*, vol. 18, edited by J. Buchner, pp. 197–205, Pergamon Press Ltd., Oxford, England.

Russell, C. T., G. Le, and S. M. Petrinec (2000), Cusp observations of high- and low-latitude reconnection for northward imf: An alternate view, *J. Geophys. Res.*, *105*(A3), 5489–5495.

Scholer, M. (1988), Magnetic-flux transfer at the magnetopause based on single x-line bursty reconnection, *Geophys. Res. Lett.*, *15*(4), 291–294.

Scholer, M. (1989a), Asymmetric time-dependent and stationary magnetic reconnection at the dayside magnetopause, *J. Geophys. Res.*, *94*(A11), 15,099–15,111.

Scholer, M. (1989b), Undriven magnetic reconnection in an isolated current sheet, *J. Geophys. Res.*, *94*(A7), 8805–8812.

Scholer, M., I. Sidorenko, C. H. Jaroschek, R. A. Treumann, and A. Zeiler (2003), Onset of collisionless magnetic reconnection in thin current sheets: Three-dimensional particle simulations, *Phys. Plasmas.*, *10*(9), 3521–3527, doi:10.1063/1.1597494.

Scudder, J. D., P. A. Puhl-Quinn, F. S. Mozer, K. W. Ogilvie, and C. T. Russell (1999), Generalized walen tests through alfven waves and rotational discontinuities using electron flow velocities, *J. Geophys. Res.*, *104*(A9), 19,817–19,833.

Shay, M. A., J. F. Drake, B. N. Rogers, and R. E. Denton (2001), Alfvenic collisionless magnetic reconnection and the hall term, *J. Geophys. Res.*, *106*(A3), 3759–3772.

Shelley, E. G., R. D. Sharp, and R. G. Johnson (1976), Satellite-observations of an ionospheric acceleration mechanism, *Geophys. Res. Lett.*, *3*(11), 654–656.

Shi, Y., and L. C. Lee (1990), Structure of the reconnection layer at the dayside magnetopause, *Planet. Space. Sci.*, *38*(3), 437–458.

Sibeck, D. G., and R. Q. Lin (2010), Concerning the motion of flux transfer events generated by component reconnection across the dayside magnetopause, *Journal of Geophysical Research-space Physics*, *115*, A04,209, doi:10.1029/2009JA014677.

Sonnerup (1979), Magnetic field reconnection, in *Solar System Plasma Physics*, edited by C. F. K. L. T. Lanzerotti and E. N. Parker, pp. 46–108, North-Holland, New York, U. S.

Sonnerup, B. U., and L. J. Cahill (1967), Magnetopause structure and attitude from explorer 12 observations, *J Geophys. Res.*, *72*(1), 171–183.

Sonnerup, B. U. O., G. Paschmann, I. Papamastorakis, N. Sckopke, G. Haerendel, S. J. Bame, J. R. Asbridge, J. T. Gosling, and C. T. Russell (1981), Evidence for magnetic-field reconnection at the earths magnetopause, *J. Geophys. Res.*, *86*(NA12), 49–67.

Swift, D. W. (1996), Use of a hybrid code for global-scale plasma simulation, *J. Comput. Phys.*, *126*(1), 109–121.

Terasawa, T. (1981), Numerical study of explosive tearing mode-instability in one-component plasmas, *J. Geophys. Res.*, *86*(NA11), 9007–9019.

Terasawa, T. (1983), Hall current effect on tearing mode-instability, *Geophys. Res. Lett.*, *10*(6), 475–478.

Trattner, K. J., J. S. Mulcock, S. M. Petrinec, and S. A. Fuselier (2007), Probing the boundary between antiparallel and component reconnection during southward interplanetary magnetic field conditions, *J. Geophys. Res.*, *112*(A8), A08,210.

Uberoi, C. (2003), A unified theory for micropulsation and flux transfer events, in *Very low frequency (VLF) phenomena*, edited by A. R. W. Hughes, C. Ferencz, and A. K. Gwal, pp. 164–174, Narosa Publishing House, Delhi, India.

Winglee, R. M., E. Harnett, A. Stickle, and J. Porter (2008), Multiscale/multifluid simulations of flux ropes at the magnetopause within a global magnetospheric model, *J. Geophys. Res.*, *113*(A2), A02,209.

Wu, B. H., and L. C. Lee (2000), Hall effects on the walen relation in rotational discontinuities and alfven waves, *J. Geophys. Res.*, *105*(A8), 18,377–18,389.

Yan, M., L. C. Lee, and E. R. Priest (1992), Fast magnetic reconnection with small shock angles, *J. Geophys. Res.*, *97*(A6), 8277–8293.

Bibliography

Appendices

Appendix A

Fundamental Plasma Parameters

Physical Quantity	Symbol	Definition
Alfvén velocity	$\mathbf{V_A}$	$\frac{\mathbf{B}}{4\pi n_i m_i}$
Debye length	λ_D	$(\frac{kT}{4\pi ne^2})^{0.5}$
ion gyrofrequency	ω_i	ZeB/m_ic
ion gyroradius	r_i	v_{T_i}/ω_i
ion plasma frequency	ω_{pi}	$(4\pi n_i Z^2 e^2/m_i)^{\frac{1}{2}}$
ion thermal velocity	v_{T_i}	$(\frac{kT_i}{m_i})^{0.5}$
ion inertial length	λ_i	c/ω_{pi}
magnetic mach number	M	V/V_A

Table A.1: Fundamental plasma parameters, adapted from *Huba* [2009]. (All quantities are in Gaussian cgs units except that temperature expressed in eV and ion mass in units of the proton mass.)

Appendix B

Maxwell's Equations

Name	SI	Gaussian
Faraday's law	$\nabla \times \mathbf{E} = -\frac{\partial \mathbf{B}}{\partial \mathbf{t}}$	$\nabla \times \mathbf{E} = -\frac{\mathbf{1}}{\mathbf{c}} \frac{\partial \mathbf{B}}{\partial \mathbf{t}}$
Ampere's law	$\nabla \times \mathbf{H} = -\frac{\partial \mathbf{D}}{\partial \mathbf{t}} + \mathbf{J}$	$\nabla \times \mathbf{H} = \frac{\mathbf{1}}{\mathbf{c}} \frac{\partial \mathbf{D}}{\partial \mathbf{t}} + \frac{\mathbf{4\pi}}{\mathbf{c}} \mathbf{J}$
Poisson equation	$\nabla \cdot \mathbf{D} = \rho$	$\nabla \cdot \mathbf{D} = \mathbf{4}\pi\rho$
[Absence of magnetic monopoles]	$\nabla \cdot \mathbf{B} = \mathbf{0}$	$\nabla \cdot \mathbf{B} = \mathbf{0}$
Lorentz force on charge q	$q(\mathbf{E} + \mathbf{v} \times \mathbf{B})$	$q(\mathbf{E} + \frac{\mathbf{1}}{\mathbf{c}} \mathbf{v} \times \mathbf{B})$
Constitutive relations	$\mathbf{D} = \epsilon \mathbf{E}$ $\mathbf{B} = \mu \mathbf{H}$	$\mathbf{D} = \epsilon \mathbf{E}$ $\mathbf{B} = \mu \mathbf{H}$

Table B.1: Maxwell's equations, adapted from *Huba* [2009].
In a plasma $\mu \approx \mu_0 = 4\pi \times 10^{-7} Hm^{-1}$ (Gaussian units: $\mu \approx 1$). The permittivity satisfies $\epsilon \approx \epsilon_0 = 8.8542 \times 10^{-12} Fm^{-1}$ (Gaussian units: $\epsilon \approx 1$)

Appendix C

Sample Subroutine in MATLAB: GUI of Finetuning Field Line

```
function MyGui(action) global Field;


global param;
global myplt;
global Handle0 Handle1 Handle2 Handle3;
% Generates GUI menu popup_index = get(Handle1.popupmenu, 'Value');
switch popup_index
case 1
% Call the subroutine of Field Line Finetuning
BlineFineTuneGui;
case 2
minimum_variance;
case 3
return;
end
```

Appendix D

Sample Subroutine in MATLAB: Finetuning Field Line

```
function BlineFineTune(step,direction)


global Field;
global param;
global myplt;
global c_info;
global V3D_HANDLES;
global Handle0 Handle1 Handle2 Handle3;
figure_handle=V3D_HANDLES.figure_handle;
axis_handle=V3D_HANDLES.axis_handle;
handles=V3D_HANDLES.handles;
figure(figure_handle) ;
figure(handles.figure1);
hold on;
if (myplt.Bline.sx==0 && myplt.Bline.sy==0 && myplt.Bline.sz==0) ,
myplt.Bline.sx=15;
myplt.Bline.sy=0;
myplt.Bline.sz=0;
return;
else
switch direction
case 1
myplt.Bline.sx=myplt.Bline.sx+step;
myplt.Bline.sy=myplt.Bline.sy;
myplt.Bline.sz=myplt.Bline.sz;
case 2
myplt.Bline.sx=myplt.Bline.sx;
myplt.Bline.sy=myplt.Bline.sy+step;
myplt.Bline.sz=myplt.Bline.sz;
case 3
myplt.Bline.sx=myplt.Bline.sx;
myplt.Bline.sy=myplt.Bline.sy;
myplt.Bline.sz=myplt.Bline.sz+step;
end;
end;
```

```
[n1,n2]=size(myplt.Bline.numexist);
if n2>=1 ;
delete(myplt.Bline.h1(myplt.Bline.numexist(1)));
end;
%[sx, sy, sz]: the starting point where we begin to trace the field lines.
sx=myplt.Bline.sx;
sy=myplt.Bline.sy;
sz=myplt.Bline.sz;
x=myplt.plot3D.x3;
y=myplt.plot3D.y3;
z=myplt.plot3D.z3;
u=myplt.plot3D.u;
v=myplt.plot3D.v;
w=myplt.plot3D.w;
verts1 = stream3(x,y,z,u,v,w,sx,sy,sz);
verts2 = stream3(x,y,z,-u,-v,-w,sx,sy,sz);
w=myplt.tubewidth;
verts3=[];
aa=verts11,1';
nn=size(aa);
aa(:,1:nn(1,2))=aa(:,nn(1,2):-1:1);
verts3=[verts3 aa];
verts3=[verts3 verts21,1'];
verts3=verts3';
nn=size(verts3);
verts = mat2cell(verts3, nn(1,1), nn(1,2));
h1=streamtube(verts,w);
colorBline = str2num(get(Handle1.editHandle77, 'string'));
if(colorBline > 1);
colorBline=1;
end;
color= param.fmin+colorBline*(param.fmax-param.fmin);
newcolor=get(h1,'CData');
cmin=min(min(newcolor));
cmax=max(max(newcolor));
if(colorBline >= 0);
cnew=newcolor.*0+color;
end;
if(colorBline < 0);
cnew=param.fmin+(newcolor-cmin)/(cmax-cmin)*(param.fmax-param.fmin);
end;
if(colorBline <=-1);
cnew=ones([size(newcolor) 3]);
value = get(Handle1.popupmenuHandle7, 'Value');
colorselect = get(Handle1.popupmenuHandle7, 'String');
```

```
colorselect = colorselectvalue;
switch colorselect;
case 'red', cnew(:,:,1) = 1; cnew(:,:,2) = 0; cnew(:,:,3) = 0;
% [1 0 0]; red
case 'green', cnew(:,:,1) = 0; cnew(:,:,2) = 1; cnew(:,:,3) = 0;
% [0 1 0]; green
case 'blue', cnew(:,:,1) = 0; cnew(:,:,2) = 0; cnew(:,:,3) = 1;
% [0 0 1]; blue
case 'yellow', cnew(:,:,1) = 1; cnew(:,:,2) = 1; cnew(:,:,3) = 0;
% [1 1 0]; yellow
case 'cyan', cnew(:,:,1) = 0; cnew(:,:,2) = 1; cnew(:,:,3) = 1;
% [0 1 1]; cyan
case 'magenta', cnew(:,:,1) = 1; cnew(:,:,2) = 0; cnew(:,:,3) = 1;
% = [1 0 1]; magenta
case 'pink', cnew(:,:,1) = 1; cnew(:,:,2) = 0; cnew(:,:,3) = 0.5;
% = [1 0 .5]; pink
case 'orange', cnew(:,:,1) = 1; cnew(:,:,2) = 0.5; cnew(:,:,3) = 0;
% [1 .5 0]; orange
case 'lime green', cnew(:,:,1) = 0.5; cnew(:,:,2) = 1; cnew(:,:,3) = 0;
%[.5 1 0]; lime green
case 'aquamarine', cnew(:,:,1) = 0; cnew(:,:,2) = 1; cnew(:,:,3) = 0.5;
%[0 1 .5]; aquamarine
case 'sky blue', cnew(:,:,1) = 0; cnew(:,:,2) = 0.5; cnew(:,:,3) = 1;
%[0 .5 1]; sky blue
case 'violet', cnew(:,:,1) = 0.5; cnew(:,:,2) = 0; cnew(:,:,3) = 1;
%[.5 0 1]; violet
case 'black', cnew(:,:,1) = 0; cnew(:,:,2) = 0; cnew(:,:,3) = 0;
%[.5 0 1]; violet
case 'white', cnew(:,:,1) = 1; cnew(:,:,2) = 1; cnew(:,:,3) = 1;
%[.5 0 1]; violet
end;
end;
set(h1,'CData',cnew,'FaceColor','interp',...
'EdgeColor','none' ,...
'FaceLighting','phong',...
'BackFaceLighting','lit','visible','on');
h2=h1;
myplt.Bline.h1(myplt.Bline.numexist(1))= h1;
myplt.Bline.h2(myplt.Bline.numexist(1))= h2;
myplt.Bline.start(myplt.Bline.numexist(1),:)=[myplt.Bline.sx myplt.Bline.sy
myplt.Bline.sz];
return;
```

Appendix E

Sample Subroutine in MATLAB: 2-D Contours Plotting

```
function diag2Dplot global Field;


global param;
global myplt;
global Handle0 Handle1 Handle2 Handle3;
global figure_handle;
global V3D_HANDLES;
streamline_option=1;
movie2d=struct('cdata',[],'colormap',[]);;
for jj=1:param.nt
titlestring= get(Handle1.popupmenuHandle2, 'Value');
if param.nt==1
afile=param.filenames
else
afile=param.filenames(1,jj) ;
end
afilename=[param.pathname,char(afile)];
plotName=char(afile);
if(jj   = 1);
%case 'checkDATAbox'
value= get(Handle1.checkboxHandle1, 'Value');
if value ==1
param.dataType =1;
set(Handle1.checkboxHandle2, 'Value', [0]);
set(Handle1.checkboxHandle3, 'Value', [0]);
%read_Boxdata_textfile(afilename)
read_hy3d_box_data(0,jj)
end
%case 'checkDATAcov'
value= get(Handle1.checkboxHandle3, 'Value');
if value ==1
param.dataType =3;
set(Handle1.checkboxHandle1, 'Value', [0]);
set(Handle1.checkboxHandle2, 'Value', [0]);
read_hy3d_convert_data(afilename)
```

```
end
end;
reset_plot3D_p Handle2.figureHandle1=figure( ...
'Name','2', 'NumberTitle','off', ...
'Visible','off', 'BackingStore','off');
figure(Handle2.figureHandle1);
set(Handle2.figureHandle1,'Units','centimeters',...
'PaperPositionMode','Auto','Position',[2, 5 ,12, 12]);
reset_2d_param
if streamline_option==1;
x=myplt.plot3D.x3;
y=myplt.plot3D.y3;
z=myplt.plot3D.z3;
u=myplt.plot3D.u;
v=myplt.plot3D.v;
w=myplt.plot3D.w;
daspect([1 1 1])
my_streamslice=streamslice(x,y,z,u,v,w,[],[0],[],0.25);
set(my_streamslice,'Color','k');
hold all;
my_slice=slice(x,y,z,myplt.plot3D.p,[],[0],[]);
caxis([-5 5]);
set(my_slice, 'EdgeColor','None','FaceColor','Interp')
temp=findobj(gca,'type','surface');
my_x=get(temp(1,1),'xdata');
my_y=get(temp(1,1),'ydata');
my_z=get(temp(1,1),'zdata');
my_c=get(temp(1,1),'cdata');
my_x=interp2(my_x,3);
my_y=interp2(my_y,3);
my_z=interp2(my_z,3);
my_c=interp2(my_c,3);
set(temp(1,1),'xdata',my_x,'ydata',my_y,'zdata',my_z,...
'cdata',my_c);
this_axis=findobj(gca,'type','axes');
xlim(this_axis,[7.5 10.5]);
zlim(this_axis,[0 6]);
view(0,0);
set(gcf,'color',[1,1,1])
set(gcf,'outerposition',[1, 3 ,10.9,10.9]);
set(gca,'FontWeight','bold','FontSize',14,...
'FontName','Arial',...
'FontAngle','italic');
zlabel('Z','FontWeight','bold','FontSize',14,...
'FontName','Arial','FontAngle','italic');
```

```
xlabel('X','FontWeight','bold','FontSize',14,...
'FontName','Arial','FontAngle','italic');
colorbar('location', 'eastoutside');
colorbar('delete');
else
colormap jet; contourf(myplt.plot2D.xaix,myplt.plot2D.yaix,...
myplt.plot2D.p,20,'LineColor','none');
caxis([-1 1]);
colorbar;
shading flat;
title(titlestring);
end
end
filename='movie2d.avi';
fid=fopen(filename,'w');
if fid < 0
warndlg(['Selected file, "',filename, ...
' ", cannot be created or exists alreadey ...
and is used by another program.']);
else
movie2avi(movie2d,filename,'fps',4,...
'compression','none','quality',100);
try
fclose(fid);
catch;
end;
end;
% to add black regtangular option=0;
option1_tag=25;
if option==1,
switch option1_tag
case 15
width=1;
length=2;
angle=15;
rectangle_xi=[0 width width 0 0]
rectangle_zi=[0 0 length length 0]
rectangle_xf=cos(angle*pi/180).*rectangle_xi...
-sin(angle*pi/180).*rectangle_zi
rectangle_zf=sin(angle*pi/180).*rectangle_xi...
+rectangle_zi*cos(angle*pi/180)
line(rectangle_xf+9.5,rectangle_zi*0,...
rectangle_zf,'Linewidth',2,'Color','k');
case 25
width=1;
```

```
length=3;
angle=20;
rectangle_xi=[0 width width 0 0]
rectangle_zi=[0 0 length length 0]
rectangle_xf=cos(angle*pi/180).*rectangle_xi...
-sin(angle*pi/180).*rectangle_zi
rectangle_zf=sin(angle*pi/180).*rectangle_xi...
+rectangle_zi*cos(angle*pi/180)
line(rectangle_xf+9.18,rectangle_zi*0,...
rectangle_zf+1.1,'Linewidth',2,'Color','k');
case 35
width=1;
length=3;
angle=0;
rectangle_xi=[0 width width 0 0]
rectangle_zi=[0 0 length length 0]
rectangle_xf=cos(angle*pi/180).*rectangle_xi...
-sin(angle*pi/180).*rectangle_zi
rectangle_zf=sin(angle*pi/180).*rectangle_xi...
+rectangle_zi*cos(angle*pi/180)
line(rectangle_xf+9,rectangle_zi*0,...
rectangle_zf-1.5,'Linewidth',2,'Color','k');
case 65
width=1;
length=3;
angle=20;
rectangle_xi=[0 width width 0 0]
rectangle_zi=[0 0 length length 0]
rectangle_xf=cos(angle*pi/180).*rectangle_xi...
-sin(angle*pi/180).*rectangle_zi
rectangle_zf=sin(angle*pi/180).*rectangle_xi...
+rectangle_zi*cos(angle*pi/180)
line(rectangle_xf+9.2,rectangle_zi*0,...
rectangle_zf+1,'Linewidth',2,'Color','k');
end
end
return
```